Investigations on growth and structure of silver and silver halide nanostructures formed on amphiphilic dye aggregates

Dissertation
zur Erlangung des akademischen Grades

Doctor rerum naturalium
(Dr. rer. nat.)

im Fach: Physik
Spezialisierung: Experimentalphysik

eingereicht an der
Mathematisch-Naturwissenschaftlichen Fakultät
der Humboldt-Universität zu Berlin

von
Herrn Dipl.-Phys. Egon Steeg

Präsidentin der Humboldt-Universität zu Berlin:
Prof. Dr. Sabine Kunst

Dekan der Mathematisch-Naturwissenschaftlichen Fakultät:
Prof. Dr. Elmar Kulke

Gutachter:

1. PD Dr. Stefan Kirstein
2. Prof. Christoph T. Koch, PhD
3. Prof. Dr. Monika Schönhoff

Tag der mündlichen Prüfung: 31.08.2018

Abstract

Quasi one-dimensional inorganic nanostructures, with diameters in the order of several nanometers, received increasing interest over the past decades because of their promising application in the fields of electronics and photonics. Nanowires less than 7 nm in diameter can be grown within tubular aggregates of amphiphilic cyanine dyes by addition of silver nitrate to the aqueous solution as shown in previous work [1][2]. It was concluded that these wires consist entirely of pure silver. This thesis reports on the growth mechanism of these wires as revealed by conventional as well as cryogenic transmission electron microscopy. The growth, initiated by short illumination with UV light, has been observed over time scales ranging from minutes to days. In an early stage, within the tubular aggregates nanoparticles are formed which act as seeds for continuous growth of separate pieces of wires. The diameter of the wires is determined by the inner diameter of the tubes. In the final state, the pieces of wire totally fill the aggregate. The growth process indicates transport of at least silver ions through the tubular wall membrane. After homogeneously filling the template the wires grow onwards over the diameter of the nanotubes, destroying it in the process. A strategy is presented to stop the growth when the wires are completed by precipitation of excess silver ions via addition of chlorides.

The crystal structure of the wires was investigated by means of high resolution transmission electron microscopy and selected area electron diffraction. The clarification of the wires crystal structure led to the unambiguous finding that the wires consist of silver iodide. The silver iodide could be clearly identified in its β-phase by its typical wurtzite structure. Since only silver nitrate was added to the solutions, the source of the iodide ions could be attributed to impurities within the dye powder itself. The fragmented growth of the wires from separate seeds leads to nanowires consisting of single crystalline domains exceeding 100 nm in length. A preferential orientation of the crystal lattice planes with respect to the aggregate axis was observed which is explained by the molecular structure of the aggregates.

Based on these findings a model for the growth of silver iodide nanowires within the inner space of the tubular molecular aggregate is presented. The growth is assumed to start at silver seeds that are formed due to photooxidation of the already present iodide ions by the silver ions during the illumination of the sample. These silver seeds facilitate nucleation of silver iodide and subsequent growth into wires. These findings may demonstrate a possible route for growing other metal halide structures within the amphiphilic cyanine dye tubules.

Zusammenfassung

Quasi eindimensionale anorganische Nanostrukturen, mit Durchmessern in der Größenordnung von einigen Nanometern, fanden in den letzten Jahrzehnten aufgrund ihrer vielversprechenden Anwendung in den Bereichen Elektronik und Photonik zunehmendes Interesse. Durch Zugabe von Silbernitrat zu röhrenförmigen Farbstoffaggregaten in wässriger Lösung können Nanodrähte mit weniger als 7 nm im Durchmesser gezüchtet werden [1][2]. Es wurde festgestellt, dass diese Drähte vollständig aus reinem Silber bestehen. Diese Arbeit beschäftigt sich mit dem Wachstumsmechanismus dieser Drähte. Das Wachstum wurde initiiert durch Belichtung mit UV-Licht und über einen Zeitraum von Minuten bis hin zu Tagen untersucht. Im frühen Stadium bilden sich Silbernanopartikel innerhalb der Farbstoffröhren, welche als Keime für das weitere Wachstum von isolierten Drahtstücken dienen. Der Durchmesser dieser Drähte wird durch den Innendurchmesser der Röhren definiert. Im letzten Stadium wachsen diese Drahtstücke zusammen bis sie das gesamte Aggregat füllen. Dieser Wachstumsprozess impliziert einen Transport von Silber Ionen durch die Wand der Röhre. Das Wachstum der Drähte setzt sich weiter fort nachdem das Template gleichmäßig mit Drähten gefüllt ist und zerstört die Röhren in der Folge. Eine mögliche Strategie zum Stoppen des Wachstum wird vorgestellt.

Die Kristallstruktur der Drähte wurde sowohl mit hochauflösender Elektronenmikroskopie als auch Elektronenbeugung untersucht. Diese Untersuchungen erlaubten die eindeutige Zuordnung der Kristallstruktur zu Silberjodid. Das Silberjodid konnte aufgrund seiner charakteristischen Wurtzite Struktur in der β-Phase identifiziert werden. Da der Lösung nur Silbernitrat beigesetzt wurde, konnte die Quelle der Jod-Ionen als Verunreinigung im Farbstoffpulver ausgemacht werden. Das fragmentierte Wachstum der Drähte von verschiedenen Startpunkten aus führt zu Kristallen mit einkristallinen Domänen von mehr als 100 nm Länge. Eine bevorzugte Orientierung der Kristallstruktur relativ zur Aggregatachse wurde gefunden und durch die Molekülstruktur der Aggregate erklärt.

Basierend auf diesen Ergebnissen wurde ein Model zum Wachstum von Silberjodid Nanodrähten im Inneren eines röhrenförmigen Molekülaggregats entwickelt. Es wurde angenommen, dass das Wachstum an Silberkeimen beginnt, die durch Photooxidation der bereits vorhandenen Jod Ionen mit Silber Ionen während der Belichtung der Probe gebildet werden. Diese Silberkeime ermöglichen die Bildung von stabilen Silberjodid Kristalliten und das nachfolgende Wachstum zu Drähten. Die Ergebnisse zeigen einen möglichen Weg zur Synthese von Metall-Halogenid Strukturen innerhalb von Farbstoffröhren.

Contents

Chapter 1

Introduction

Nanotechnology is a highly promising research area attracting physicists, chemists, biologists, and engineers. Since "nano" describes just the scale in which concepts are established it allows for an interdisciplinary approach. The joint effort of many disciplines has led to a whole bunch of fascinating new basic principles and applications. Especially the field of optoelectronics has made tremendous progress in the last decades as can be seen for example in the development of new quantum dot light emitting diodes QD-LED [3]. Nanomaterials are defined by having one ore more of it's dimensions confined on a scale of less than a 100 nm and this work focuses on quasi one dimensional nanowires.

Metallic nanostructures in general have become an interesting research topic mostly because of their applications within the field of plasmonics [4]. Furthermore, they allow for the fabrication of transparent electrodes [5][6], and for the preparation of conducting nanocomposites [7]. Among other metals silver is favorable because of its plasmon resonance that may cover the whole visible spectrum [8][9]. Additionally, silver has the highest electrical conductivity of all pure metals.

Another practicable class of nanomaterials are semiconductors and among this whole class of materials silver iodide is of particular interest. Silver iodide offers the possibility for applications in solid-state battery and electrochemical sensing systems [10][11][12][13]. For example, a novel rechargeable, all-solid sate silver battery has been made by using superionic silver iodide nanoplates as solid electrolytes, which promises miniaturization into nanoscale silver batteries [13].

Silver iodide is a I-VII semiconductor with a direct band-gap of 2.82 eV at room temperature. The crystalline structure exhibits a rich phase diagram [14] with two phases in coexistence at ambient conditions [15]. At elevated temperatures ($\approx 420K$) it undergoes a phase transition to the so-

called superionic α-phase [16]. This phase transition is characterized by a recrystallization where part of the silver ions become highly mobile. Those silver ions are responsible for high ion conductivity as they provide the only appreciable contribution to the conductivity [17]. The ion conductivity for bulk silver iodide in the α-phase is in the order of 2 S/cm which is comparable to liquid electrolytes [18]. This effect is well documented but the underlying picture of the crystal structures within the superionic state has only emerged within the last ten years or so [18]. It is therefore still of major importance to study the crystal structure of this textbook example for fast ion conductivity, also on the nanoscale.

When reaching the nanoscale, preparation and architectural control of well-defined nanocrystals is requested for applications, since their physical and chemical properties are strongly influenced by their size and shape [19][20]. For silver iodide, for example, it was shown that the electric conductivity of polycrystalline silver iodide pellets increases when particle size decreases from the bulk to 140 nm [10][11]. A further decrease in size could possibly lead to even higher conductivity for smaller silver iodide. For other applications the shape is of utmost importance such as the usage as photochromic glass [21].

Especially high aspect ratio silver halide rods and wires show promising properties since silver halide fibers are flexible, water insoluble, non-toxic, and have good transmission in the mid-infrared region (3-5 mm) [22]. The so far developed techniques for the production of silver iodide nanomaterials involve synthesis via wet chemical methods. A controlled precipitation of silver iodide in presence of a stabilizing agent, which acts as a growth moderator through strong binding to certain surfaces, results in well-defined silver iodide nanostructures. Possible stabilizing agents are gelatin [23], organic polymers [24][25][26][27], and polyelectrolytes [28]. All these methods produce particles with diameters below 10 nm. Another approach is the synthesis of silver iodide by transient photochemical methods. The pulse radiolysis of methylene iodide was used to create iodide ions in aqueous solution which then generate silver iodide in varying sizes and shapes [29][30][31]. The shape-controlled preparation of silver iodide nanocrystals can also be achieved by the use of templates [32][33]. Alumina membrane templating has been successfully applied in production of polycrystalline silver iodide nanowire arrays [34]. However, it remains challenging to synthesize isolated highly anistropic single crystalline silver iodide nanowires with a well-defined diameter less than 10 nm in solution.

This work presents the interesting system of a tubular surfactant structure, that acts as a real template for the growth of nanowires. The amphiphilic cyanine dye molecule $3,30-bis(2-sulfopropyl)-5,50,6,60-$

tetrachloro−1, 10−*dioctylbenzimida*−*carbo*−*cyanine* (C8S3) forms double-walled nanotubes upon aggregation in aqueous solutions [35]. The growth of silver iodide and silver structures using the tubular J-aggregate formed by the C8S3 as a template was shown in principle in previous publications for the growth of particles [36] and wires [1].

This work focuses on the growth of high-aspect ratio nanowires within the inner space of the double-walled tube using the aggregate as a template. The growth of the wires is first investigated in terms of the underlying formation mechanism. The growth from photo-induced formation of seeds to homogeneous wires is slow enough (ranging from minutes to days) to be observed "in-situ" via transmission electron microscopy (TEM), which means by sample preparation at distinct time steps. Here the demanding questions to solve were.

- What is the reason of the photo-induced initiation of the growth?
- How is the growth mediated within the tubular template?
- How are wires formed out of seeds and nuclei and where are they formed predominantly?
- Are there ways to influence the growth of the wires?

The experimentally challenging elucidation of the actual nanowire's crystal structure was successfully obtained with TEM. To allow for application of the large-dose TEM techniques, such as electron diffraction, for the structural weak nanocrystals an unconventional approach was used. This included the use of a cryogenic holder, cooling the sample down during the measurements and results in the feasibility of the combined application of selected area electron diffraction (SAED) and high resolution transmission electron microscopy (HR-TEM). The structure analysis was used to answer the open questions about the real composition of the wires and related questions such as.

- Does the crystal structure analysis by SAED and HR-TEM leads to the same crystal and if so, what is it nature?
- Is the observed structure unique or do we see a coexistence of different phases (such as β-γ-silver iodide)?
- Can we identify grain boundaries as expected from the growth model?
- Is there an orientational correlation between the silver iodide crystallites and the tubular aggregate?

Based on these findings a model for the growth of silver iodide nanowires within a soft template is presented and discussed. This model could be further adopted to the use of different halides resulting in the synthesis of high aspect ratio silver halide nanowires. All these results combined can pave the way for a novel synthesis method of nanowires.

Chapter 2

Fundamentals

The following chapter introduces the fundamentals of this thesis. This work investigates the growth of inorganic nanowires within a soft template, which is a topic that spans chemistry, physics and materials science. The self-assembly of molecules as well as the synthesis of inorganics in solution is normally assigned to the field of chemistry, whereas the growth and characterization of crystals is considered a part of physics. The method of Transmission Electron Microscopy (TEM) on the other hand is closely related to material science. To give a detailed review of all the basic principles involved would go beyond the scope of this thesis. Nevertheless, all topics are touched upon to provide a basis for the understanding of this work. A brief introduction including literature recommendations for further information is given at the beginning of every section. The first part describes the process of micelle formation in aqueous solutions, followed by a detailed description of the aggregates actually used, and ends with the presentation of previous work this thesis is based upon. Then a brief introduction into the field of crystal structure analysis is given. This focuses on defining and characterizing the crystal structures that will be encountered in this work. The nucleation of crystals as well as the anisotropic growth in solution is briefly covered. Finally, a summary of the methods used during the course of this work with a focus on TEM is presented.

2.1 J-aggregates from cyanine dyes

The growth process of silver iodide nanowires presented in this work starts with a very well-defined organic system, namely a double-walled tubular J-aggregate as shown in Fig. 2.1. This tubular system, which self assembles in water, acts as a true template for the growth of the nanowires. This is because it dictates the size and shape of the nanowires without any change in its own size or shape. Since the wires precisely follow the morphology of the aggregate an introduction into the formation and resulting structure of this unique organic system is given in the following section. It is not possible to give an exhaustive list of the literature covering these topics, but the following are a few examples. A very good introduction into the field of micelle formation can be found in Jirgenson [38] while Tanford covers the hydrophobic effect [39]. A recent overview of the state of the art is given by Letchford [40]. An introduction to the fundamentals of the optical behavior of J-aggregate systems can be found in Davydov [41]. Möbius and Würthner have both published excellent reviews regarding recent developments in the field of J-aggregates [42][43].

2.1.1 Micelle formation

Molecular aggregates are non covalently bound supramolecular compounds. One group of molecules that show aggregation behavior are the so-called surface active agents or simply surfactants. These molecules are amphiphilic, meaning they have both hydrophilic and hydrophobic side groups in a single molecule, and form aggregates in aqueous solutions. The well solubilized

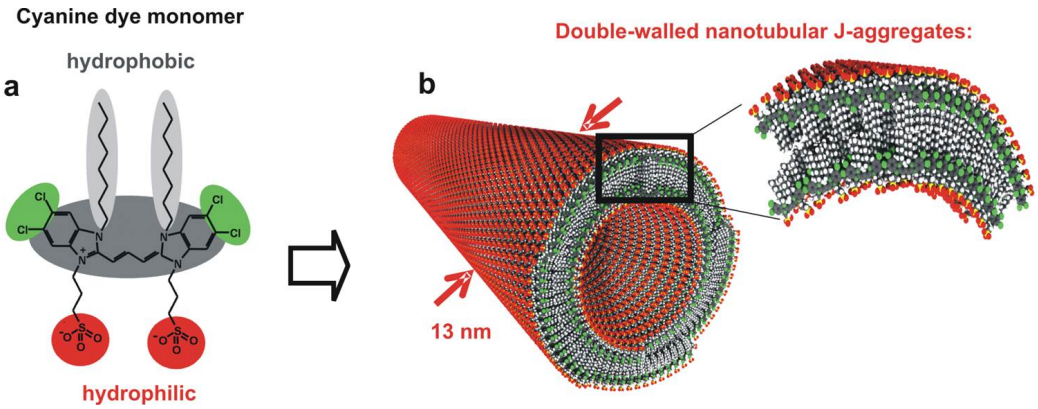

Figure 2.1: The C8S3 molecule with a 3D-model of the double-walled tubular J-aggregate[37].

part is hydrophilic and the poorly soluble part is hydrophobic, which leads to organization of the hydrophobic groups such that water is excluded and the hydrophilic groups remain in contact with the solvent. The result of this hydrophic effect is an increase of the entropy of water. The resulting structure is a so-called micelle. The formation of micelles depends on the concentration. For low concentrations the surfactants form a layer at the surface of the solvent. Once the concentration reaches a level where the surface is completely occupied they form micelles in solution as shown in Fig. 2.2. This threshold is called the critical micelle concentration (CMC). Those structures can have many different morphologies ranging from spherical micelles to double-layer structures. Israelachvili defined a surfactant packing parameter N_s as [44]:

$$N_s = \frac{V_c}{a_e l_c}$$

Where V_c is the volume of the hydrophobic chain, a_e the head group area per molecule at the aggregate interface, and l_c the length of the hydrophobic chain. With this parameter it is possible to predict the tendency of the structure of the resulting micelle for a given surfactant [45].

$$N_s < \frac{1}{3} \rightarrow \text{spherical micelles}$$

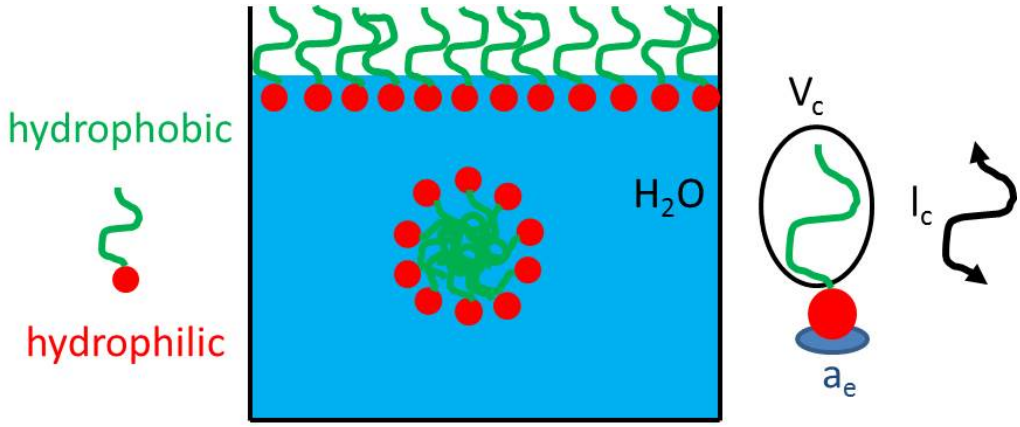

Figure 2.2: Sketch of surfactants in water. The surfactant molecules are made of an hydrophilic and hydrophobic part. First the surfactants will arrange on the surface of the water and later at a sufficient concentration form micelles in solution due to the hydrophobic effect. The shape of the resulting micelles can be predicted with the help of the surfactant packing parameter $N_s = \frac{V_c}{a_e l_c}$. Where V_c is the volume of the hydrophobic chain, a_e is the head group area per molecule at the aggregate interface, and l_c the length of the hydrophobic chain.

$$\frac{1}{3} < N_s < \frac{1}{2} \rightarrow \text{cylindrical micelles}$$

$$\frac{1}{2} < N_s < 1 \rightarrow \text{bilayers (or vesicles)}$$

$$N_s > 1 \rightarrow \text{inverted structures}$$

For common surfactants, the ratio V_c/l_c is a constant independent of tail length [46]. Hence, the area a_e is the main contribution in the packing parameter. This area is influenced directly by the hydrophilic headgroup. Thus, the headgroup controls the equilibrium aggregate structure in this model.

2.1.2 Tubular J-aggregates of C8S3

In this work we focus on a certain class of surfactants, namely amphiphilic cyanine dyes which exhibit interesting optical properties. Upon aggregation the broad-banded monomer absorption red shifts to a narrower but stronger band of absorption [47][48][49][50][51][52][53] as shown in Fig. 2.3. Such behavior was discovered independently by both Jelley [54] and Scheibe [55][56][57] for similar systems and are frequently referred to as "J-aggregates". If the aggregate absorption is instead blue shifted relative to the monomer then it is called an "H-aggregate" [58]. The amphiphilic 5,5',6,6'-benzimidacarbocyanines are a group of cyanine dyes with J-aggregate characteristics. Some of the aggregates formed by these dyes in aqueous solution have a tubular morphology [35]. One of these dyes is 3,3'-bis(2-sulfopropyl)-5,5',6,6'-tetrachloro-1,1'-dioctylbenzimida-carbo-cyanine, abbreviated as C8S3, used in this work. Fig. 2.1 shows the dye and its aggregate morphology. The monomer is composed of a backbone with the chromophore, two hydrophobic side chains eight carbon atoms long (C8), and the two polar sulfonate groups at the end of a three carbon atom long chain (S3), thus the name C8S3. It is a symmetric molecule with a delocalized π-electron system in the backbone. This chromophore has high polarizability, which leads to strong attractive van-der-Waals-forces, called dispersion forces, that favors stacking of the molecules. The combined influence of the hydrophobic effect and the dispersion forces leads to the formation of double-walled nanotubes in aqueous solution above the CMC of 10^{-5} mol/L [59][60]. The main features of these tubes are their uniform, reproducible morphology, namely a homogeneous outer diameter of 13 nm and inner diameter of 6.5 nm with lengths exceeding microns, and their optical properties. Fig. 2.3 shows the absorption spectra for the C8S3 monomer and the resulting J-aggregate. The J-aggregate absorbance is red-shifted with respect to the monomer and

contains two sharp bands, marked as (1) at 590 nm and (2) at 600 nm in the spectrum. Band (1) can be attributed to absorbance by the outer wall layer and band (2) to the inner wall [61][62][63]. The absorption at the two peaks is polarized along the main aggregate axis. Additionally the spectrum contains several other peaks and a shoulder at lower wavelength which are either due to residual monomers or excitonic transitions with perpendicular polarization to the aggregate axis. The postion and intensity of those bands are very sensitive to changes in the morphology of the J-aggregate and can be used as a "fingerprint" for the structural integrity.

2.1.3 C8S3 as template for nanowire growth

It was already demonstrated earlier that the tubular J-aggregates from the C8S3 can be used as a template for the growth of inorganic nanowires [1][64]. Growth of the inorganic nanowires was initiated by addition of silver nitrate to a solution of C8S3 aggregates, followed by brief illumination with blue light. The structures then grew in the inner space of the tubes during subsequent storage in darkness. Skipping the illumination step results in the growth of particles at the outer wall [36]. The line scans in Fig. 2.4 show that the nanowire matches the inner diameter of the double-walled tube of 6.5 ± 0.5 nm and the J-aggregate remains intact. The J-aggregate acts here as a real template without being destroyed. These nanowires were assumed to be silver nanowires. During the wire growth the absorption spectrum of the aggregates qualitatively changes and quantitatively decreases [65] as can be seen in Fig. 2.5. The change of spectral shape is due to the fact that

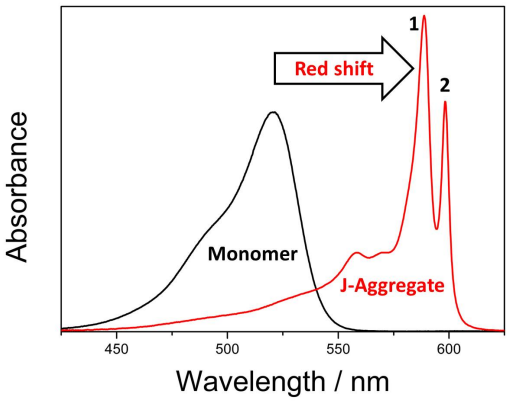

Figure 2.3: Absorption spectra of the monomer and the J-aggregate from C8S3. The J-aggregate has two sharp absorption bands at 590 nm (1) and 600 nm (2) red-shifted with respect to the monomer.

the different absorption peaks change their intensity at different rates. The fastest decrease is found for the strongest absorption band at 590 nm, which is attributed to absorption located at the outer dye layer of the aggregate, while a slower decrease is found for the absorption band at 600 nm that belongs to absorption located at the inner dye layer of the tubular aggregates. These changes can be explained by an oxidation of the tubular J-aggregates using silver ions as an external reducing agent. The controlled oxidation of a pure J-aggregate solution with cyclic voltammetry (CV) was observed via optical absorption spectroscopy and allowed to correlate the observed spectral changes with an oxidation of the nanotubes [66]. The change in conjugation length leads to a change in the optical spectra as can be monitored by absorption spectroscopy. It is important to notice that the oxidation of the dyes only modifies the conjugated π-electron system but does not decom-

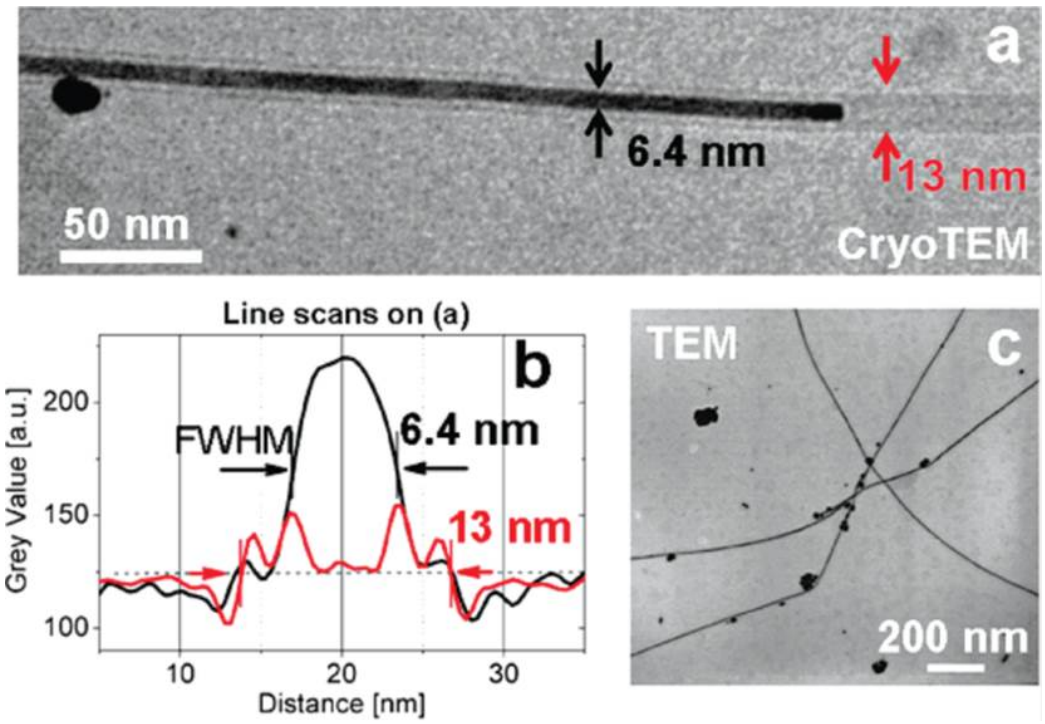

Figure 2.4: (a) Cryo-TEM image of a nanowire with a width of (6.4±0.5) nm partially filling a supramolecular dye nanotube, and a silver nanoparticle on the nanotube's outside 15 min after adding $AgNO_3$ to the solution and exposure to white light for 20 s. (b) Line scans across the template filled with silver (black) and unfilled template (red). (c) TEM image of nanowires immobilized on a solid substrate 72 h after adding $AgNO_3$ and exposure of the solution to white light for 90 min.[1]

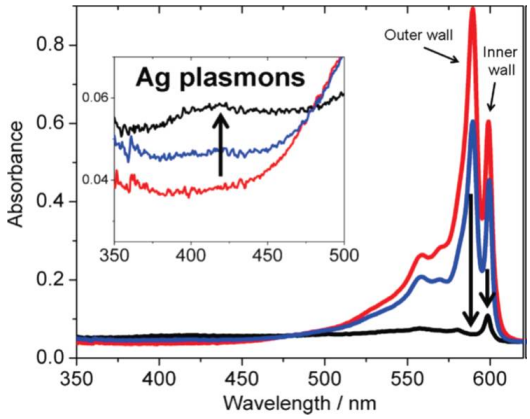

Figure 2.5: Blue: 4 h after adding AgNO3 (no light exposure). Black: 4 h after adding AgNO3 and exposure to white light for 5 min. Inlet: Zoom on silver plasmon peak $\approx$ 420 nm[1]

pose the molecules [67], which explains why the absorbance vanishes despite the morphology remaining unchanged. CV experiments with a J-aggregate solution, where silver nitrate has been added and illuminated, provided a response associated with the oxidation of silver, confirming the formation of neutral silver within the solution [64]. Additionally, cryo-TEM observations showed that only few aggregates are neither filled with a wire nor decorated with particles. The proposed mechanism for the formation of silver nanostructures in a J-aggregate solution was a localized redox chemistry at the walls of the tubes, where the silver ions get reduced by the dyes within the tubular aggregate.

2.2 Crystal structure and growth

This section illustrates the crystal structures that are of importance for the system. The crystal structures can be reduced to two types of lattices both of which are presented. The most common methods for the characterization of crystals are diffraction techniques. For an understanding of the recorded diffraction patterns the concept of Bragg reflexion and the reciprocal space is briefly discussed. The nucleation process is of utmost important for the growth process and an attempt has been made to elucidate the role of the template in this process. Further information may be found in any of a great number of introductory textbooks, for instance those of Kittel [68], Massa [69] and Giacovazzo [70]. Theories of nucleation and growth of crystals are manifold and very dynamic. The solution based crystallization in presence of biological system has opened the whole new field of biomineralization [71]. Recommended here is the review from Sear [72] since it deals especially with the nucleation in protein solutions and shows that molecules provide good nucleation sites for crystal growth.

2.2.1 The cubic closed packed and the hexagonal closed packed crystal structures

The extension of unit cell into a lattice is called a crystal. In three dimensions the possible lattice arrangements can be reduced to 14 "Bravais lattices" due to symmetry. For our case two structures are of major interest, both of which are related to the closed packing of spheres, the hexagonal closed packed (hcp) and the cubic closed packed (ccp) structure. Both result in the same packing density but with different symmetries [73]. Those are the two crystal structures observed in this work for silver, silver chloride and silver iodide. Silver crystallizes in a face centered cubic (fcc) structure and silver chloride in a cubic zinc blende structure. For silver iodide three different crystal phases exist: α-AgI crystallizes in a body centered cubic (bcc) structure, a hexagonal wurtzite structure for β-AgI forms, and a cubic zinc blende structure γ-AgI. From the three phases of AgI only the β- and γ-phase occur at standard conditions while the α-Phase is encountered under elevated temperatures at around 150°C. Since all experiments take place at room temperature we have to deal with two basic structures the ccp and the hcp. The ccp structure for silver results in a fcc unit cell, which is made up of a cube with an atom at each corner and face as can be seen in Fig. 2.6 **left**. There the vectors and angles that define the unit cell are marked. The angles between the pairs of vectors $\vec{b}$ and $\vec{c}$, $\vec{c}$ and $\vec{a}$, and $\vec{c}$ and $\vec{b}$ are defined as α, β, and γ respectively. Silver chloride, as γ-AgI, has two types of atoms in the unit cell, a crystal

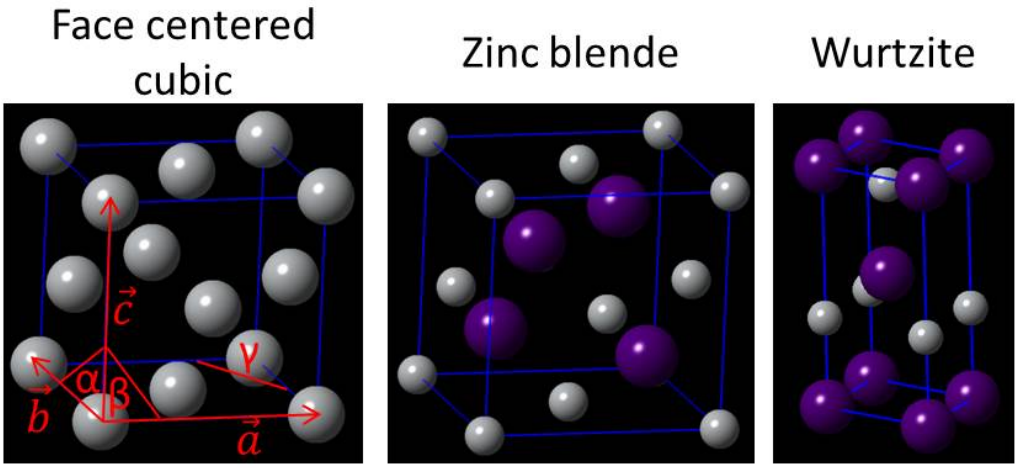

Figure 2.6: Overview of the main crystal structures encountered in this work. The face centered cubic (fcc), the zinc blende, which is fcc but with two kinds of atoms in the unit cell, and the wurtzite, a hexagonal closed packed structure with two different atoms in the unit cell. For fcc the base vectors and their respective angles are shown.

structure called zinc blende. Fig. 2.6 **middle** shows the unit cell for γ-AgI with the gray atoms as silver and the purple ones as iodine. The unit cell for wurtzite β-AgI is shown in Fig. 2.6 **right** with the same color code as for γ-AgI. Again the structure is distinguished from hcp since the unit cell consists of two atoms. The lattice parameters for the four encountered crystals are summarized in the following table (from the Crystallography Open Database: [74], see methods):

	Silver	**Silver Chloride**	**γ-Silver Iodide**	**β-Silver Iodide**
a [Å]	4.09	5.47	6.47	4.59
b [Å]	4.09	5.47	6.47	4.59
c [Å]	4.09	5.47	6.47	7.52
α [°]	90	90	90	90
β [°]	90	90	90	90
γ [°]	90	90	90	120

2.2.2 Indexing of lattice planes

A standard notation for crystal lattice planes uses Miller indices. The base for every crystal system is given by the unit cell, which is made up of the three lattice vectors $\vec{a}$, $\vec{b}$, and $\vec{c}$ and their respective angles α, β and γ. Every

lattice plane intercepts the crystal system at specific coordinates. The Miller indices are proportional to the inverses of the intercepts of the plane, in the basis of the lattice vectors. They are relatively prime integers and a triplet of them defines one specific lattice plane (hkl), that intercepts the unit cell at the points $(\frac{\vec{a}}{h}, \frac{\vec{b}}{k}, \frac{\vec{c}}{l})$. If one of the indices is zero, it means that plane does not intersect that axis. Fig. 2.7 shows three lattice planes with their Miller indices for a cubic system. The (100) plane intercepts the unit cell at one point along the $\vec{a}$ axis and does not intercept in the other directions. The (100) plane is then the face of the cubic unit cell perpendicular to $\vec{a}$. By extension, (010) would be the face of the cube perpendicular to $\vec{b}$. Since these numbers are the inverses of the intercepts it means that (200) would be the plane at half of the length of the lattice vector $\vec{a}$ resulting in this plane being parallel to the (100) plane and located halfway between the (100) and the origin. For the (110) plane, the intercepts are then at lattice lengths a and b in the direction of $\vec{a}$ and $\vec{b}$ as shown in Fig. 2.7. These planes define the edges of the unit cell. The (111) plane intercepts the unit cell at the corners. For planes intercepting the unit cell at the opposite direction of one of the lattice vectors a dash is written over the Miller index instead of a minus, e.g. $(\bar{1}00)$ instead of (-100). If instead of a single unique plane an equivalent set of lattice planes is being considered, the miller indices are written in curly brackets. This depends strongly on the symmetry of the given lattice. For the highly symmetric cubic system the notation {100} addresses the three planes with identical symmetry (100), (010), and (001). Due to the symmetry

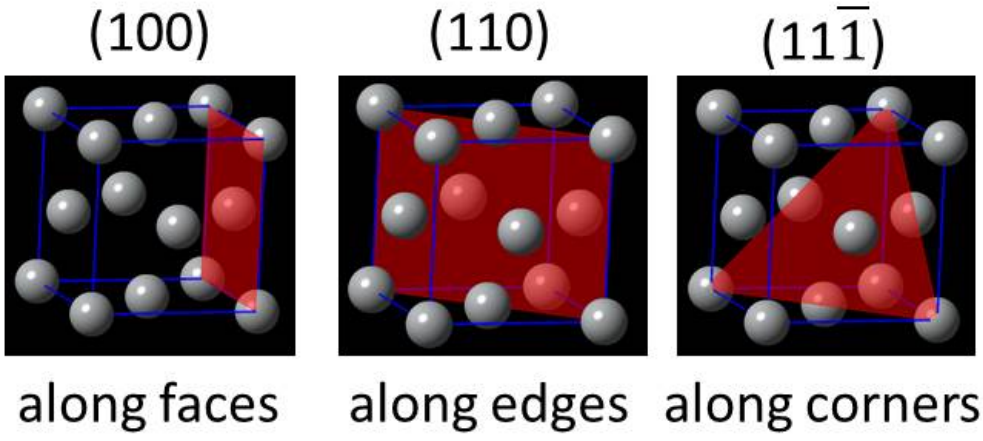

Figure 2.7: Three frequently considered planes for the face centered cubic lattice and their respective Miller indexes.

these planes are identical and the notation exploits that.

For a hexagonal system a fourth index, i, is introduced, resulting in the Miller-Bravais notation (hkil), whith $i = -(h + k)$. The hexagonal base can tessellate a surface, but the description of the translation is complicated if restricted to an orthonormal basis. So the unit cell is often defined by a hexagonal base of three planar vectors $\vec{a_1}$, $\vec{a_2}$, and $\vec{a_3}$ plus the "height" of the unit cell as $\vec{z}$. In Fig. 2.8 the base and the three vectors are shown, where $\vec{a_3}$ = -($\vec{a_1}$ + $\vec{a_2}$). The two black vectors are the "normal base vectors" that together with $\vec{z}$ define the unit cell as mentioned above for the hcp crystal. Planes that define the three faces of the hexagon marked in green are in the Miller notation written as (100), (010), and ($\bar{1}$10). Those triplets are shown in black at the respective planes and from this notation no apparent permutation symmetry is present. By introducing the fourth vector $\vec{a_3}$ those planes become (10$\bar{1}$0), (01$\bar{1}$0), and ($\bar{1}$100) as marked in red. For the permutation symmetry the last integer is ignored and all three planes can be written as {10$\bar{1}$0}. From there all three planes are obtained by cyclic permutation without changing the last integer, so {10$\bar{1}$0} means the three equivalent planes (10$\bar{1}$0), ($\bar{1}$100), and (01$\bar{1}$0). This notation is often used for hexagonal crystal systems. Whenever a lattice plane is defined in the Miller-Bravais notation it is from a hexagonal system. Note that those crystals can of course be

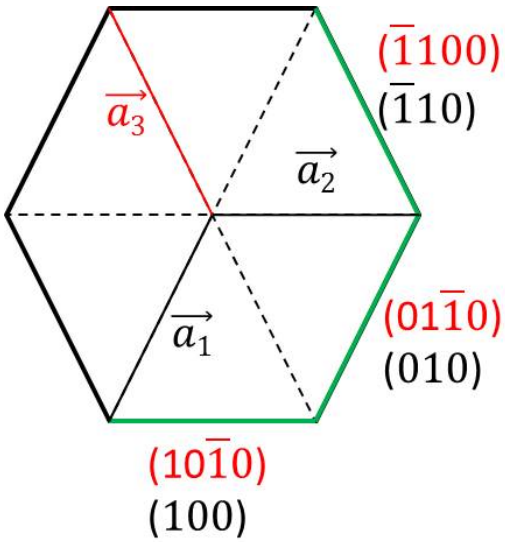

Figure 2.8: Base of the hexagonal closed packed structure. To describe the faces of the base hexagon, marked in green, the two base vectors and the Miller notation can be used as shown in black. The Miller-Bravais indices introduce a fourth vector to describe equivalent planes in the hexagonal base, here marked in red.

defined by the Miller notation only, but then it is not possible to indicate several equivalent planes with just one set of indexes. The conversion is defined as $(h, k, l) \rightarrow (h, k, -(h + k), l)$.

2.2.3 Diffraction on crystals

The most common method to characterize lattices is diffraction. X-rays and electrons have a wavelength on the order of typical lattice plane distances. The diffraction of waves on a periodic system is described by the Bragg equation:

$$n\lambda = 2dsin\theta$$

where n is a positive integer, λ is the wavelength of incident beam, d is the interplanar distance between lattice planes, and θ is the scattering angle. It implies that the radiation is reflected from the lattice planes. Only when the Bragg condition is fulfilled constructive interference occurs and thus a Bragg reflection is visible. For a crystal the distance d is related to the distance between certain lattice planes described by the Miller indices and d becomes d_{hkl} to point out a specific interplanar distance in the crystal.

Diffraction on crystals is usually considered in reciprocal space. For every lattice in real space a uniquely defined reciprocal lattice exists. The reciprocal lattice does not correspond to array of atoms, as each point is associated with a particular set of planes in the crystal. Sets of parallel atomic planes (hkl) are represented by a single point located a distance $1/d_{hkl}$ from the lattice origin. A reciprocal lattice vector $\vec{G_{hkl}}$ is a vector from the origin to a specific point (hkl) in the reciprocal lattice. A wave can be described by the wave vector $\vec{k}$, which points in the normal direction to the wave fronts and has the length $|k| = \frac{2\pi}{\lambda}$.

The notation of the Bragg equation in terms of reciprocal lattice and wave vectors is called Laue condition:

$$\vec{k} - \vec{k_0} = \vec{G_{hkl}}$$

where $\vec{k_0}$ is the wave vector of the incident beam, $\vec{k}$ is the wave vector of the diffracted beam, and $\vec{G_{hkl}}$ is the change of the vector and needs to be a reciprocal lattice vector. $\vec{G_{hkl}}$ defines at which lattice spacings in the crystal diffraction takes place. The Ewald sphere construction gives a simple geometric interpretation for the Laue condition. To find the lattice planes for which the Bragg condition is fulfilled for elastic scattering, one can draw a sphere with radius $2\pi/\lambda$, where λ is the wavelength for the incident light. This is sketched in Fig. 2.9 for two dimensions where the sphere is a circle and the reciprocal lattice shown is a two-dimensional section of the actual

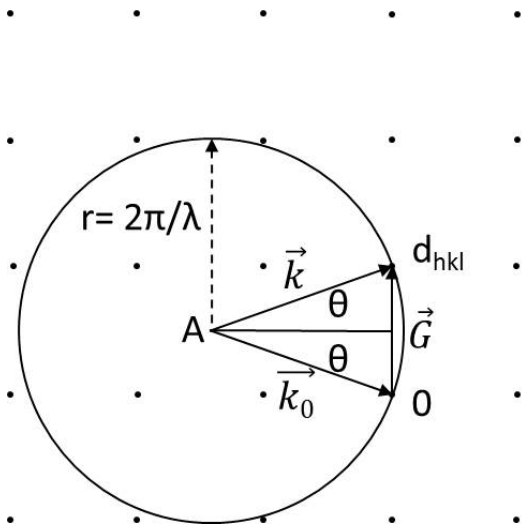

Figure 2.9: The Ewald construction for a two-dimensional reciprocal lattice.

lattice. The sphere passes trough the origin of the reciprocal lattice indicated by the point 0, that is not the origin of the sphere, with the radius defined by its wavelength. For every point in the reciprocal lattice intersected by the circle the Bragg equation is satisfied and the corresponding planes in real space will diffract strongly. This is shown for elastic scattering where $|\vec{k}| = |\vec{k_0}|$ and $\vec{G}$ represents the change in direction only and θ is the Bragg angle.

For perfect crystals with infinite dimension the points are infinitesimally small and for producing a sufficient number of diffraction spots to characterize the specimen the sample needs to be rotated or "white" radiation is used. For crystals with finite dimension the diffraction spots are broadened (with respect to infinitesimally small spots). The Scherrer equation relates the size of a crystallite to the broadening of a peak in a diffraction pattern [75].

$$\Delta(2\theta) = \frac{K\lambda}{Lcos\theta}$$

Where $\Delta(2\theta)$ is the line broadening at half the maximum intensity in radians, K is a dimensionless shape factor with a value close to unity, λ the wavelength, L is the mean size of the crystalline domain, and θ the Bragg angle. Since $\Delta(2\theta) \approx \frac{1}{L}$, the smaller a given crystallite the broader are the resulting peaks.

2.2.4 Classical nucleation theory

The growth of crystals is in general described by a two step process. In the first step nuclei form, and in the second step the nuclei grow into crystal. The formation of nuclei or nucleation is the first step in the formation of a new thermodynamic phase or a new structure in which stable clusters of atoms will form. The driving force behind the formation is the reduction of the free energy, which needs to be lower than the free energy of the initial phase or structure [76]. For example a phase transition from liquid to solid in a supersaturated solution can decrease the free energy. Those solids are called nuclei and are a result of density fluctuations. It is well accepted within framework of the classical nucleation theory (CNT) that the nuclei are unstable until they reach a critical size. Before that size a nucleus is more likely to dissolve back into the solvent than to grow. The rate at which

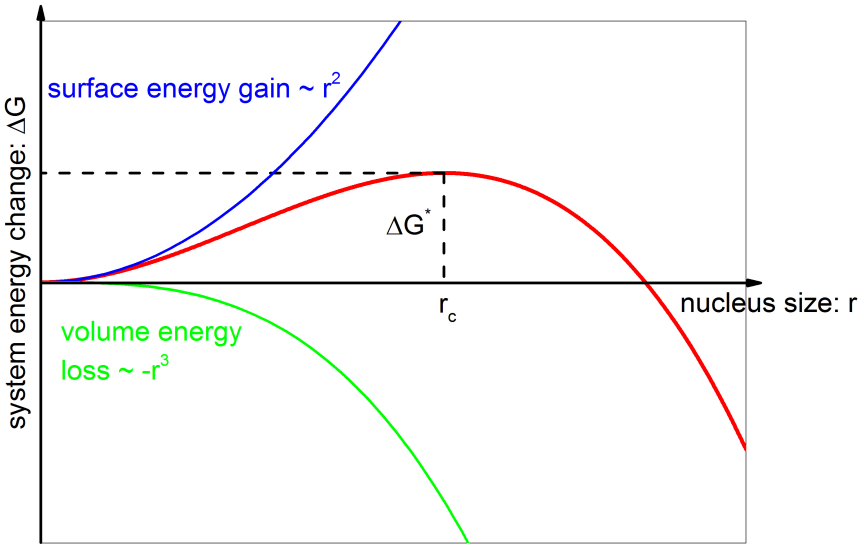

Figure 2.10: Sketch of the two competitive processes in homogeneous nucleation as described by classical nucleation theory: The gain in surface energy vs. the loss in volume energy. Only if the nuclei reach a critical radius r_c they can overcome the energy barrier ΔG^*, becoming stable because growth then lowers total energy.

critical nuclei form is given within the CNT [72]:

$$R_{CNT} = \rho j Z exp\left(-\frac{\Delta G^*}{k_B T}\right)$$

This is a rate per unit volume and consists of a prefactor and an exponential factor. The exponent is of primary interest since it contains an energy barrier, ΔG^* the free energy cost of creating a critical nucleus divided by the thermal energy $k_B T$. The prefactor is composed of three terms: number density of molecules ρ, rate j at which molecules attach to the nucleus, and the Zeldovich factor Z, the probability that a nucleus at the top of the barrier will go on to form the new phase, not dissolve. The prefactor is often taken to be a constant since the exponential factor typically varies much more rapidly. Under the assumptions that nucleation happens freely in solution and the nuclei are spherical, which is called homogeneous nucleation, we can estimate the exponential factor according to [77]:

$$\Delta G = \frac{4}{3}\pi r^3 \Delta g + 4\pi r^2 \sigma$$

The first term is a volume term (volume of a sphere) times Δg, the change in free energy per unit volume between the two thermodynamic phases (e.g. solid/liquid), which is always negative for nucleation because of the binding energy. The second term is a surface term (surface of a sphere) times σ, the surface tension, which is always positive. This is qualitatively plotted in Fig. 2.10. From this model the energy barrier ΔG^* needed to calculate R_{CNT} is found by setting $\frac{d\Delta G}{dr} = 0$:

$$r_c = -\frac{2\sigma}{\Delta g} \Leftrightarrow$$

$$\Delta G(r_c) = \frac{16\pi\sigma^3}{3(\Delta g)^2} = \Delta G^*$$

From this energy barrier, the rate R_{CNT} at which critical nuclei will form can be calculated. This calculated rate appears to be very low and actual nucleation rarely occurs homogeneously.

However nucleation predominantly occurs at surfaces in what is called heterogeneous nucleation [78] in contrary to the above described homogeneous nucleation which happens in the pure bulk. The growth of nuclei at impurities or surfaces increases the rates of nucleation many orders of magnitude making homogeneous nucleation unlikely. At surfaces, the effective

surface energy is lowered, thus diminishes the free energy barrier and facilitating nucleation. The simplest approach is to assume a plane surface at which "wetting" occurs and the CNT can be expanded to [72].

$$\Delta G_{heterogeneous} = \Delta G_{homogeneous} * f(\theta)$$

Where $f(\theta)$ is a function of the contact angle θ. The angle θ depends on three interfacial tensions, namely γ, between the nucleus and the bulk phase, γ_{bs}, between the bulk phase and the surface, and γ_{ns}, between the nucleus and the surface. The contact angle θ is related to the three interfacial tensions by Young's equation:

$$\gamma_{ns} + \gamma cos(\theta) = \gamma_{bs}$$

With this equation it is possible to derive an expression for $f(\theta)$ [79].

$$f(\theta) = \frac{2 - 3cos\theta + cos^3\theta}{4}$$

For $\theta = 180°$ the function becomes 1 and the nucleus detaches itself from the surface, where heterogeneous and homogeneous nucleation are the same. For $\theta = 0°$ the function becomes zero and a layer of the new phase forms. This is because there is a thermodynamic driving force for forming a thick wetting layer.

2.2.5 Growth of Crystals

After the formation of nuclei larger than the critical size, the growth of crystals starts. For the growth in solution this process is due to the attachment of atoms on the surfaces of the nuclei. This process is defined by diffusion in solution or at surfaces. Many theories exist regarding the actual kinetics of crystal growth and a thorough discussion of the topic would exceed the scope of this work. However, one important consideration should be made regarding the equilibrium shape of the resulting crystals. Volmer suggested in the 1930s [80][81][82] that atoms arriving on a crystal surface do not enter the lattice, but rather lose only one degree of freedom and can freely diffuse over the surface. Those units will integrate into the lattice on energetically favorable positions (i.e. kinks). Due to this high degree of freedom, the crystal growth proceeds most rapidly on faces that provide the highest decrease in surface energy, namely the closed packed ones. The shape of the resulting crystal is that with the minimum surface energy.

The equilibrium form can be estimated with the help of the Wulff construction [83]. This is based upon the Gibbs condition for the minimization

of surface energy. It states that, for a given volume, the ith plane with surface energy γ_i will have an area A_i that minimizes the overall surface free energy $\Sigma\gamma_i A_i$. For the Wulff construction an arbitrary point O in the crystal is taken as a reference as shown in Fig. 2.11. A characteristic vector $\vec{OP_i}$ for each plane is then defined as being perpendicular to the i-th plane with a length corresponding to the surface energy γ_i of this plane. To construct the equilibrium form, one needs to draw vectors normal to the possible crystallographic planes. The lengths of the vectors are proportional to the corresponding γ_i-values defining endpoints P_i. At every endpoint P_i a tangent which is perpendicular to the vector is drawn. The inner envelope of these tangents gives us the equilibrium shape.

Important for applications is the growth of crystals in a desired shape, which may differ from the equilibrium shape. For the growth of highly anisotropic crystals several methods have been established [84]. Of particular interest here is the growth of high-aspect ratio crystals such as wires or rods in the nanometer regime. Diffusion limited aggregation (DLA) is a widely observed phenomena leading to anisotropic but undirected growth resulting in "finger-like" structures called Brownian trees [85]. As a result of Brownian motion particles have a higher probability of adsorbing at the tips of already existing structures. This leads to the growth of dendritic structures which are fractals [86].

The difference in surface energies is the reason why some crystals have an elongated morphology as their equilibrium shape. This intrinsic property of the crystal is often not large enough to cause highly anisotropic growth of

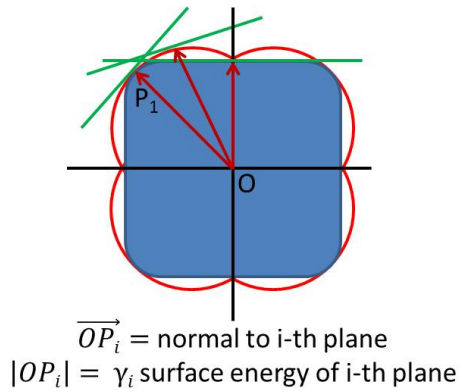

Figure 2.11: Wulff construction by drawing vectors OP perpendicular to the possible crystallographic planes with lengths corresponding to the surface energy of these planes. At the end of every vector a tangent is drawn. The inner envelope of these tangents gives us the equilibrium shape.

long nanowires. The effective surface energy of a nanocrystal can be modified by adding surfactants to the reaction solution [84]. These surfactants act as "surface capping agents" by selectively adsorbing and binding to certain surfaces. The growth can then continue only on the un-capped surfaces, since the growth units can not attach to the capped surfaces. The result is a far more anisotropic structure than their equilibrium shape. Silver nanowires have been grown with the use of poly(vinyl pyrrolidone) PVP as capping agent [87][88]. The PVP selectively binds to the {100} facets of Ag particles and allow the growth on the {111} facets.

Another method for anisotropic growth is the use of templates. Templates are certain structures that define the morphology of the resulting crystals. A template is an integral part of the grown structures as it stays intact during the whole process. It provides a confined volume in which the growth units of the resulting crystal can arrange and follow the shape of the template. Possible templates for the growth of high-aspect ratio crystals are porous substrates. The pores act as structure defining entity for the growth of nanowires. Those wires will reproduce the shape of the pores and are arranged in the same way as the pores on the substrate [89]. For the growth of single nanowires hard templates such as silicon nanotubes [90] or mesoporous silica [91] as well as soft templates like DNA [92] and most recently also insulin fibrils [93] are used.

2.3 Transmission Electron Microscopy

Almost all experimental data presented in this work were collected by transmission electron microscopy (TEM). This is why the basic imaging methods used are briefly presented and explained here. For the analysis and interpretation of the data a detailed understanding of how the contrast is generated in TEM images for the given images is crucial. Electrons are charged and therefore interact strongly with matter. The basic interactions are summarized in Fig. 2.12. Some of these interactions can be used for imaging, such as the scattering of electrons, and some for a detailed analysis of the specimen such as the emitted X-rays. The following methods were used:

- Conventional transmission electron microscopy (TEM)
- Cryogenic transmission electron microscopy (cryo-TEM)
- High-resolution transmission electron microscopy (HRTEM)
- Scanning transmission electron microscopy (STEM)
- Energy dispersive X-ray spectroscopy (EDXS)
- Selected area electron diffraction (SAED)

The presentation here closely follows the book written by Williams and Carter [94]. However, many other excellent introductory textbooks exist

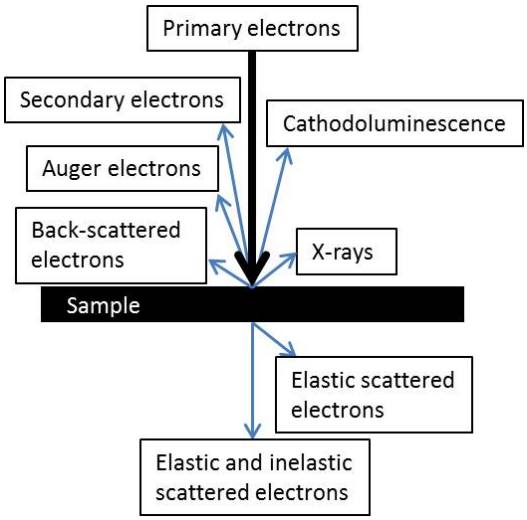

Figure 2.12: Overview of the interactions between electrons and matter

and the interested reader is directed to [95][96][97][98]. An example image is shown for each technique to support the explanation. The images are selected from the experimental work of the thesis and mostly show the nanowires central to this work.

2.3.1 Imaging with electrons

One reason to invent electron microscopy was to overcome the resolution limit of optical microscopy. This limit can be described by the Rayleigh-criterion.

$$d_{min} = 0.61\frac{\lambda}{NA}$$

with

$$NA = nsin\varphi$$

Where d_{min} is the minimum distance of two objects that can be separated by visual inspection, λ is the wavelength, NA the numerical aperture, φ is the maximal half-angle of the cone of light that can enter or exit the lens, and n the refraction index. The resolution is therefore mainly given by the wavelength of the used light. The resolution can be increased by using light of shorter wavelength in the visible range or by changing the refraction index n by using an oil-immersion. For classical-optical microscopy the limit achievable for d_{min} is about 240 nm. The main idea behind TEM is to replace the optical photons with accelerated electrons. The particle-wave-dualism allows to assign a wavelength to the accelerated electron with the de-Broglie-equation.

$$\lambda_{dB} = \frac{h}{\sqrt{2m_0eU_B^*}}$$

with

$$U_B^* \cong U_B\left(1 + \frac{eU_B}{2m_0c^2}\right)$$

Where h is the Planck constant, m_0 the electron mass, e the elementary charge, U_B the acceleration voltage, and U_B^* the voltage with relativistic correction. An electron accelerated with 100 keV has a wavelength of 0.0037 nm, which theoretically allows for resolution in the sub-nanometer-range. For the use of electrons in microscopy the lenses have to be built from electric and magnetic fields. These lenses also suffer from image defects or aberrations. These aberrations limit the resolution, which is rather defined by technical than physical properties. Nevertheless, almost every modern TEM achieves a resolution of at least 0.25 nm.

2.3.2 Contrast in TEM

Another important parameter in imaging is the contrast. The contrast c can be defined as difference in intensity ΔI between two adjacent areas.

$$c = \frac{I_1 - I_2}{I_2} = \frac{\Delta I}{I_2}$$

To observe this change in intensity caused by the specimen with bare eyes on the screen or photograph, the contrast should be higher than 5%. Using a camera for image recording can enhance low contrasts electronically. This difference can be caused by several mechanism.

The amplitude contrast is mainly achieved by a change in the amplitude of the electron wave function. This amplitude contrast originates from two mechanisms: mass-thickness contrast, and diffraction contrast. Mass thickness contrast is due to incoherent Rutherford scattering of electrons. The Rutherford cross section is a function of the atomic number Z [94].

$$\frac{d\sigma_{Rutherford}(\theta)}{d\Omega} = \frac{e^4 Z^2}{16(E_0)^2 sin^4 \frac{\theta}{2}}$$

Where $\frac{d\sigma(\theta)}{d\Omega}$ is the differential scattering cross section, e the elementary charge, Z the atomic number, E_0 is the electron energy, and θ is the scattering angle. Higher atomic number material leads to a larger Rutherford cross section and therefore more scattering to higher angles then lower atomic number materials. Since Rutherford scattering occurs at the nucleus of the material one can express this equation to define $Q_{nucleus}$, the number of scattering events per unit distance that the electron travels trough.

$$Q_{nucleus} t = (N_0 \frac{\rho}{A} t) \sigma_{Rutherford}$$

Where t is the thickness of the specimen, N_0 is Avogadro's number, ρ is the density of the sample, A is the atomic weight of the atoms in the specimen, and σ the scattering cross section. The product ρt is called the "mass-thickness" of the specimen. The thicker a specimen is the more scattering will occur.

Bragg diffraction can also be used to create contrast in TEM. This diffraction contrast is simply a special form of amplitude contrast because the scattering occurs at special angles. The contrast depends on the orientation of the crystalline sample.

Another important mechanism is the phase contrast. For thin specimen, less than 50 nm, parts of the electron wave front are phase-shifted with respect to the unaffected wave after passing the sample. This can be described

as the wave w_1, penetrating the object, is being composed of two waves, the zero wave w_0 and the diffracted wave w_2 [99]. The phase of the wave penetrating the object is shifted by φ_1. For a wave propagating in z direction with amplitude a_0 and angular velocity ω.

$$w_0 = a_0 sin(kz - \omega t)$$

$$w_1 = a_0 sin(kz - \omega t + \varphi_1)$$

For "weak phase objects" this phase shift φ_1 is small compared to $\frac{\pi}{2}, \varphi_1 << \frac{\pi}{2}$ and we can use $cos\varphi_1 \approx 1, sin\varphi_1 \approx \varphi_1$.

$$w_1 = a_0 sin(kz - \omega t) + a_0 \varphi_1 cos(kz - \omega t)$$

The second term is called diffracted wave.

$$w_2 = a_0 \varphi_1 cos(kz - \omega t)$$

$$w_1 = w_0 + w_2$$

The amplitude of the diffracted wave $a_0\varphi_1$ is very low for "weak phase objects". In an ideal microscope this diffracted wave is almost not visible. The penetrating wave carries the signal in form of phase shifts which are invisible in a focused image. In the image only the amplitude of the penetrating wave w_1 is recorded. By introducing a difference in the optical path for the two waves w_0 and w_2 they can be separated.

2.3.3 Phase-contrast imaging in TEM

A perfect lens would focus both the unaffected wave and the diffracted wave to the same focal point. Aberrations in the imaging system (e.g. defocus, astigmatism, spherical aberration, etc.) impose different phase shifts on waves that travel at different angles through the objective lens and have thus a strong effect on the contrast of images. While in a conventional TEM without an aberration corrector, the spherical aberration is fixed, defocus and astigmatism can be adjusted. For weak phase objects, the defocus can thus be tuned to enhance the image contrast. Spherical Aberration describes the deviation of the shape of the phase plate that is imposed by a lens on the transmitted wave from that of a sphere. The electrons passing through the lens at different scattering angles experience different phase shifts. In the case of defocus this phase shift is proportional to the square of the scattering angle, and spherical aberration introduces a phase shift that is proportional to the 4th power of the scattering angle. This effect of positive spherical

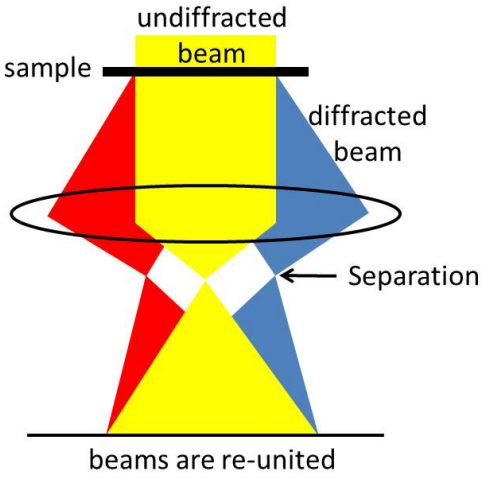

Figure 2.13: Schematic to illustrate the influence of the lens in phase-contrast imaging. The lens focuses the unaffected as well as the diffracted beams to different points in the focal plane. The separated waves are re-united on the image plane, causing an interference of the beams.

aberration causes electrons passing through the lens at higher angles to effectively see a lens with a shorter focal length. Aberrations of the objective lens impose different phase shifts on waves that travel at different angles through the optical system (beams). The result is an interference of these beams, causing an amplitude modulation in the image.

The phase contrast can be even stronger if the objective lens is defocused. The total phase shift in TEM can be expressed by the phase-distortion function χ [94].

$$\chi = \pi \Delta f \lambda u^2 + \frac{1}{2} \pi C_s \lambda^3 u^4$$

Where Δf is the defocus, λ the De Broglie wavelength of the electrons, u the spatial frequency, and C_s the spherical aberration. This equation has the form of a phase shift expressed as $2\pi/\lambda$ times the path difference. From the phase shift results a change in the contrast leading to the contrast transfer function T(u).

$$T(u) = 2sin\chi(u)$$

In Fig. 2.14 shows a representative plot of T(u) versus u (C_s = 1.2 mm, E_0 = 200 keV, Δf = -67 nm) done with CTF Explorer [100]. This is an oscillatory function of the spatial frequency. When the function is negative, that represents positive phase contrast, leading to a bright background, with

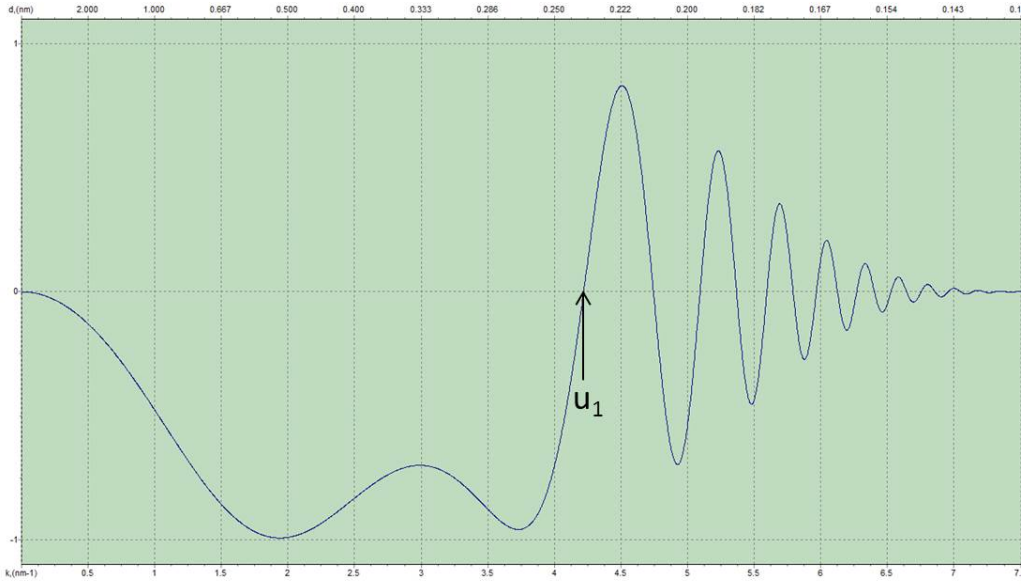

Figure 2.14: Plot of the contrast transfer function for C_s = 1.2 mm, E_0 = 200 keV, Δf = -67 nm done with CTF Explorer [100]. For frequencies higher than u_1 the contrast is inverted.

dark atomic features. For frequencies at which the function becomes zero, no contrast is generated and those frequencies do not contribute to the output signal. The first frequency u_1 for which T(u) becomes zero is an important parameter since this frequency will give no contrast and any higher frequency will show a weaker and inverted contrast. So u_1 defines a limit at which our image may be quite directly interpreted. For the plot in Fig. 2.14 u_1 is around 4 nm^{-1} or 0.25 nm in real space, meaning that periodicities or, in the case of a crystal, lattice spacings as low as 0.25 nm can be imaged without significant changes in the contrast. The best transfer function is the one with the highest u_1 or the fewest zeros.

2.3.4 Conventional transmission electron microscopy

Conventional TEM is probably the most practiced technique for this type of microscope and is here referred to simply as TEM. It is in principle a bright field method with electrons where the contrast is mainly achieved by a change in the amplitude of the electron wave function. For thin specimen this amplitude contrast originates from scattering of electrons by the sample. Placing an aperture after the sample excludes electrons scattered to high angles from the further imaging as indicated in Fig. 2.15. Additionally the

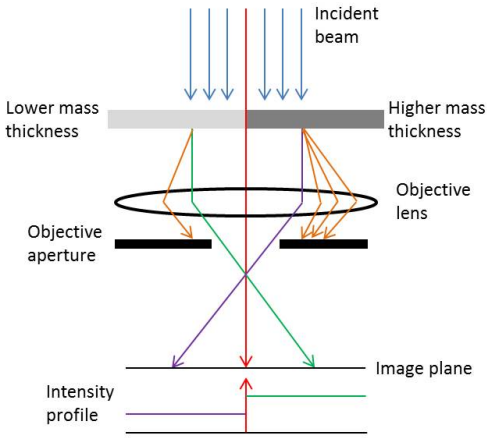

Figure 2.15: Schematic to illustrate the mass-thickness contrast. Samples with higher atomic number scatter more electrons to higher angles. By selecting only those electrons close to the optical axis those samples provide less intensity. Adapted from [94].

thicker a sample is the more scattering occurs and thus fewer electrons reach the detector. In the resulting image the sample has a lower intensity than the background. In summary, all electrons that strongly interact with the sample are prevented from reaching the detector by a simple aperture. This also includes absorbed or otherwise affected electrons but the strongest influence is the scattering from mass-thickness and crystal structure of the analyte.

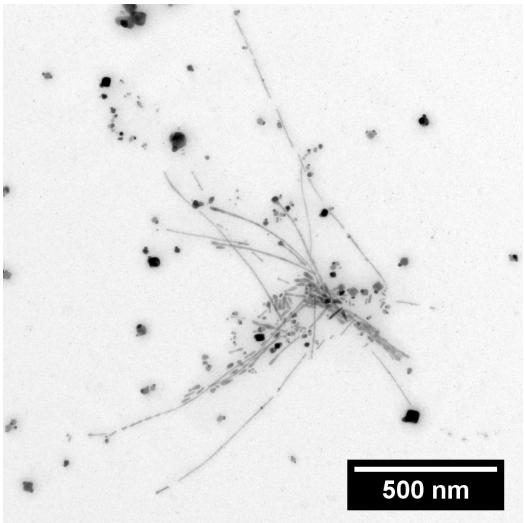

Figure 2.16: Characteristic example for an image acquired by conventional transmission electron microscopy (TEM) with a magnification of 10k.

A drawback of this method is that one needs material with a high mass-thickness for good contrast, so organics are poorly suited for this imaging mode. Nevertheless, this mode is most suitable for screening of samples since this method does not require specialized sample preparation and the images are easy to interpret. Fig. 2.16 shows a TEM image with a magnification of 10k. Visible are the inorganic nanowires and particles. The organic tubes surrounding the wires are not visible.

2.3.5 Cryogenic transmission electron microscopy

The structures investigated in this work are grown in aqueous solution and must be deposited on a TEM grid for imaging. These are commercially available with a variety of materials and shapes. Commonly used substrates for samples in solution are carbon films deposited over the TEM grids. The grids used here are circular with a diameter of 3.05 mm and are made of copper. One such grid usually has a mesh size between 200 to 400 bars per grid. The grid is coated with a thin film of amorphous carbon, typically 6-10 nm thick, which is essentially transparent for the electron beam. Fig. 2.17 shows one grid schematically. In the upper branch a detailed view of one such mesh with a side view and the dimensions for a 400 mesh grid is shown. Due to the hydrophobic nature of carbon film, the grids must be hydrophilized before an aqueous sample can be deposited. This is done by plasma treatment or by storing them over water soaked kimwipe over night. A 5-10 μL droplet of solution is deposited on the side of the grid coated with the carbon film. The excess liquid is wicked away after about a minute, taking care to avoid touching the surface of the grid. This leaves behind a sufficiently thin film for electron transmission. The whole grid is then stored until totally dried.

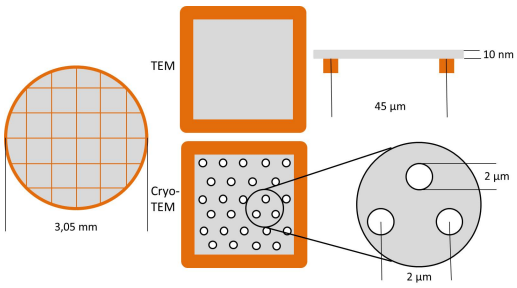

Figure 2.17: A spherical grid made of copper with a carbon film coated on the mesh is displayed at the left. The upper branch shows a typical grid for TEM with the cross-section for a grid with 400 meshes. The lower branch shows a grid for cryo-TEM with holes in the film and the dimensions.

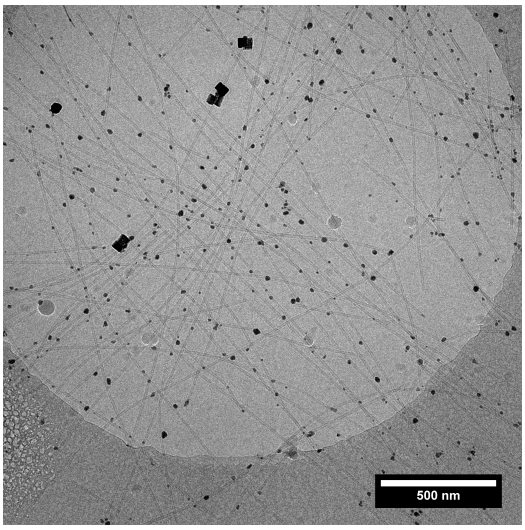

Figure 2.18: Example of an image taken with cryogenic transmission electron microscopy (cryo-TEM). Visible is a hole in the carbon film.

After this procedure the structures that were in the solvent are immobilized on the grids. These grids are poorly suited for imaging organics due to poor contrast. A possible solution for this is the use of cryogenic-TEM. Cryo-TEM is a very similar method to TEM for the imaging of organics. To overcome the problem of the low contrast of organic molecules that are laying on a carbon film, the film contains holes as indicated in Fig. 2.17 bottom for a grid with hole diameter of 2 μm and a distance of 2 μm between holes. The solution is dropped on the grid and the liquid bridges the holes due to capillary forces. After blotting away excess solution the whole grid is then shock-frozen, often by plunging into liquid ethane, so that the thin water film does not crystallize and stays amorphous. The preparation is sensitive to ambient humidity due to water in the air crystallizing on the cold sample and thus hiding the organics behind water crystals. Fig. 2.18 shows a J-aggregate sample with silver particles prepared the way described above with a hole in the carbon film visible. The organic nanotubes have a different contrast over the hole than over the carbon film.

2.3.6 High-resolution transmission electron microscopy

High-resolution TEM (HRTEM) in general refers to imaging in which lattice fringes (i.e. crystallographic planes) are observed or atomic resolution is achieved. The most important contrast mechanism for HRTEM is phase-contrast. To achieve a phase-contrast image the diffracted as well as the

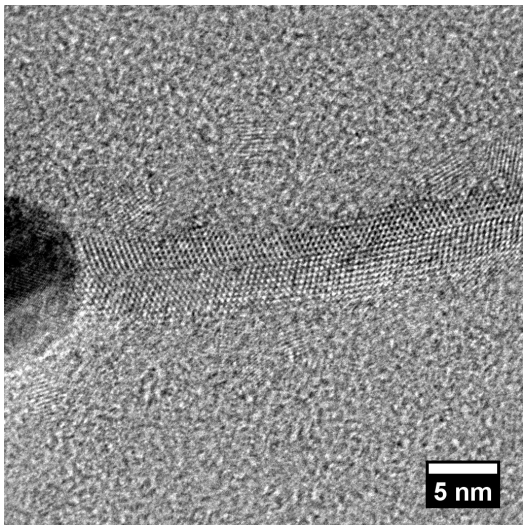

Figure 2.19: HRTEM of a particle and a wire. The lattice spacing of the wire is visible and reveals a single crystalline domain which contains a twin boundary.

unaffected beams are used for imaging. Phase-contrast images of the crystalline lattice are formed by removing the objective aperture entirely or by using a very large objective aperture. The incoming electron wave will be altered to an exit wave after passing the sample. This exit wave is a superposition of a (unaffected) plane wave and multiple waves diffracted by the sample. The diffracted beams are then re-united with the unaffected wave to the image wave. This image wave reaching the detector is a result of phase shifts and interference in the optical system of the microscope. The image wave collected by the electron detector contains the lattice spacing information of the crystalline structure but is not a direct mapping of the structure. This contrast mechanism is very sensitive to many factors, as for example the focus and astigmatism of the lenses. The properties of the specimen, as for example thickness and orientation, strongly influence the phase contrast as well. The latter is the reason HRTEM can be used to image the atomic structure of thin specimen. The images are more difficult to interpret than TEM images but allow for the highest resolution. Fig. 2.19 displays such a measurement for a nanowire attached to a particle. The lattice spacings of the wire are visible and reveal a twin boundary in the center.

2.3.7 Scanning transmission electron microscopy

For scanning TEM (STEM) the incident electron beam is focused to a very small diameter (usually $\oslash \approx 0.2$ nm) and this spot is then raster-scanned over

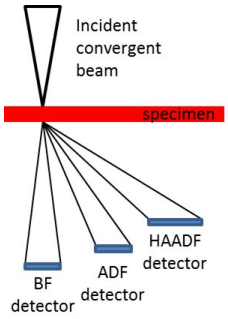

Figure 2.20: Illustration of detector arrangements for scanning transmission electron microscopy (STEM). The incident beam is concentrated to a small spot, which is then raster-scanned over the sample. For every spot, the intensity of the electrons is measured by either a bright field (BF) detector, an annular dark field (ADF) detector, or a high angle annular (HAADF) detector. Adapted from [94].

the sample. For the detection of the electrons several detectors can be used. Fig. 2.20 shows some possible detector arrangements. The contrast is due to amplitude contrast. In this work STEM was performed with a high angle annular dark field (HAADF) detector. In this case the strongly scattered electrons are exclusively selected. HAADF STEM is a dark field method where the contrast is inverted with respect to bright field methods, meaning brighter parts in the image belong to thicker and higher Z-number material then the darker parts. The detector is mounted exactly on the optical axis. He has a hole in the middle that is so large that all the electrons that do

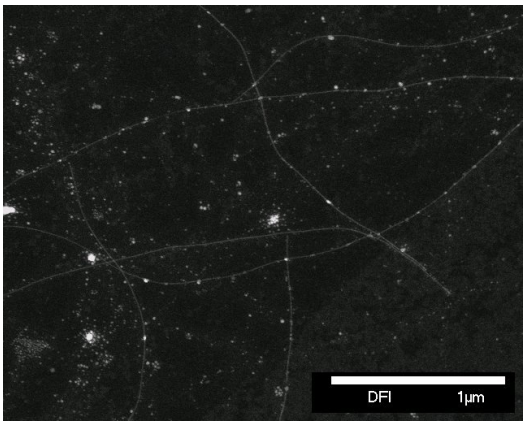

Figure 2.21: The method of HAADF STEM reverses the contrast similar to optical dark field microscopy. The more dense materials, such as the particles and wires, give a higher signal to the high angle detector, leading to brighter spots than the background.

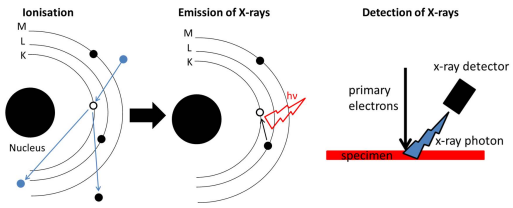

Figure 2.22: Sketch to illustrate the principle of energy dispersive x-ray spectroscopy (EDXS). Inelastic collisions of electrons result in the transfer of energy to the scattering material. The energy can be released by emitting a X-ray photon.

not scatter at large angles will not hit the detector. At each spot in the scan the electrons hitting the detector are integrated to give the overall intensity. The image is then a map of the measured intensities for every spot position. Since no magnification by lenses takes place the resolution is determined by the spot size of the electron beam. Fig. 2.21 shows a HAADF STEM image of inorganic nanowires and particles. The contrast is inverted with respect to TEM as in Fig. 2.16.

2.3.8 Energy dispersive x-ray spectroscopy

Energy dispersive x-ray spectroscopy (EDXS) is a technique that gives information about the chemical composition of the sample. Electrons can scatter elastically or inelastically. Inelastic collisions result in the transfer of energy to the scattering material. The incident beam may excite an electron in an

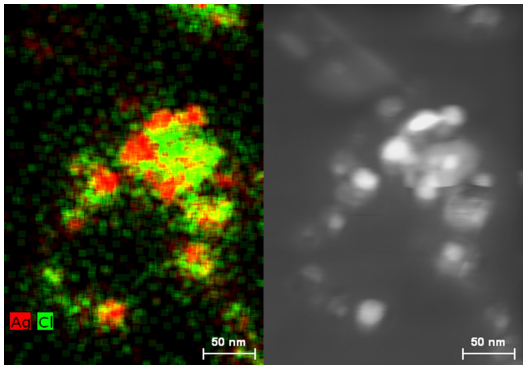

Figure 2.23: Energy dispersive X-ray spectroscopy (EDXS) mapping with the corresponding STEM image of a sample containing silver as well as silver chloride. For this mapping, EDXS spectra have been taken for every point in the STEM raster and the normalized peak intensities for silver (red) and chloride (green) are shown with their corresponding color intensity.

inner shell, ejecting it from the shell while creating an electron hole where the electron was. An electron from an outer, higher-energy shell then fills the hole, and the difference in energy between the higher-energy shell and the lower energy shell may be released in the form of an X-ray as shown in Fig. 2.22. These photons can not only be detected but also analyzed in terms of its energy. The used silicon drift detector measures the energy of an incoming photon by the amount of ionization it produces in the detector material. This varying ionization produces varying charge and the number of charges can be related to the energy of the photon. These x-ray spectra are a fingerprint for the elements of the sample since every element contains an unique x-ray spectrum. EDXS spectra were collected in STEM configuration as indicated in Fig. 2.22. By generating x-rays with the strongly focused electron beam we gain insight into the elements within the electron spot. The lateral resolution is again determined by the spot size. A prominent feature is element mapping with EDXS, which allows for easy screening of a samples element distribution. A color is assigned to the peaks corresponding to one element. For every point in the STEM raster a spectrum is taken and the elements are displayed with their respective color coding. The intensities of the colors correspond to the relative intensities of the respective element's x-ray peaks. Such a mapping is depicted in Fig. 2.23 on the left for silver in red and cloride in green with the corresponding STEM image on the right.

2.3.9 Selected area electron diffraction

Selected area electron diffraction (SAED) is a diffraction technique with electrons. The wavelength of the accelerated electrons is about a hundred times

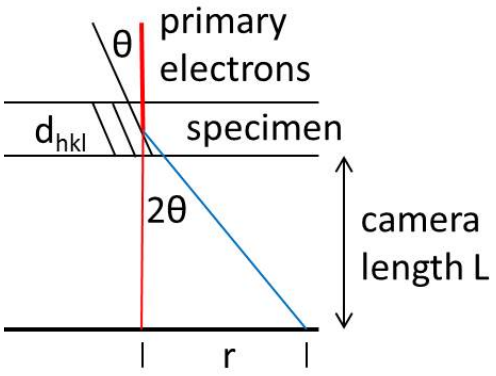

Figure 2.24: Selected area electron diffraction (SAED) illustration. See text for explanation.

smaller than the spacing between atoms in a solid. The lattice planes of a crystalline sample act as a diffraction grating to the high-energy electrons. Parts of the electrons will be scattered to particular angles determined by the crystal structure of the sample as described by the Bragg equation. The resulting image on the screen is a series of spots and each spot corresponds to a satisfied diffraction condition of the sample's crystal structure. The resulting diffraction pattern contains information from the whole area of the specimen that we illuminate with the beam. Due to polycrystalline or buckled samples, it is often of interest to select a certain area of the sample to contribute exclusively to the diffraction pattern. This is done by inserting a simple aperture, the selected area diffraction aperture, in the image plane of the objective lens. This creates a virtual aperture at the plane of the specimen and any electron that hits the specimen outside the area defined by the virtual aperture is excluded from contributing to the diffraction pattern. All SAED pattern share a bright spot in the center which is the unaffected beam. The other spots are displayed on the screen with a certain distance r to this central beam spot as shown in Fig. 6.4. With the camera length L it is possible to calculate the diffraction angle, the Bragg angle, which is half the angle between the diffracted and the unaffected beam. According to Bragg's relation we can now assign those angles to a lattice plane distance. For small angles($sin\theta = \theta$).

$$\lambda = 2d_{hkl}\theta$$

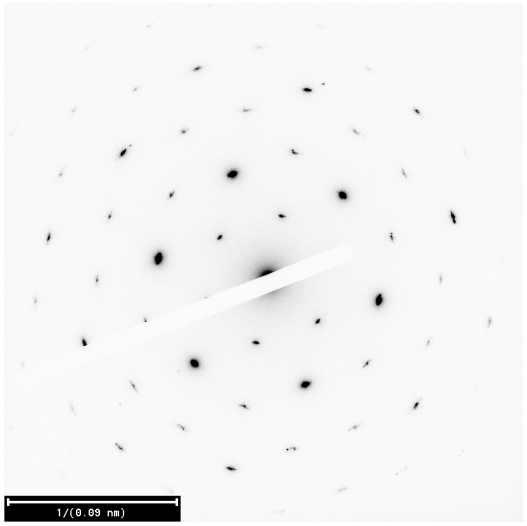

Figure 2.25: Selected area electron diffraction (SAED) pattern of the silver fcc lattice in [110] orientation. The contrast is inverted.

or with $\frac{r}{L} = 2\theta$

$$r = \lambda L \frac{1}{d_{hkl}}$$

Sharp spots appear only when the beam is diffracted by a single crystal. In many materials there are many crystals with different orientations. SAED of polycrystalline materials gives ring patterns analogous to those from X-ray powder diffraction, and can be used to identify texture and discriminate nanocrystalline from amorphous phases. Fig. 2.25 is a diffaction pattern of single crystalline silver in [110] orientation and contains an arrangement of sharp points. The contrast is inverted.

Chapter 3

Materials and methods

3.1 Preparation of J-aggregates

The cyanine dye $3,3' - bis(2 - sulfopropyl) - 5,5',6,6' - tetrachloro - 1,1' - dioctylbenzimida - carbo - cyanine$ (C8S3) was obtained from FEW Chemicals as a sodium salt with a molecular weight of 902.8 $gmol^{-1}$, and used as received. The double-walled nanotubular J-aggregates were prepared via the so-called alcoholic route [101]. A 2.9 mM stock solution was prepared by dissolving the dye in methanol (ROTISOLV $>$ 99,9% UV/IR-Grade) with stirring at 120 rpm in brown glass vial (Fisher Scientific). The stock was stored with avoidance of light. For the preparation of the J-aggregates, 130 μL of stock solution were added to 500 μL ultrapure DI water (Siemens Protegra CS, 14 $M\Omega/cm$) and stored in the dark for 24 hours to allow for aggregation. An additional 500 μL ultrapure DI water was then added to the solution to stabilize the formed aggregates. The final solution composition is 100:13 water/methanol by added volume with a final dye concentration of $3.36 * 10^{-4}$ M. The process is accompanied by a color change from the orange

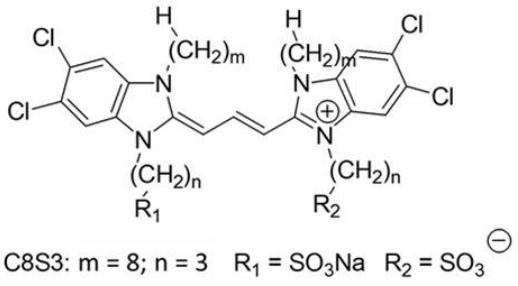

Figure 3.1: Chemical structure of amphiphilic cyanine dye 3,3-bis(2-sulfopropyl)-5,5,6,6-tetrachloro-1,1-dioctylbenzimidacarbocyanine (C8S3) as a sodium salt.

stock solution to a pink color for the J-aggregates. Further modifications by addition of other materials were performed within 24 hours after solution preparation to prevent aging effects of the J-aggregates such as bundling.

3.2 Preparation of nanowires and addition of sodium chloride

11 μL silver nitrate at a concentration of 100 mM in water was added to 400 μL of freshly prepared J-aggregate solution in a clear glass vial (Fisher Scientific) and then illuminated by 420 nm light for one minute employing the Xenon lamp of a Jasco FP-6500 fluorescence spectrometer. After illumination, the samples were stored in the dark during the subsequent growth of the nanostructures. 11 μL sodium chloride at a concentration of 100 mM in water was added to 411 μL silver nitrate/C8S3 solution.

3.3 Absorption spectroscopy

Absorption spectra were taken with a double-beam UV-Vis spectrometer (Shimadzu UV-2101PC). Quartz cells (Hellma GmbH) with path lengths of 0.2 mm and 2 mm were used. The spectra were always measured against a reference containing the blank solvent and normalized to the same path length of 1 cm.

3.4 Transmission electron microscopy

Conventional TEM and cryo-TEM measurements were made using a JEOL JEM2100 at a beam energy of 200 keV (LaB_6 cathode). High-resolution TEM and energy-dispersive X-ray spectroscopy (EDXS) were performed with a JEOL JEM2200FS at a beam energy of 200 keV (field emission gun). Selected area electron diffraction was performed on both instruments. Prior to sample deposition, the grids were hydrophilized by overnight incubation with water vapor. Conventional samples were prepared by depositing a small (five μL) droplet of solution on a 400-mesh carbon film supported copper TEM grid (Plano GmbH, item S 160) and removing the excess liquid by blotting with filter paper after ten minutes. Cryo samples were prepared by putting a droplet of the sample (five μL) on a perforated (two μm hole diameter) carbon film grid (Quantifoil R2/2 200 mesh). Excess sample solution was blotted using filter paper and the grids were immersed in liquid

ethane using a Vitrobot Mark IV (FEI, Eindhoven, Netherlands) to vitrify the aqueous film. CrystalMaker Software Ltd was used for simulating the measured crystal structures and SAED patterns. The necessary information of the crystals were obtained from the Crystallography Open Database (http://www.crystallography.net/cod/) and can be found with their respective identification numbers:

crystal	**COD ID**
silver	9008459
silver chloride	9008597
β-silver iodide	1011025
γ-silver iodide	9008829

Simulations for the HRTEM image have been performed with QSTEM (https://www.physics.hu-berlin.de/en/sem/software/software_qstem) [102].

Chapter 4

Results and discussion

The growth of silver structures at the walls of the tubular J-aggregate formed by the C8S3 was shown in previous publications to result in the growth of particles[36] or wires [1]. This work focuses on the growth of high-aspect ratio nanowires within the inner space of the double-walled tube. This chapter is divided into two parts dealing with two issues separately.
In the first part, the growth kinetics are studied in terms of morphology and material transport. By following the process of nanowire formation from the first visible crystallites to homogeneous wires with TEM, we gain insight into the whole growth process. Investigations of the early phases of this process allow for clarification of the nucleation process. The resulting structures at later times shed light on the material transport supporting the growth of the wires. When left to themselves, the nanowires growth eventually exceeds the outer diameter of the tube. A strategy is presented to prevent this overgrowth. In the end of the first chapter, a preliminary model for the growth of the wires based on these findings is presented and discussed. This part follows closely the recent publication based on this work [2].
In the second part, the crystal structure of the resulting materials is observed. A detailed analysis allows for unambiguous identification of the nanowire's composition. In previous publications the wires were identified as pure silver [1][2]. However, it will be proposed that the wires are silver iodide crystals. The analysis of particles outside the template which consist of pure silver led to the misconception that the wires are pure silver as well. Additionally the source of the iodide ions was only in hindsight found to be impurities of the dye powder. In the end the results from the two separate sections are put together and a more complete model for the growth of high-aspect ratio silver iodide wires is presented.

4.1 Nucleation and growth

This section focuses on the morphology of the wires grown with the tubular J-aggregate acting as a template and closely follows our publication [2]. The basic principles of the experiment are summarized in the fundamentals chapter, since they were established in previous work [1]. The growth of the wires within the inner volume of the tubular template is accompanied by changes in the optical spectra of the J-aggregate. Those changes are again monitored to determine relevant time points at which to prepare the samples for TEM. The reaction kinetics, which are in the order of hours to days, allow for "ex-situ" investigations by TEM. Based on the spectral changes the growth was separated into three phases: the "early growth phase", at which first nucleation and the subsequent evolution of these nuclei to stable crystallites takes place. This is followed by the "main growth phase", where the crystallites coalesce into a wire following the structure of the organic template. Since many nuclei form in the same aggregate and then converge during the "main growth phase", the process of material transport for the growth is discussed. After two days of growth time the wires reach a "desired" state at which they homogeneously fill the whole template. The growth then continues over the diameter of the template due to the excess of silver ions. A strategy is presented to prevent this "over-growth" by removing the remaining silver ions by precipitation with chlorides. It turns out that the wires can be affected by the addition of the extra ions as well. A first model for the growth and the manipulation of the wires is presented and discussed.

4.1.1 Kinetics followed by optical spectroscopy

The nucleation and growth of inorganic nanowires in the J-aggregate solution can not be followed "in-situ" by TEM since the preparation of the TEM-grids requires drying of the solution on a carbon film to immobilize the aggregates [37]. To observe the formation and growth of the nanostructures, they have to be fixed on a TEM-grid at defined time steps during the growth and be examined "ex-situ". It was demonstrated in previous experiments [65] that during the growth phase the absorbance decreases and changes in the shape of the spectrum are observed. These changes can be explained by oxidation of the C8S3 dyes that does not change the structure of the aggregates using silver ions as an external reducing agent. The controlled oxidation of a pure J-aggregate solution with cyclic voltammetry (CV) was observed via optical absorption spectroscopy and allowed to correlate the observed spectral

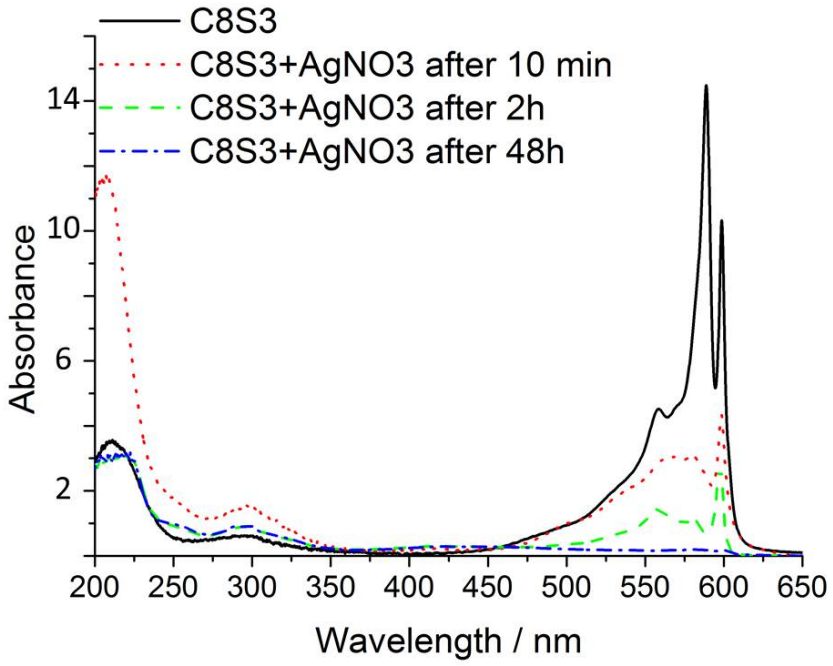

Figure 4.1: Absorption spectra of **black:** a pure J-aggregate (C8S3) solution, **red:** aggregate solution with added silver nitrate and ten minutes after illumintaion, **green:** two hours after illumination, and **blue:** two days after illumination. The spectra reveal a fast oxidation of the dyes within the first ten minutes which is slowed down after two hours and completed after two days. All spectra are scaled to a path length of 1 cm.

changes with an oxidation of the nanotubes [66]. The change in conjugation length leads to a change in the optical spectra as can be monitored by absorption spectroscopy. It is important to notice that the oxidation of the dyes only modifies the conjugated π-electron system but does not decompose the molecules [67], which explains why the absorbance vanishes despite the morphology remaining unchanged. CV experiments with a J-aggregate solution, where silver nitrate has been added and illuminated, provided a response associated with the oxidation of silver, confirming the formation of neutral silver within the solution [64]. Additionally, cryo-TEM observations showed that only few aggregates are neither filled with a wire nor decorated with particles. The proposed mechanism for the formation of silver nanostructures in a J-aggregate solution was a localized redox chemistry at the walls of the tubes, where the silver ions get reduced by the dyes within the tubular aggregate.

Investigation of the optical changes during addition of silver nitrate allows us to define reasonable time steps at which to prepare the grids for TEM. A typical behavior is shown in Fig. 4.1 where silver nitrate was added to a freshly prepared J-aggregate solution and illuminated with 420 nm blue light for one minute. A spectra were collected before the addition of silver nitrate and then 10 minutes, 2 hours, and two days after adding silver nitrate and illuminating with blue light. No spectra were collected prior to 10 minutes for practical reasons. The unadulterated C8S3 solution that did not have any silver nitrate added (black) shows the typical J-aggregate behavior for this dye, namely two strong excitonic absorption bands at 590 nm and 600 nm. Ten minutes after addition of silver nitrate and illumination (red) the absorbance of the aggregates is already halved, indicating that first reduction of silver ions by the dyes has taken place. Two hours after illumination (green) the aggregates have a strongly reduced absorbance while after two days (blue) the dyes are almost completely oxidized resulting in only a very slight absorption at around 605 nm. The strong decrease of the J-band

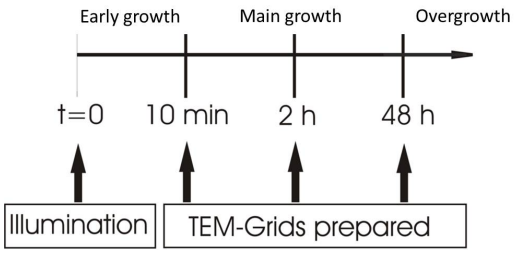

Figure 4.2: Time line illustrating the three growth phases and the time at which samples for TEM have been prepared.

absorbance within the first ten minutes indicates that most of the dyes are oxidized during that time. Further reduction of absorbance happens within the next two hours at which point the oxidation of the dyes is slowed. After two days the J-band absorbance vanishes and no more oxidation of the dyes is visible.

"Ex-situ" investigations are possible because the nanowire growth rate is slow enough to permit the preparation of several TEM grids within the interesting growth phase. Samples taken during the first ten minutes may give insight into the formation of nuclei with further nucleation happening within the first two hours. After two days no crystal growth due to a redox reaction with the dyes is possible since the dyes are completely oxidized. We call the time within the first two hours where the first nucleation takes place the "early growth phase". This is followed by the "main growth phase", which continues up to two days after illumination, where the crystallites grow into homogeneous wires. Despite no further changes in the absorption spectra samples taken after two days reveal a continuation of the growth called "overgrowth" which is also described in detail in the following investigations.

4.1.2 Early growth phase

To observe the formation of nuclei, samples for TEM need to be prepared directly after illumination. Cryo-TEM allows for the fastest sample preparation because the shock-freezing results in a good snapshot of the sample at that time. Due to the time needed to prepare the TEM grids, the shortest possible time was around three minutes. This was shorter than the ten minutes needed for the absorption spectroscopy.

Figure 4.3 shows a cryo-TEM image of a sample shock frozen three minutes after illumination. Images at this time step mostly show bare tubular J-aggregates, as identified by the parallel lines and previously analyzed in detail [35][65]. Few silver nanocrystals were found mostly located adjacent to the aggregates, either along the tube, or at the tube ends. Infrequently, small pieces of nanowires are found that are obviously located within the tubular aggregates and following their shape. In Fig. 4.3 one such piece is marked by a circle. The dark gray shaded area with grainy structures in the lower left corner of the image is an artifact due to the boundary of the Quantifoil film. Possible smaller nuclei and the emerging crystallites are too small to be directly visualized by TEM. Other imaging methods, such as scanning probe microscopy, also failed due to insufficient lateral resolution and low contrast between nuclei and aggregates. Therefore, the locations where nuclei have been formed can only be found indirectly from the location of the silver nanocrystals that are visible. It is possible, that there are other nuclei

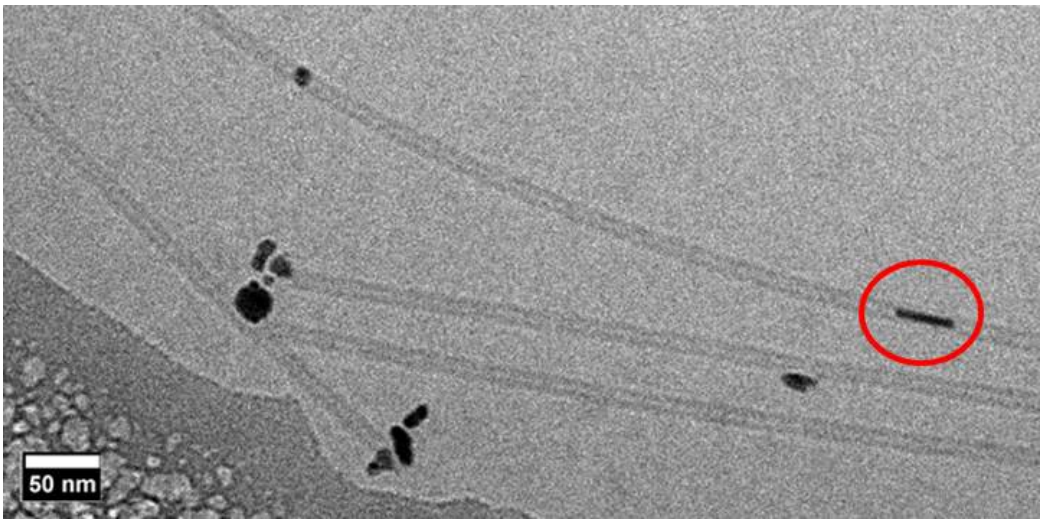

Figure 4.3: Representative cryo-TEM image of tubular C8S3 J-aggregates and a few nanoparticles (black objects). A small piece of a wire in the aggregate was located and marked by a red circle. The image was taken from a sample prepared for cryo-TEM three minutes after illumination.

which are too small to be visualized by TEM.

4.1.3 Main growth phase

Typical features of the main growth phase are depicted in Fig. 4.4 and Fig. 4.5 with conventional TEM, because it allows for fast screening of many samples and the features of interest are just as easy to identify. Fig. 4.4 is a sample that was prepared two hours after illumination. While at the very short times, represented by Fig. 4.3, only very short pieces of nanowires are found sporadically, after about two hours somewhat larger fragments of wires are visible. The piecewise wires are obviously following the shape of the tubular aggregates. The wire fragments have a broad length distribution in the range of 20-500 nm. In comparison to the early growth phase (Fig. 4.3), the main growth phase has more crystallites forming within the aggregates, as can be seen by the higher density of wire fragments and spherical particles. No single isolated short wires are visible anymore. More detailed inspection of images at this early stage of the main growth phase shows that those pieces of wires are either adjacent with a globular crystallite (dotted red circle), or are alternating with such globular crystallites (see insert in Fig. 4.4 blue circle). The spherical crystallites (for which the contrast is not in saturation) provide a homogeneous contrast along a single particle in TEM which is similar for all of them. This is contrary to the wire pieces, which have inhomogeneous

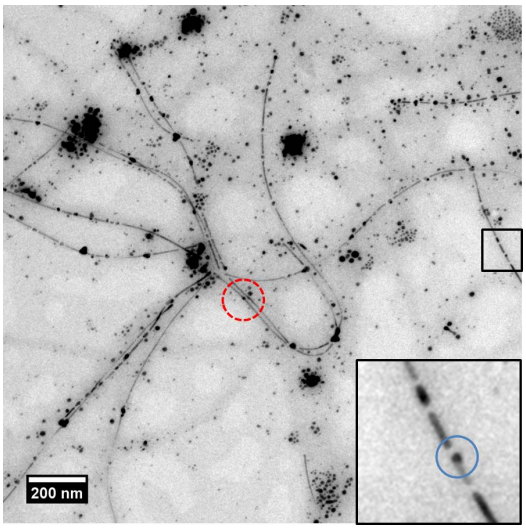

Figure 4.4: Typical TEM images of samples immobilized on a TEM grid after two hours of growth time. The wires are either combined with a globular crystallite(red dotted circle) or pieces of wires are alternating with such globular particles (blue circle in the insert).

contrast along a single piece and variable contrast between fragments.

The wire fragments grow with increasing time until they completely fill the aggregates to form wires with homogeneous diameters of 6.5±0.5 nm and lengths exceeding microns, as shown in Fig. 4.5. After about 48 hours, no

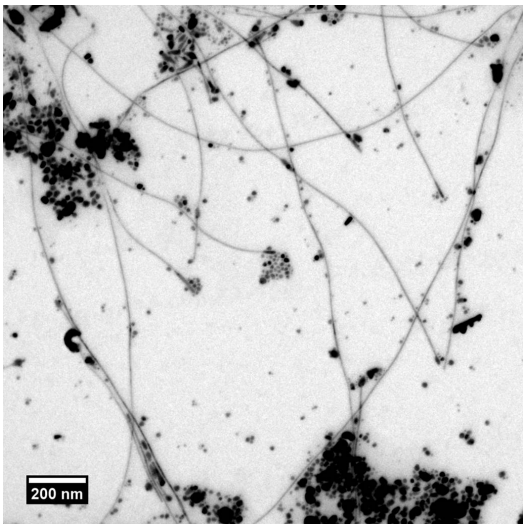

Figure 4.5: Typical TEM image taken after 24 hours of growth time. The piecewise wires have coalesced to continuous high aspect ratio nanowires.

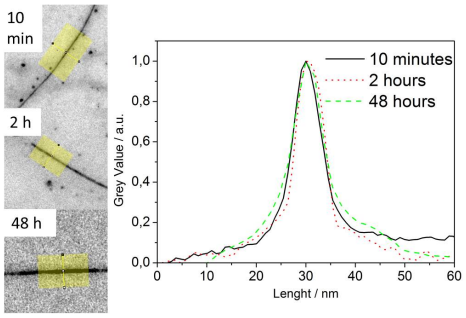

Figure 4.6: Linescans of the wires after ten minutes, two hours, and two days of growth time. The FWHM is the same for all three growth times.

short wire fragments could be found. Linescans of the wires at all of the three time steps as seen in Fig. 4.6, convincingly prove that the growth of these pieces only takes place in length and not in diameter.

Besides the growth from short pieces to wires, a remarkable coexistence of different motifs was found and is best presented by cryo-TEM imaging. A typical situation is depicted in Fig. 4.7, where a sample is prepared ten minutes after light exposure. Bare aggregates (i) are still visible together with aggregates filled with long silver wires (ii) and aggregates decorated by small (less than five nm diameter) nanoparticles (iii). All three types of structures

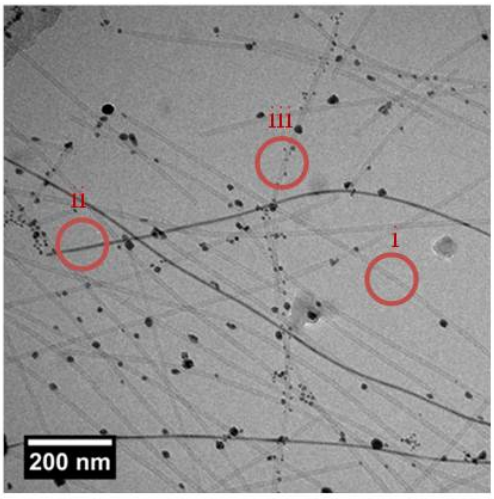

Figure 4.7: Cryo-TEM image showing the J-aggregates and crystallites after ten minutes growth time. A coexistence of three different motifs was observed for all samples: (i) bare aggregates, (ii) filled aggregates, and (iii) aggregates decorated by particles.

are sparsely decorated by larger particles about 10-20 nm in diameter. These large particles were always found. They are considered as an "unavoidable background" and, because of their sparse appearance, are not considered in the following discussion. Interestingly, no aggregates can be found that are both filled inside with a nanowire (case ii) and at same time decorated outside with small particles (case iii). The three motifs observed are found in parallel during the whole growth phase, but in different proportions. This observation makes it difficult to define precise growth kinetics for the wires. Another observation to note is that the wires already fill the whole template without being interrupted but with a variable contrast along a wire. TEM images at later time show repeatedly interrupted wires as in Fig. 4.4 after two hours growth time. This difference observed for the different TEM methods can be attributed to the cryo imaging where the sample is embedded in ice, which induces less harm to the sample. Also structurally weaker parts of the crystal remain intact, but they give less contrast. This is in contrast to conventional TEM, where the weaker parts of the wires get dissolved by the electron beam (see discussion, Fig. 4.19). This "preserving" effect of the cryo-imaging was later used to investigate the crystal structure of the wires.

4.1.4 Overgrowth

Fig 4.8 is a sample that was stored in the dark for six days after illumination. The structures seen are still wire-like in general appearance but with variable diameter and contrast along each wire. The diameter of the structures is non-uniform, ranging from several tens up to a hundred nanometers. The growth of the wires after completely filling the nanotubes after two days (Fig. 4.5) exceeds the confinement of the template. This "overgrowth" is due to the excess of silver ions present in solution and because the template is soft. This means that samples prepared and stored for longer than two days do not contain nanowires with a well-defined diameter and extreme high aspect ratio. Hence those structures are not of interest and are not analyzed further. These "overgrown" samples were used for optical dark field imaging, confirming the length of these structures reaches several tens of micrometer [1].

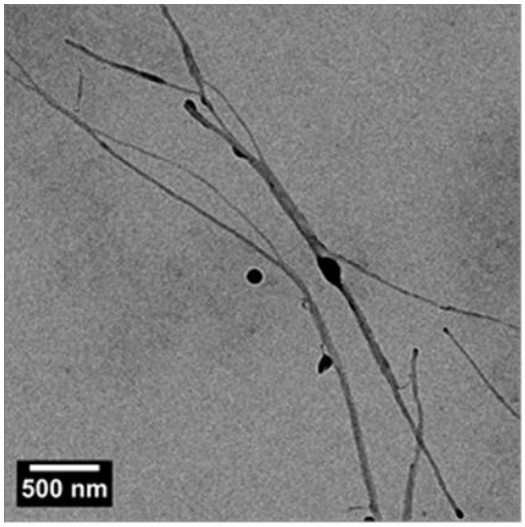

Figure 4.8: TEM image of a sample deposited on a grid six days after preparation. The structures have grown in diameter beyond the template diameter, leading to irregular structures with non-uniform and inhomogeneous thickness which is referred to as overgrowth.

4.1.5 Addition of chlorides

The growth of the wires continues after they homogeneously fill the template after two days (see Fig. 4.5). To prevent this "overgrowth" and stop the growth of the wires in solution, one has to remove the excess of silver. A straightforward approach is the removal of excess silver ions by precipitation of the remaining silver ions via addition of halides. Sodium chloride was used because it is pH-neutral and sodium ions are already present in the dye salt as counter-ions. Upon addition of sodium chloride, the residual silver ions precipitate according to the reaction:

$$Ag^{+}(aq) + Cl^{-}(aq) \longrightarrow AgCl(s)$$

For first investigations, the time of addition was chosen to be after two hours (see Fig. 4.9) as after that time the dyes still show a decent absorption but are almost completely oxidized (see Fig. 4.1). Only then can we effectively halt the redox reaction between silver ions and dyes thus reducing the source for elementary silver to gain a proof of principle for the whole idea. No noticeable reduction of silver with oxidation of the dyes takes place at a later point. Additionally, the remaining J-aggregate absorbance allows for spectral investigations. The chlorides were added in the same molar ratio as the initial silver concentration leading to an excess of chlorides ensuring complete precipitation.

Since the growth of the wires is accompanied by changes in the optical absorption spectra (see Fig. 4.1), the spectra were used to investigate the influence of the chloride ions. The effect of adding sodium chloride on the optical absorption is presented in Fig. 4.10. Spectra taken at different time steps for a sample without any added sodium chloride (Fig. 4.10**a**) are compared to the spectra for a sample where sodium chloride was added

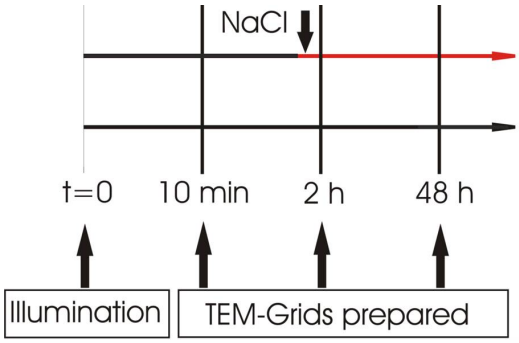

Figure 4.9: Schematic to illustrate the time steps for the addition of sodium chloride and the growth times.

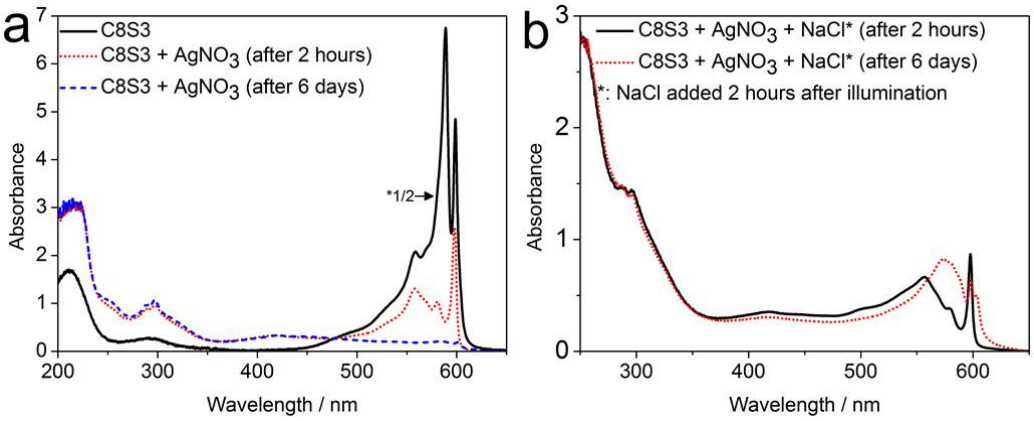

Figure 4.10: Absorption spectra of (a) pure C8S3 solution (scaled by a factor 1/2), a solution measured two hours after addition of silver nitrate, and a solution measured six days after addition of silver nitrate and (b) the same solution with silver nitrate and same time steps as in (a), but with the addition of sodium chloride after two hours. All spectra are scaled to a cuvette thickness of 1 cm except for the first, which is essentially scaled to 0.5 cm.

two hours after light exposure (Fig. 4.10**b**). Before addition of the sodium chloride, the aggregate spectra are identical in Fig. 4.10**a** and **b**. Sodium chloride was then added to the solution of Fig. 4.10b in a 1:1 molar ratio of silver to chloride. An increased absorption for wavelengths less than 300 nm is observed immediately after addition of the sodium chloride, which is attributed to the absorbance of silver chloride that has formed by precipitation. Six days after illumination a strong difference is seen between the spectra. In the solution where no sodium chloride is added (Fig. 4.10**a**) the aggregate absorption is completely vanished. A new absorption peak has developed around 400 nm, which can be attributed to the plasmon resonance of silver particles [103][104][105] or, as will be shown later, an absorbance of silver iodide nanostructures [106][107][108]. This spectral behavior is accompanied by the "overgrowth" of the silver nanowires due to free silver ions as described above. After this long time period not only the dyes are oxidized, but the J-aggregates are also structurally destroyed. In contrast, the sample where sodium chloride was added (Fig. 4.10**b**) still shows J-band absorption, although the shape of the spectrum has changed. However, the integrated absorbance of the J-band remains constant over the whole period of time. This preservation of the J-band indicates a prevention of further oxidation and destruction of the J-aggregate template because of the removal of excess silver ions by precipitation in the form of silver chloride.

The morphology of the structures was again observed via TEM. Sam-

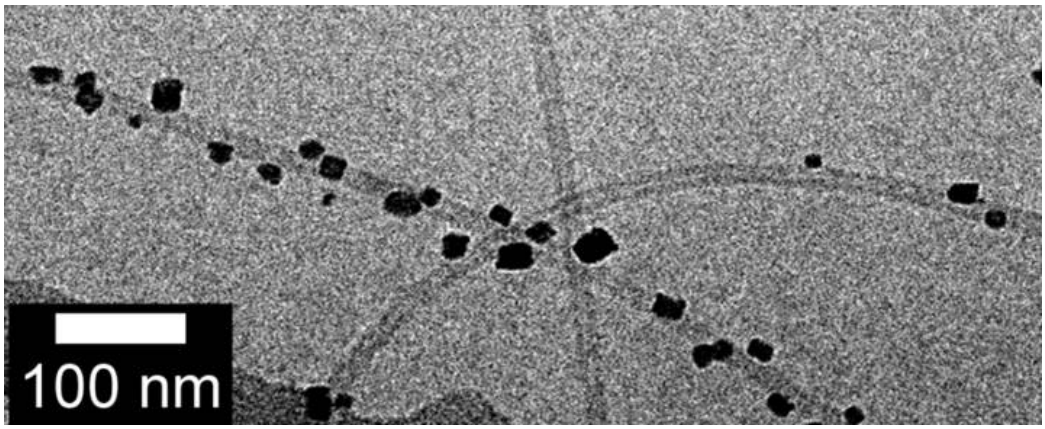

Figure 4.11: Cryo-TEM image of a sample where sodium chloride was added two hours after illumination. The sample was stored in solution in the dark for two days before inspection.

ples prepared immediately after addition of sodium chloride show the same features as without sodium chloride and shown in Fig. 4.4. The aggregates are repeatedly filled by fragments of wires and no influence of chloride is observed. Figure 4.11 shows a typical situation where sodium chloride was added two hours after illumination and imaged after two days growth time with cryo-TEM. Surprisingly, no wires are found anymore. Instead, cubic crystallites are observed that are attached to the template. The morphology of the template remains intact after addition of sodium chloride and dissolution of the wires.

4.1.6 Influence of oxygen

We added sodium chloride with the intent to remove excess silver ions and to stop the overgrowth of the wires. Surprisingly, we found that the wires disappeared due to presence of chloride ions. It was recently reported that silver nanocrystals in aqueous solution can be dissolved by chloride ions in a process called oxidative etching [109][110]. Silver ions gets reduced to their zerovalent form and these can be possibly oxidized back to their ionic forms. The oxidization is accompanied by an electron transfer from the reductant to an oxidant. Oxygen for example is a strong oxidizing agent. When an electrolyte is present the oxidation is greatly enhanced, because the electrolyte serves as a salt bridge by transferring charges from the reductant to the oxidant [111]. During the synthesis of silver nanocrystals the presence of chloride ions, combined with oxygen from the air, often resulted in significant changes to the crystallinity and morphology of the final products. The chloride acts

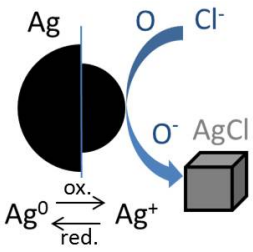

Figure 4.12: Schematic illustrating the oxidative etching in presence of oxygen and chlorides. The chloride acts as a ligand to facilitate the oxidation.

as a ligand facilitating the oxygen induced oxidation of silver atoms at the surface of the crystals (see Fig. 4.12). This leads to an electron transfer from the silver to the oxygen mediated by the chlorides and the resulting silver ions nucleate with the chlorides to silver chloride. This process leads to the dissolution of the crystals preferentially at the defects sites. In the literature, the etching is used to obtain single crystal silver nanoparticles in higher yield, demonstrating that particles containing defects are preferentially oxidized.

Fig. 4.13 shows a TEM image of a sample were sodium chloride was added two hours after illumination and stored in the dark without deoxygenating the solution. With oxygen present in the solution no wires can be found and the aggregates are densely covered by cubic crystallites that could be identified as silver chloride. The insert in Fig. 4.13 shows a magnification where the distance between the crystallites is about 50 nm, which suggests that the cubes are attached to the outside of a bundle of four aggregates.

To gain further insight into this etching process, the experiments have also been conducted without oxygen. The solution was bubbled with nitrogen to remove the oxygen and was stored in the oxygen-free atmosphere of a glove-box. Fig. 4.14 shows a sample where sodium chloride was added two hours after illumination and the solution was stored for five weeks in an anaerobic environment. In that case, the same piecewise wires already present at the time of sodium chloride addition were found. This morphology remains stable even over weeks. The solution itself showed clear precipitation in form of flakes in both cases, providing visual evidence for the successful removal of excess silver ions. The oxygen dependent dissolution of the wires was also initially attributed to oxidative etching of silver. The influence of oxygen on the addition of sodium chloride is again discussed after the unambiguous identification of the wires as silver iodide in the next chapter.

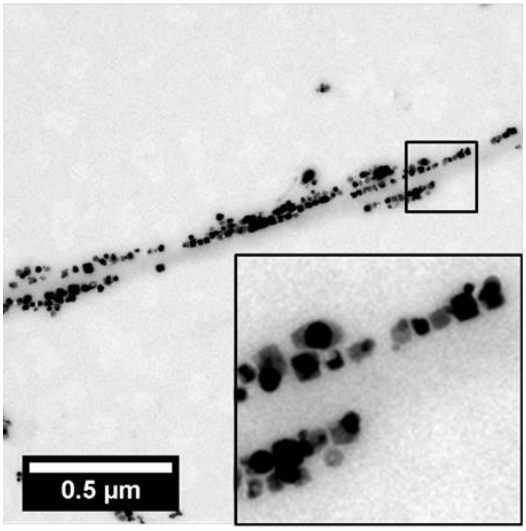

Figure 4.13: TEM image of a sample where sodium chloride was added two hours after light exposure but imaged after two days. The solution was not deoxygenated. The insert shows a magnified view of the marked area where the distance between the two rows of particles (≈ 50 nm) indicates that a bundle of aggregates is covered.

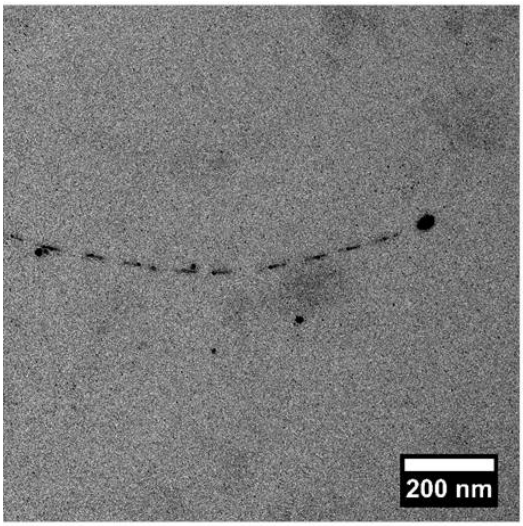

Figure 4.14: A similar sample as in Fig. 4.13 but prepared with exclusion of oxygen and inspected after storing for five weeks in oxygen free environment.

4.1.7 Multiple stranded cable

The growth process of inorganic nanowires can also be extended to the use of different tubular J-aggregates. In a first proof of principle this was performed for the very similar dye C8O3. Fig. 4.15 provides a comparison between the C8S3 and the C8O3. The dyes differ in the polar side groups, which are two carboxyl-groups (COOH) for the C8O3 instead of the sulfonate groups (SO_3) for the familiar C8S3. The C8O3 aggregates to tubes as well but with a smaller diameter of $10 \pm 1\ nm$ [35]. The resulting tubes show strong bundling with a random helicity and a bundling periodicity that depends on the number of tubes twisted. By performing the same experiment as for the wire formation within the C8S3, namely addition of silver nitrate with the same concentration as for the C8S3 and illumination @ 420 nm for one minute, they could be used as template for the growth of inorganic wires as well.

Fig. 4.16 displays a TEM image two days after the illumination. Visible is a multiple strand of wires oriented along an elongated structure with a diameter of approximately 30 nm. The line scan in the image shows that the wires are arranged in parallel with a remarkably homogeneous diameter and distance between them. In some parts of the image the whole structure is filled by parallel wires while in other parts only in one half of the structure

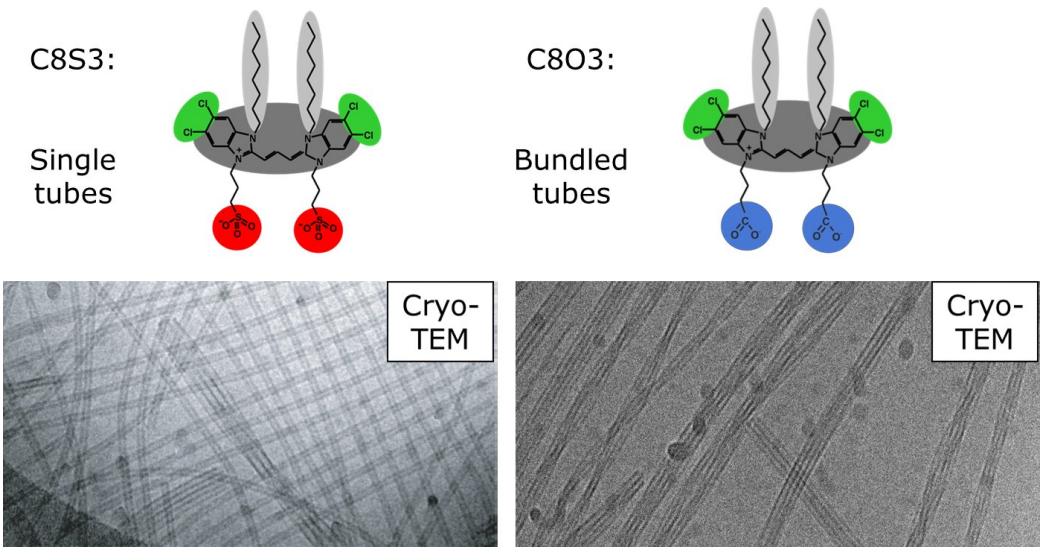

Figure 4.15: Comparison of the two dyes C8S3 and C8O3. They differ by their polar side groups, which are sulfonate groups (red) for the C8S3 and carboxyl-groups (blue) for the C8O3. They both form nanotubes upon aggregation in aqueous solution, but the tubes from the C8O3 show strong bundling.

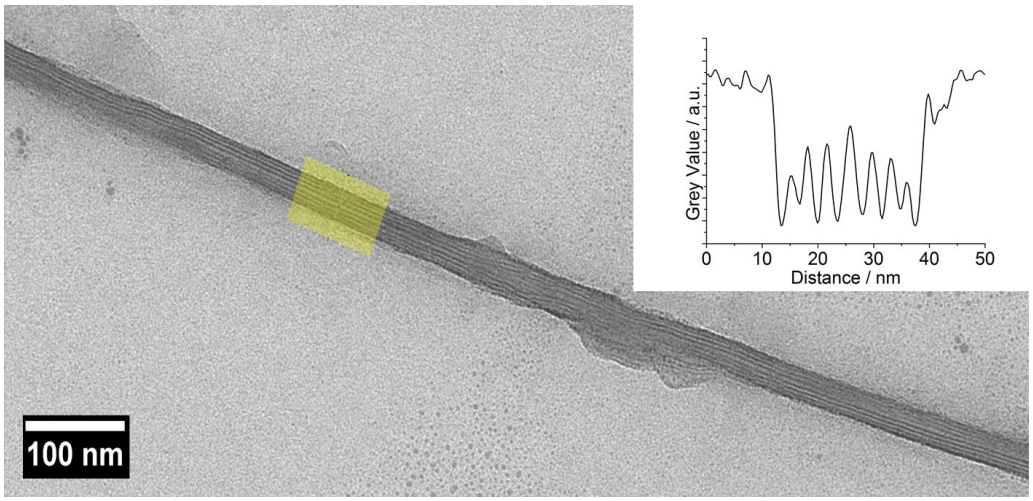

Figure 4.16: TEM image of a C8O3 solution two hours after addition of silver nitrate and illumination with blue light @ 420 nm for one minute. The line scans shows that the resulting wires are arranged in parallel with a well defined diameter and distance between them.

wires are visible. The varying arrangement of the wires can be explained by the twisting of the bundles of the C8O3. These multiple stranded cables are very promising in the application of these systems, since they could posses a much higher mechanical stability and are probably much less sensitive to structural defects than a single nanowire.

4.1.8 Particle analysis

It was shown in the previous section that the stability of the wires upon addition of sodium chloride depends on the presence of oxygen. For oxygen containing samples the wires are dissolved, whereas in absence of oxygen both the wire and C8S3 tubule morphology remain intact. To confirm the suggested dissolution of the wires due to oxidative etching, the resulting particles were analyzed with selected area electron diffraction. For comparison, the same method was applied to the deoxygenated sample as well. The solutions showed precipitation independent from oxygen concentration, so excess silver ions have been removed from solution in both cases. Investigated here is only a possible change from silver to silver chloride for the particles attached to the template when oxygen is present. Due to the dissolution of the wires in samples containing oxygen, only the particles are analyzed for comparison between aerobic and anaerobic samples. SAED allows for characterization of the crystal structure of the particles and hence differentiation between silver

and silver chloride. After addition of sodium chloride and two days growth in the dark, silver chloride particles have formed in the oxygen containing samples and none have formed in the deoxygenated sample. Together with the oxygen dependent dissolution of the wires, this strongly supports the proposed mechanism of oxidative etching. The next chapter focuses on the more experimentally challenging analysis of the crystal structure of the wires, although SAED provides first indication for the presence of silver iodide.

4.1.9 Crystal analysis of particles in an oxygen containing sample

The experiments shown here have been performed without illumination, thus no wires are present in the samples. Sodium chloride was added to the sample two hours after addition of silver nitrate and the grids were prepared after two days growth time. No effort was made to remove oxygen from the solution. Fig. 4.17 **a** is a conventional TEM image for such a sample. Particles in various sizes ranging from several up to almost a hundred nanometers can be identified. The morphology of the particles is spherical and especially the bigger ones have inhomogeneous contrast under TEM. The particles are arbitrarily distributed showing no alignment relative to the elongated template. Fig. 4.17 **b** is the selected area electron diffraction (SAED) pattern obtained from the region in the Fig. 4.17 **a**. The pattern consists of two distinctive rings close to the center followed by a smeared disk and two weaker rings at the outside. Since no discrete Bragg spots or symmetry can be seen, the pattern is a superposition of crystals in different orientations. Comparison with the TEM image is in agreement with the observed pattern, e.g. many particles, which can have any orientation. For a better evaluation of this measurement a circularly integrated intensity plot of the pattern is shown in Fig. 4.17 **c**. Within the radial plot of the SAED the lattice plane distances of silver (red) and silver chloride (blue) are plotted with their relative intensities and the prominent ones are indexed. Tab. 4.1 displays the measured mean values for the distances and a summary of all the theoretical lattice plane distances for silver and silver chloride in the measured region as also shown in Fig. 4.17 **c**. The crystals contain lattice plane spacings for both structures and from the relative intensities one may estimate a content of 20% - 30% of AgCl. Additionally, the lattice plane distances for $\beta - AgI$ (green) are shown but cannot explain any of the peaks. Hence, no AgI crystals are present in the measured area. These experiments confirm the formation of silver chloride upon addition of sodium chloride in presence of oxygen.

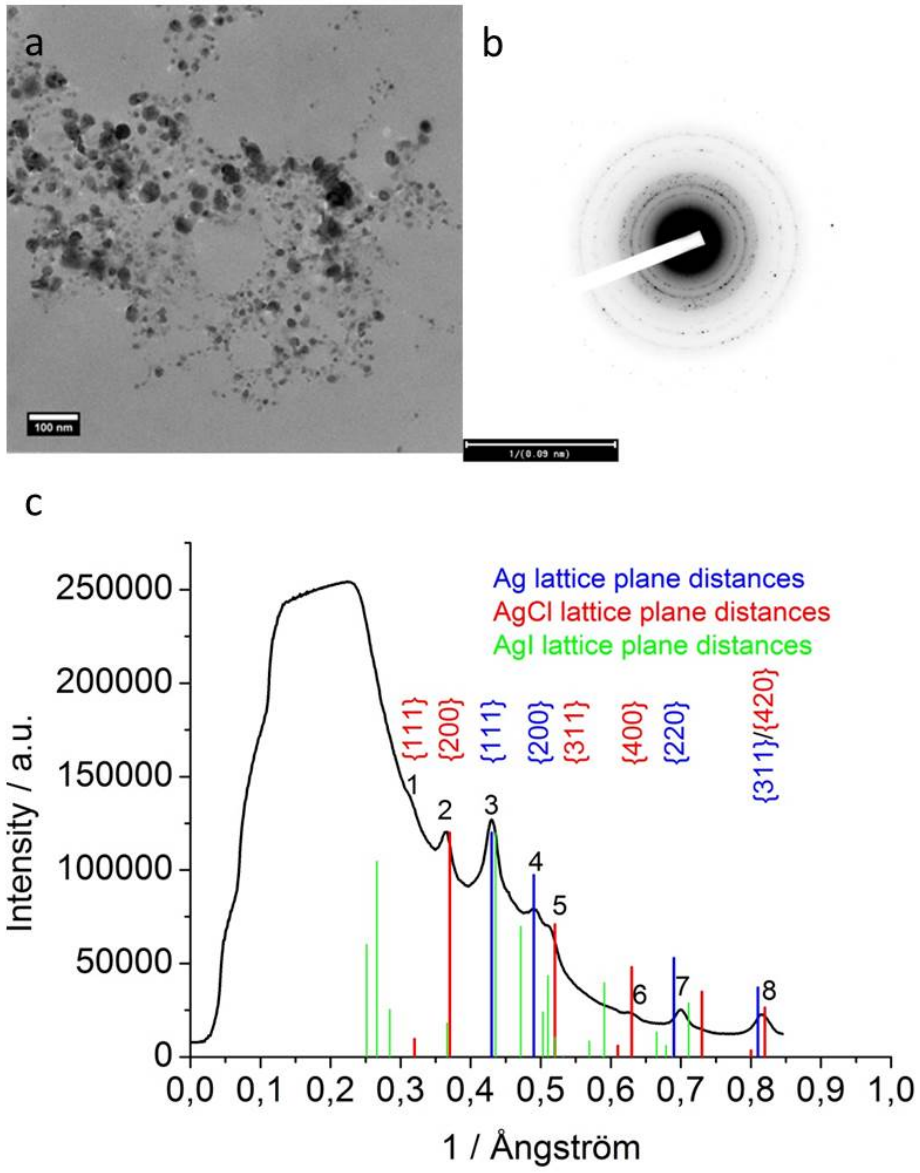

Figure 4.17: Silver and silver chloride particles grown without removing oxygen from the solutions. **a**: TEM image of particles, **b**: electron diffraction pattern of the region shown left. **c**: radial scan of the diffraction pattern with calculated lattice planes for silver, silver chloride, and $\beta - AgI$ indicated. The diffraction pattern can be explained by superposition of the most prominent Bragg reflections (indicated with respective color) of silver and silver chloride.

Table 4.1: Mean value for the measured distances and the most prominent lattice plane distances for silver chloride and silver with the fitting ones are marked with bold font.

measured mean value		Silver Chloride		Silver	
Peak number	d_{hkl} [Å]	hkl	d_{hkl} [Å]	hkl	d_{hkl} [Å]
1	**3.17**	**111**	**3.13**		
2	**2.78**	**200**	**2.70**		
3	**2.33**			**111**	**2.33**
4	**2.04**			**200**	**2.04**
5	**1.96**	**220**	**1.92**		
		311	1.64		
6	**1.61**	**222**	**1.58**		
7	**1.43**			**220**	**1.45**
		400	1.37		
		313	1.25		
8	**1.24**	**420**	**1.22**	**311**	**1.24**

4.1.10 Crystal analysis of particles in a deoxygenated sample

Fig. 4.18 is a similar analysis for a sample prepared the same way as described in Fig. 4.17, but in oxygen free conditions. The similar wire sample is shown in Fig. 4.14. In the TEM image Fig. 4.18 **a** many of particles are visible ranging from small spherical crystallites several nanometers in size up to big cubic structures tens of nanometer in dimension. The large cubic crystallites exhibit an inhomogeneous contrast, indicating that they are polycrystalline. The smaller particles are mostly randomly distributed, but some of them are aligned along an elongated structure which is most likely the J-aggregate. The influence of oxygen is already visible here, not only in the different morphology compared to the oxygen containing sample, but also in the perpetuation of the decoration of the tubes by particles. In Fig. 4.18 **b** the SAED pattern corresponding to Fig. 4.18 **a** is shown. The diffraction pattern consists of several diffraction peaks all aligned along circles but with no distinctive orientation or symmetry. The pattern is again a superposition of crystals in different orientations, as can be seen in the TEM image. Fig. 4.18 **c** is the radial plot profile of the SAED pattern. Within this plot the lattice plane distances of silver (blue) and silver chloride (red) are marked with the most prominent ones indexed with their relative intensity. Again

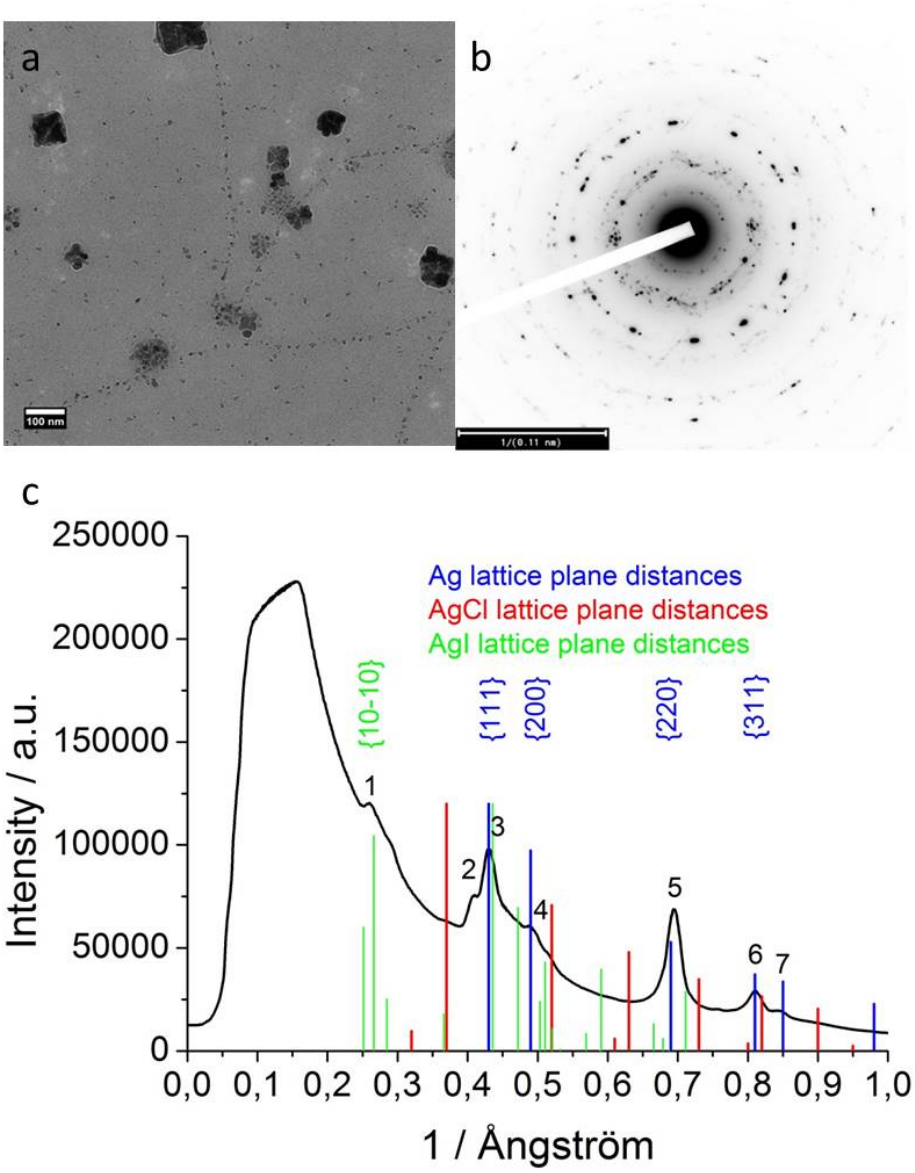

Figure 4.18: Silver and silver chloride particles grown in oxygen free solutions (bubbled with nitrogen) and stored in a glove box purged with nitrogen. **a**: TEM image of particles, **b**: electron diffraction pattern of the region shown left. **c**: radial scan of the diffraction pattern with calculated lattice planes for silver, silver chloride, and β-AgI indicated. The diffraction pattern essentially consists of silver diffraction peaks with negligible contributions from silver chloride diffraction spots. The peak marked as 1 can not be explained by either silver or silver chloride but could be assigned to β-AgI.

all the measured and theoretical lattice plane distances for silver and silver chloride are summarized in Table 4.2. The averaged measured distances of the SAED are in good agreement with silver and a negligible amount of silver chloride. Hence, besides the small amount of silver chloride that remains in solution after adding sodium chloride, most of the particles consist of silver. Interestingly, the pattern reveals a distance of 3.9 Å that cannot be explained by either silver or silver chloride. In the plot in Fig. 4.18 **c** this distance is attributed to the $10\bar{1}0$ planes of β-AgI (marked in green). From the low intensity of the peak, one can conclude a very low amount of AgI compared to the dominating peaks for silver.

Table 4.2: Mean value for the measured distances and the most prominent lattice plane distances for silver chloride and silver. The fitting ones are marked in bold font.

measured mean value		Silver Chloride		Silver	
Peak number	d_{hkl} [Å]	hkl	d_{hkl} [Å]	hkl	d_{hkl} [Å]
1	**3.90**				
		111	1.13		
		200	2.70		
2	**2.44**				
3	**2.33**			**111**	**2.33**
4	**2.00**			**200**	**2.04**
		222	1.92		
		311	1.64		
		222	1.58		
5	**1.45**			**220**	**1.45**
		400	1.37		
		313	1.25		
6	**1.24**	**420**	**1.22**	**311**	**1.24**
7	**1.18**			**222**	**1.18**

4.1.11 Discussion

Although this chapter only discusses the nucleation and growth of inorganic silver compounds within the tubular J-aggregate of C8S3, without giving insight into the defined structures, the findings require additional discussion. The crystalline structure of the nanowires is described in the next chapter.

The growth of the wires was previously assumed to be due to a photo-initiated redox reaction with the dyes [1]. Considering the amount of material needed to completely fill an aggregate with crystalline silver, the dyes cannot be the sole source of electrons since many more silver atoms per unit wire length are needed than there are dyes per same length ($N_{dye} : N_{Ag} \approx 1 : 20$ see Appendix). Hence, the dyes cannot provide all the electrons needed to reduce enough silver to completely fill an aggregate. It was suggested that methanol could act as an additional reducing agent for the silver ions. Silver can be reduced by primary alcohols, but this occurs under conditions in which the alcohols form radicals [112][113]. Since these conditions do not occur in our system, it is doubtful that methanol is responsible for the final silver ion reduction. The concentration of silver ions is generally one order of magnitude higher than the dye concentration([dye]=0.34 mM and [Ag]=2.73 mM) and sufficient to fill several tubes. Thus, the resulting structures are more likely to be a mixture of elementary silver and silver compounds like silver oxides or silver halides containing silver ions.

Additionally, the main oxidation of the dyes takes place within the first

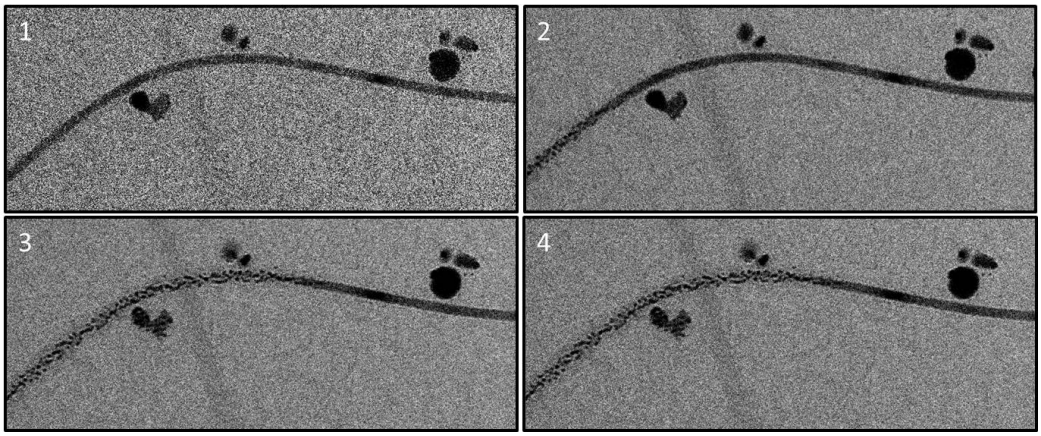

Figure 4.19: Cryo-TEM images of a wire three minutes after illumination showing the dissolution of the wire under the electron beam. The images have been taken subsequently one after another in the order indicated by the numbers without additional electron exposure. It took approximately four minutes to take the series of images.

two hours (Fig. 4.1) but the growth of wires takes days. The initial nuclei formation is most likely due to a redox reaction of silver ions and dyes since nucleation preferentially occurs at the tube walls with a strong oxidization of the template within the first two hours. Another indicator against the straight forward growth of pure silver wires is the instability of the structures under the electron beam. Even the cryo-TEM technique can easily dissolve the wires as shown in Fig. 4.19. Elementary silver is very stable under the electron beam and even silver particles smaller than ten nanometers in diameter require heating up to at least 500 °C to be dissolved in TEM [114]. In contrast, silver compounds, such as silver halides, are very unstable in the TEM. Silver iodide, for example, decomposes rapidly under the electron beam [107].

Regardless of whether the nanowires are pure silver or silver compounds, a model for the growth can be discussed. This model requires little modification after the structure determination of the wires. The principle scheme of the growth process of the nanowires at or within the tubular aggregates is sketched in Fig. 4.20. The early growth phase starts after addition of the silver nitrate and the first TEM or cryo-TEM images are taken a few minutes after illumination (upper branch in Fig. 4.20) or after keeping the sample in the dark (lower branch of Fig. 4.20). The actual formation of nuclei is too fast to be observed ex-situ with TEM. At the earliest time step we find small crystallites, which are randomly distributed in solution, or within the aggregates in form of very short pieces of wires, or attached to the outside of the aggregates in form of globular crystals (see also Fig. 4.3). It is an important observation that the wire-like pieces, together with globular particles only appear when the sample was exposed to blue light (420 nm) for one minute. Otherwise, only the silver nanocrystals on the outside of the

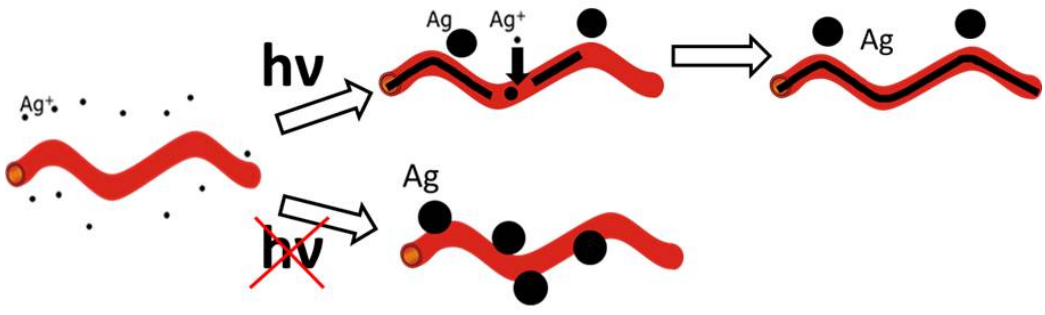

Figure 4.20: Schematic to illustrate the growth of either silver nanowires within the tubular aggregates after exposure to blue light, or silver nanoparticles on the nanotubes without light exposure.

aggregates are found. The influence of light on the growth was already reported [1]. Previously the growth of wires was initiated by white light, but in later investigations it was found that blue light at 420 nm is sufficient to initiate the growth of silver within the aggregates. One should note that the absorbance of the dye aggregates is minimal (see Fig. 4.1) at this wavelength. It is therefore likely that the growth is induced by the absorbance of small crystallites themselves than due to excitation of the dyes.

The formation of nuclei is expected to depend on the concentration of silver ions because of the higher probability for nuclei formation at higher concentrations. The negative SO_3groups of the dyes give the aggregates a negative surface charge. This should cause the silver cations to accumulate at the inner and outer walls of the aggregate tubes. That can explain why silver crystals are almost exclusively formed either at the outer surface or in the inner space of the tubular aggregates. It is important to bear in mind that the solution contains sodium counter ions from the dye salt, and that the concentration of these counter ions is orders of magnitude higher inside the tubes than outside (see Appendix for detailed calculation). Either these counter-ions are mostly exchanged against silver ions, leading to a high silver concentration as well, or the high sodium ion concentration prevents ion exchange and the silver ion concentration is lower inside than outside the aggregates. In the first case, nucleation should occur preferentially inside of the aggregates and the light exposure just facilitates the nuclei formation. In the second case, the probability for nucleation in the dark would be too low to produce a notable amount of nuclei but would be significantly increased by light exposure. In any case, we propose that the non-equilibrium ion concentration between the inner and outer space of the tubular aggregates is responsible for the light-dependent growth of crystallites and hence nanowires.

Regardless of what drives the heterogeneous nucleation, it results in an irregular distribution of crystals in the central cavity. The growth of the crystallites starts from these nuclei to form pieces of wires, as sketched in the middle section of Fig. 4.20. This growth must be supported by material transport trough the membrane-like wall of the dye tubes. Since the wires grow in segments along the tube and these gaps are filled without tube destruction, it is clear that silver atoms must be transported through the wall of the aggregates. However, besides the silver going inside, the water and other counter-ions must go outside, which requires wall permeability for all these materials. Further evidence for wall permeability comes from the observation that any given tube has either internal wires or external nanocrystal decoration, but not a mixture of the two (see cases ii and iii in Fig. 4.7; the additional scarcity of larger crystallites at all types of aggregates is not con-

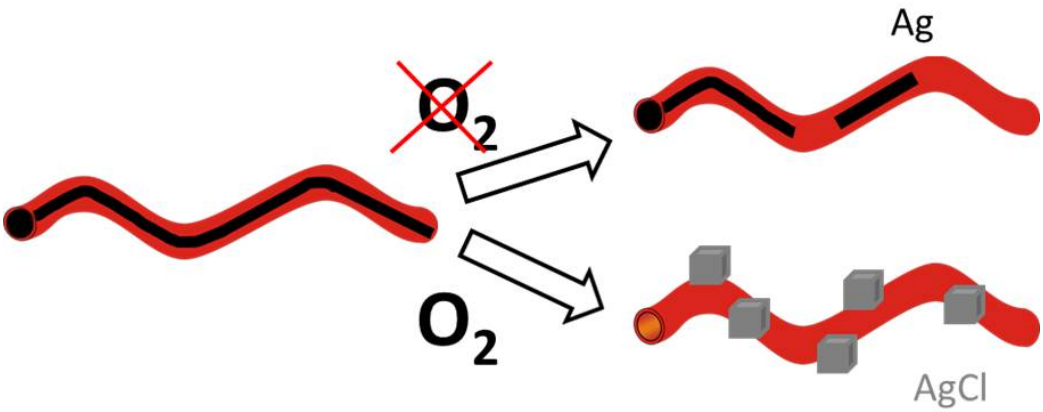

Figure 4.21: Schematic illustrating the dissolution of silver nanowires by oxidative etching using sodium chloride.

sidered further, because these crystallites appear homogeneously like a kind of "background" which cannot be controlled). It shows that either wires grow at the cost of silver ions accumulated on the outside of the aggregates (case ii) or many small particles grow on cost of silver ions present in the tube interior (case iii). This competitive growth requires unhindered ion exchange across the membrane.

The proposed material transport through the membrane is further supported by the observed dissolution of the wires by oxidative etching, as briefly outlined in Fig. 4.21. Wires are no longer found after addition of sodium chloride if oxygen is present in the solution. Instead, the tubular aggregates were found to be empty and decorated with silver chloride crystallites. The wires are effectively dissolved by oxidative etching with the help of chloride serving as a ligand. This supports the idea of material transport through the wall for chlorine and silver ions, since the silver has to be oxidized within the inner space and brought to the outside where it forms the silver chloride crystals (Fig. 4.21).

4.2 Crystal structure analysis of wires

In the previous chapter the growth of wires within the inner space of tubular J-aggregates was described. A model has been presented in which the growth of the wires takes place via material transport through the lipid-bilayer like wall of the template without destroying its morphology. This model could be verified further by manipulating the already stable wires upon addition of sodium chloride. In presence of oxygen the resulting wires were dissolved while the template stayed intact via oxidative etching. The control experiment in the absence of oxygen demonstrated the suggested process. The investigations focused on the morphology of the crystals and the template without giving insight into the actual crystal structure. This is the topic of the following chapter. For the analysis of the crystal structure selected area diffraction (SAED) and high-resolution TEM (HR-TEM) were performed on the resulting crystallites. It is shown that the wires consist of silver iodide. The counter ions of the dye molecules are identified as a likely source for the iodide ions. Detailed investigations of the wire crystals reveal a mutual orientation between the wire and the template. The published results previously presented can be brought into agreement with the identification of the nanowires as silver iodide, and a more complete proposal for the growth process is presented. Since the change of the wires during the growth phase only affects their length, meaning the diameter and crystal structure remain intact, the parameter of growth time is not discussed further in this chapter. However, all experiments have been performed taking precautions to not analyze “over-grown” structures, which can be easily identified by the larger and inhomogeneous diameter of the wires.

4.2.1 High-resolution transmission electron microscopy of a particle

The electron diffraction of the crystal structure of the particles revealed a lattice plane distance of 3.9 Å. This cannot be explained by a silver or silver chloride crystal, as shown in Table 4.2. A better understanding of the origin of this lattice plane spacing can be obtained by using HR-TEM in parallel to SAED. It is challenging to perform multiple TEM methods without dissolution of the structures by the electron beam. This was achieved by placing the sample in a cryo-holder which cools the sample down with liquid nitrogen during the measurement. These measurements allow for direct crystal imaging and give insight into the puzzling distance of 3.9 Å measured for the particles in Fig. 4.18. The samples were prepared with illumination after the addition of silver nitrate so that the combined HR-TEM SAED could also be used for the analysis of the nanowires. Additionally sodium chloride was added to the samples after two days of growth time and the sample were immobilized on a TEM-grid six days after the initial illumination. Fig. 4.22 **a** is a HR-TEM image of a particle. The particle has an almost hexagonal shape as indicated by the drawn red hexagon. The structure shown is obviously single crystalline with the visible lattice planes arranged in a sixfold symmetry with the lattice plane distances of 4.1Å. The arrangement and distances of the lattice planes are marked.

Additionally, an SAED pattern of this area was taken and is shown in Fig. 4.22 **b** together with the corresponding radial plot profile in Fig. 4.22 **c**. The SAED is not due to a single crystalline particle as it consists of rings, indicating an overlap of several crystals. The HR-TEM in Fig. 4.22 **a** reveals another particle on the top left of the image, meaning that the SAED is from several crystals in the region. Nevertheless, the distances determined by SAED are in good agreement with the measured distances from HR-TEM. The combined measurement gives a lattice plane distance of 4.0 ± 0.1Å. This distance cannot be explained by the simple silver or silver chloride lattice. Therefore, one approach is to look for silver compounds that crystallize in a hexagonal lattice and reproduce the measured lattice plane distances in the SAED. Hexagonal silver iodide fulfills all the requirements and can perfectly explain the measured crystallite. Under standard conditions two phases of silver iodide can coexist: the β-silver iodide crystallizes in the wurtzite structure, which is hexagonal closed packed (hcp) and the γ-silver iodide crystallizes in the zincblende structure, a face centered cubic (fcc) crystal [17][115][107]. With HR-TEM the lattice planes could be identified as the $\{10\bar{1}0\}$ planes of hexagonal β-AgI. The SAED pattern shows an overlap of several crystallites which reproduces the lattice plane distances

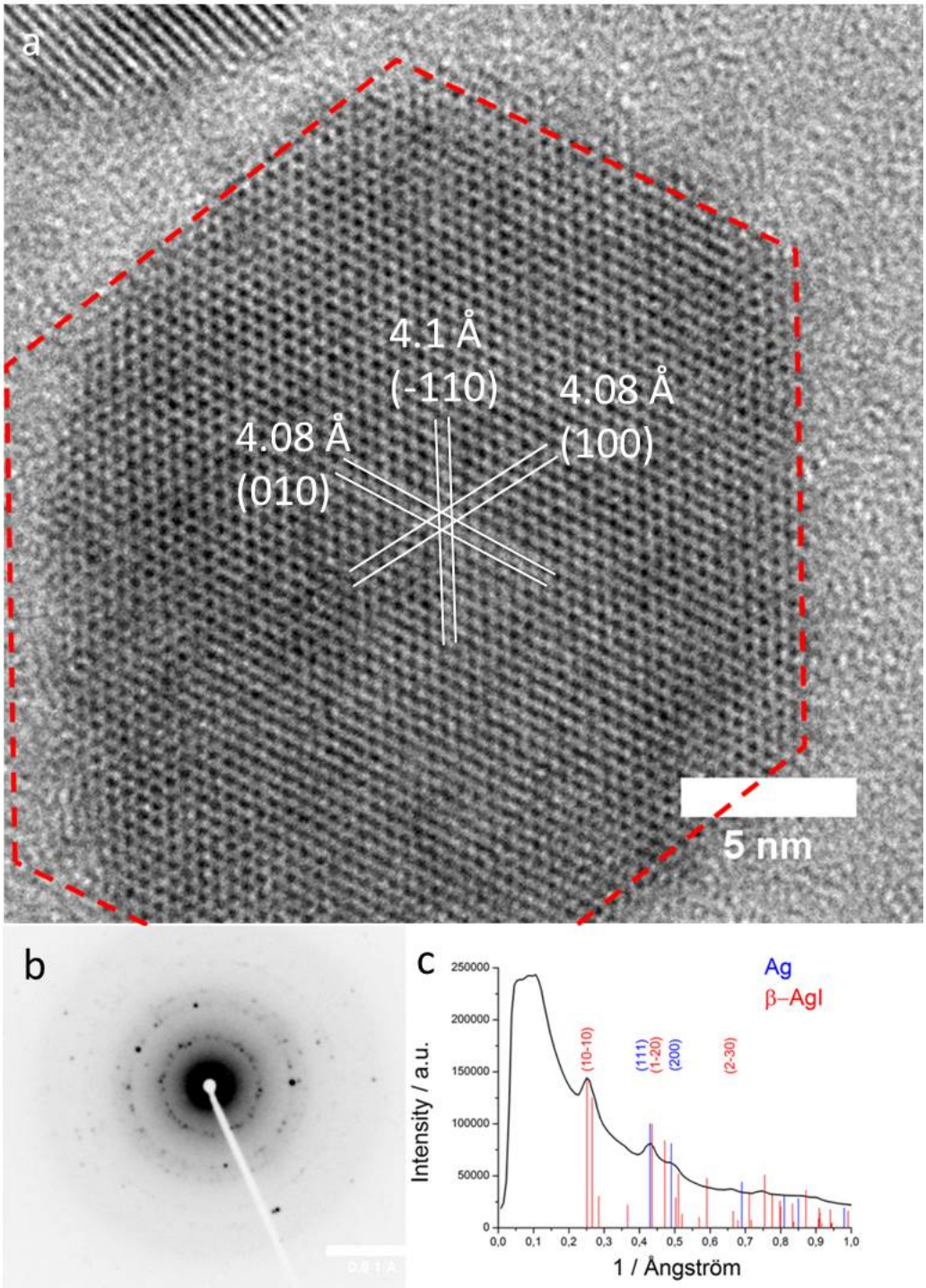

Figure 4.22: **a**: HR-TEM image of a particle. The visible lattice planes have a hexagonal arrangement and the whole particle is almost hexagonal as indicated by the red hexagon. The marked distances are just a visual guide.**b**: SAED pattern of the region shown on top reveals a polycrystalline structure. **c**: radial scan of the SAED with an overlay of calculated silver and β-silver iodide. The analyzed diffraction pattern is a mixture of silver and silver iodide.

for silver iodide and silver as there are also silver particles in the selected area present. In contrast to the analysis performed here, SAED analyses of high density particle areas such as those seen in Fig. 4.18 indicate that silver iodide is present in the particle only sample but is outnumbered by pure silver crystallites. Since no other silver compounds, such as silver oxides, are in agreement with the measured particle, one may conclude that hexagonal silver iodide is also responsible for the measured distance of 4.0 ± 0.1 Å determined from electron diffraction measurements.

4.2.2 Wire analysis

The crystal structure of the nanowires is important for possible applications in nano-optics. The degree of crystallinity is an especially important factor for determining their usefulness. SAED was again used to determine the actual crystal structure of the wires. Energy dispersive X-ray spectroscopy was used to confirm their chemical composition. For a detailed description of the crystals, HR-TEM was combined with SAED. This allowed for an analysis of the crystal orientation relative to the template. The structure of the grown crystal is independent from the growth time. Whenever we obtain a measurable crystal structure it is always the same for the crystallites within the inner space of the template. This means that the following images are independent from the growth time. The crystal structure was also found to be independent of the presence of sodium chloride. The addition of sodium chloride ultimately results in the dissolution of the wires, but the crystal structure of any remaining wires is unchanged.

4.2.3 Selected Area Electron Diffraction

The analysis of the wires has been performed in the same manner as the SAED for the particles. The sample here was prepared with illumination and without addition of sodium chloride. To obtain diffraction patterns from the wires only the smallest available selected area aperture, with a diameter of 200 nm, was used and the grid was searched for positions where only one wire is visible within this selected area. In Fig. 4.23 **a** such a situation is depicted. In the left part a single wire is visible within the selected area. The diffraction pattern obtained from it in Fig. 4.23 **b** shows discrete spots with a certain symmetry. No rings or "clusters" of spots can be seen indicating good crystallinity of the wire. Only few spots (indicated by arrows) are off lattice and obviously belong to differently oriented crystal entities. This indicates that the wire is either one single crystal with an extension over the whole SAED aperture, or at least part of the wire is a

single crystal and the remaining part of the wire consists of crystallites that are too small to give a notable diffraction pattern or is amorphous. However, one can exclude that this wire consists of polycrystalline material where all crystallites are of similar size. The most prominent spots in the pattern are marked in red and blue, respectively. Weak diffraction spots located further away from the center, which belong to smaller distances, are also present. The

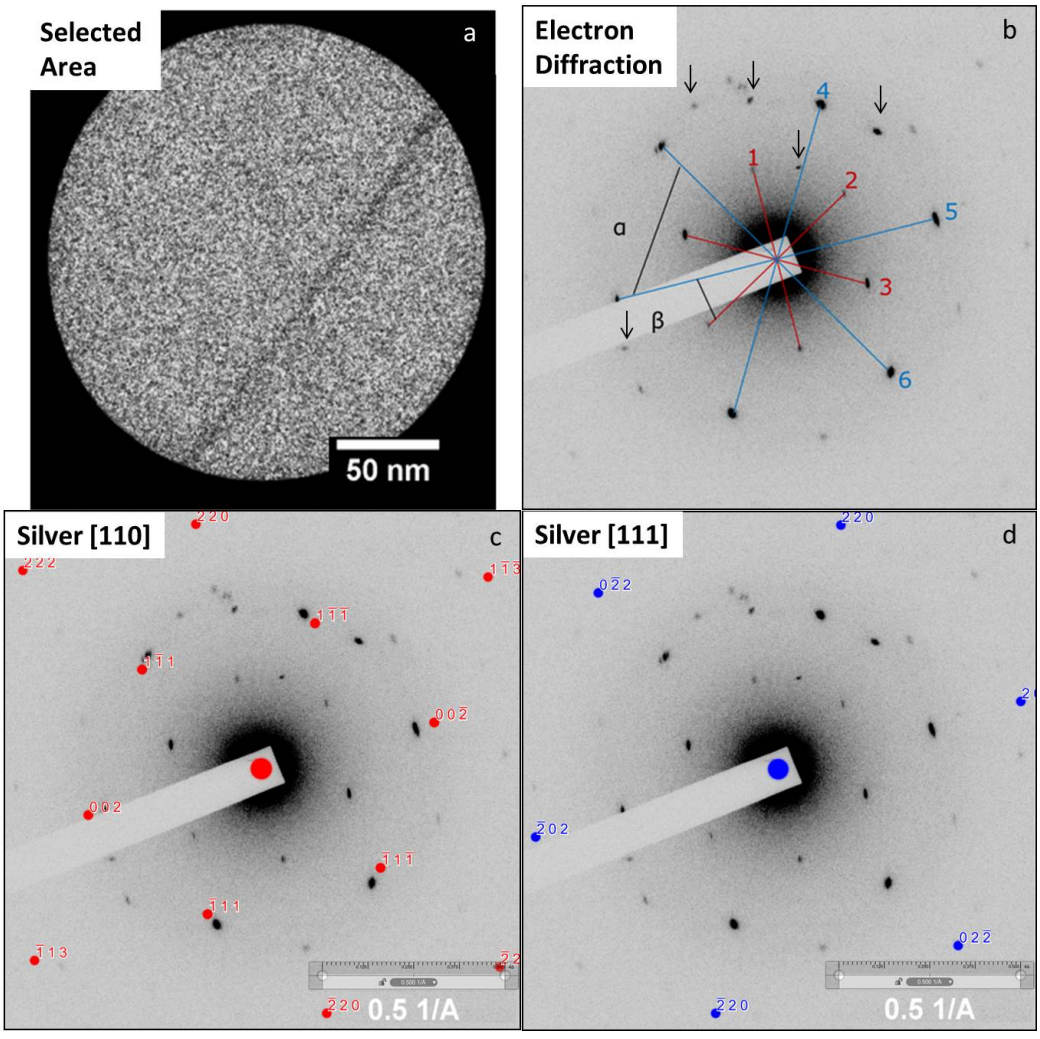

Figure 4.23: **a**: TEM image with a wire in the selected area aperture. The diameter of the aperture is 200 nm. **b**: Electron diffraction pattern from the area in the top left with the spots on the first ring (red), second ring (blue). The angles are marked. The measured values are displayed in Table 4.3. **c**: Overlay of the SAED pattern with simulated diffraction spots for silver fcc in [110] orientation. **d**: Same overlay as in bottom left but with silver in [111] orientation.

outer spots in blue represent a lattice plane distance of 2.30±0.07 Å. The inner ring highlighted in red can be attributed to a lattice plane distance of 3.96±0.07 Å. As already shown for the particles the simple silver fcc lattice cannot be responsible for these obtained distances. The single crystalline appearance of the pattern allows for a detailed investigation.

Table 4.3 shows the values for the measured spots and angles between the spots from the pattern in Fig. 4.23 **b** that belong to one crystal structure. Note that for the deeper analysis of the pattern only the spots with a visible

Table 4.3: Measured spots and angles for the SAED pattern from Fig. 4.23

1 [Å]	3.99
2 [Å]	3.93
3 [Å]	3.93
4 [Å]	2.32
5 [Å]	2.27
6 [Å]	2.31
Error [Å]	0.07
α [°]	60
β [°]	30

Table 4.4: Mean value for the measured distances and the most prominent lattice plane distances for β-silver iodide and silver with the fitting ones are marked in their respective color

measured mean value	**β-Silver Iodide**		**Silver**	
d_{hkl} [Å]	hkl	d_{hkl} [Å]	hkl	d_{hkl} [Å]
3.96	110	3.98		
	200	3.76		
	111	3.51		
	102	2.73		
2.30	210	2.29	111	2.33
	103	2.12		
			200	2.04
	220	1.99		
			220	1.44
			311	1.24

counterpart are marked. The spots belonging to 4.0 ± 0.1 Å consist of 6 distinctive spots with an angle of 60° between them and have a hexagonal symmetry. The outer spots of 2.30±0.07 Å are also in a six-folded symmetry with an angle of 30° between the inner spots. The whole diffraction pattern represents the symmetry of a hexagonal crystal for the given orientation of the wire. The only orientation in which a fcc crystal would project a 6-fold symmetry (which is actually a 3-fold symmetry) is the [111] crystallographic orientation along one of the edges. Fig. 4.23 **c** is an overlay of the pattern with simulated spots for silver in the [111] and in Fig. 4.23 **d** for [110] orientation.

To compare the distances for the most reasonable spots of silver and silver iodide, Table 4.4 shows the measured mean values and some lattice plane distances for both structures. The most prominent lattice plane distances are color coded. Silver in the [111] orientation (red) only shows the {220} planes arranged as a hexagon within the range taken by the SAED. The distance between these planes is 1.44 Å, which is unreasonably small since the calculated spots would lay far outside of even the outer spots of the actual crystal. The [110] orientation gives rise to spots also belonging to {111} with the apparent distance of 2.33 Å. This is close to the measured 2.30±0.07 Å, but in a cubic arrangement. This decent match led to the erroneous assignment of the grown wires to pure silver in previous publications [1][2]. Also, the {200} planes are visible with a distance of 2.04 Å. The silver fcc lattice however, cannot explain the outer spots in the experimentally found pattern or the

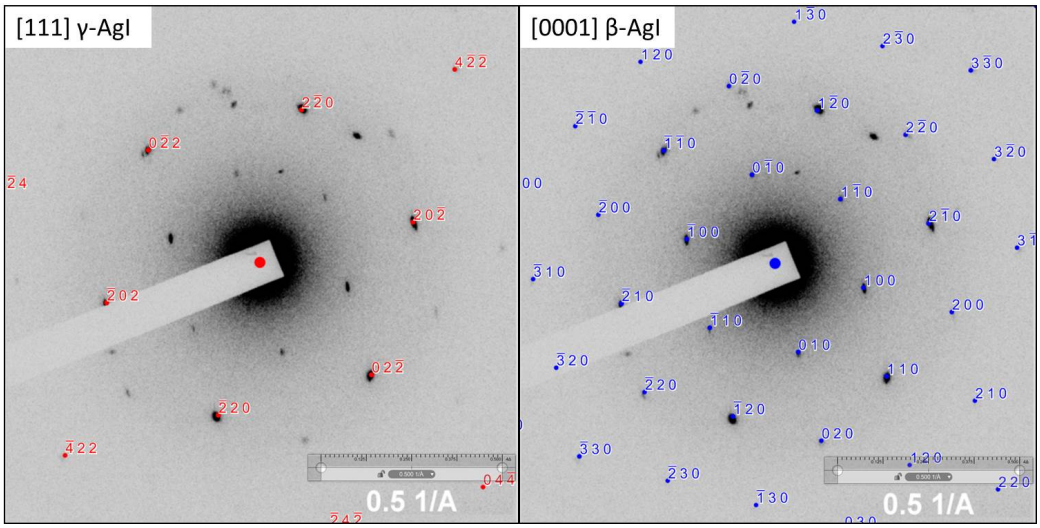

Figure 4.24: same diffraction pattern as in Fig. 4.23 with overlays of calculated silver iodide patterns. **left**: overlay with cubic γ-AgI in [111] orientation. **right**: Overlay with hexagonal β-AgI in [0001] orientation.

inner spots belonging to a distance of 4.0 ± 0.1 Å. Examination of multiple diffraction patterns allows us to conclude that the actual wire crystal has the hexagonal structure of silver iodide orientated along [0001].

After the assignment of the distance of 4.0 ± 0.1 Å to hexagonal silver iodide, one can now explain the SAED pattern of the wires using silver iodide. Two phases of silver iodide can coexist under standard conditions: the β-silver iodide crystallizes in the wurtzite structure which is hcp and the γ-silver iodide crystallizes in the zincblende structure a fcc crystal [17][115][107]. Fig. 4.24 shows the same diffraction pattern as in Fig. 4.23 with an overlay of calculated silver iodide spots. The simulated pattern in Fig. 4.24 **left** is γ-silver iodide in [111] orientation and Fig. 4.24 **right**is β-silver iodide in [0001] orientation. Both result in a hexagonal pattern. The measured pattern can be perfectly explained by the calculated β-silver iodide structure. Especially the 6 inner spots can now be attributed to the $\{10\bar{1}0\}$ planes of hexagonal silver iodide. Every reflex can now be attributed to a certain silver iodide lattice plane distance. Since we have possible coexistence of the two silver iodide phases, the γ-silver iodide must also be investigated. Indeed, the 6 brightest spots could also be assigned to the $\{220\}$ lattice planes of the γ-silver iodide because they have the same lattice planes distances as the β-silver iodide $\{11\bar{2}0\}$ planes. Since the γ-phase cannot explain the additional spots, one can already conclude that the resulting crystals within the template are hexagonal β-silver iodide. Note that in contrast to the particle HR-TEM investigation no additional ions were added to that sample.

4.2.4 Chemical analysis of the wires

SAED measurements for the wires and particles as well as HR-TEM for a particle revealed crystallites that can be explained by hexagonal silver iodide. Since we only added silver nitrate and sodium chloride to the samples, the presence of iodine has to be verified. EDXS measurements allow for an analysis of the chemical composition of the crystals and were performed on the samples. Fig. 4.25 **top** shows a STEM image with the corresponding EDXS mappings for silver and iodine for an illuminated sample after two days of growth. The STEM image of the sample reveals wire like structures and spherical particles. The wires can be identified in both EDXS mappings, of silver and of iodine, while the particles appear in silver mappings only. Spectra have been taken from a "particle-rich" and a "wire-rich" area and are shown in Fig. 4.25 **bottom**. The spectra have been normalized so that the carbon (C) and silicon (Si) peaks, which are both artifacts, have a similar intensity in both measurements. The copper (Cu) peak is an artifact from the underlying substrate and depends on the thickness of the sample. Thus, the

copper peak is higher in the particle area. The signal strength for silver (Ag) and iodine (I) has a similar intensity for the region containing wires, whereas the dominating peak in the particle region is silver. Additional elements besides those shown in the spectra do not exhibit a peak in the EDXS spectra. These indicate that the wires consist mostly of silver and iodine while the particles consist mainly of pure silver. Since no additional halides were added to the solution, the source of the iodine is expected to be found in the dye powder. The dyes are commercially available and were delivered as a salt powder with sodium counter ions. This powder was sent to the Laboratoire National de Sante (LNS) in Luxembourg and measured there with inductively coupled plasma mass spectrometry. The iodine concentration within the salt is 76 mg/g, which results in a stoichiometric ratio of dye:iodine≈2:1 (see Appendix for data sheet and calculations). All these experiments confirm the presence of a significant amount of iodide ions.

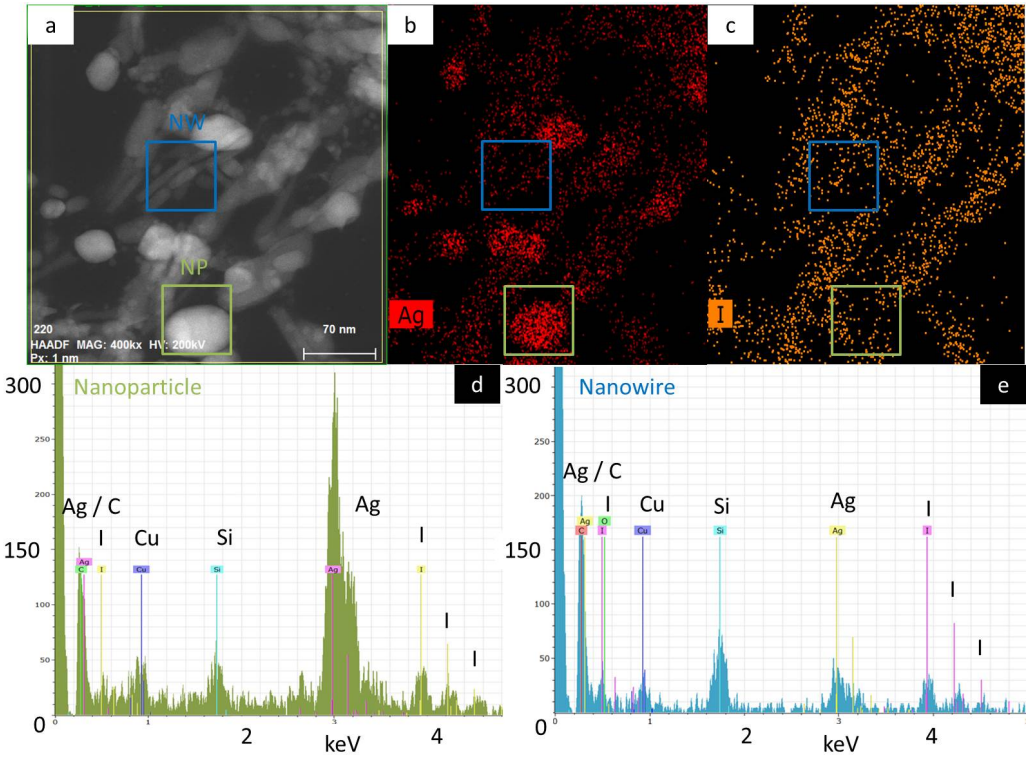

Figure 4.25: Energy dispersive X-ray spectroscopy (EDXS) analysis. a) STEM image of a small part of the sample showing wire-like structures as well as particles. EDXS- mapping for b) silver and c) iodine of the area shown in a). Spectra taken from the marked areas in a) selecting a 'particle-rich' area (d) and a 'wire-rich' area (e). See text for explanation.

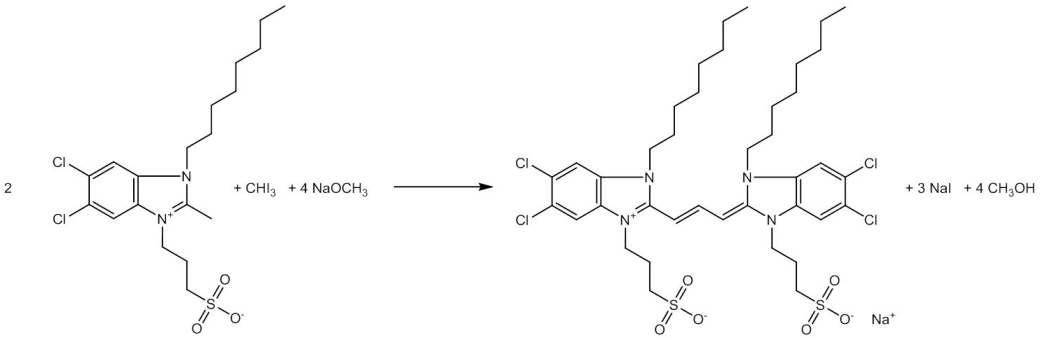

Figure 4.26: Schematic of the last step in the synthesis of the C8S3. Two $1-alkyl-3-(\omega-carboxyalkyl)-5,6-dichloro-2-methylbenzimidazolium$ bromides are brought together with iodoform in presence of sodium methoxide.

The supplier of the dye powder FEW Chemicals has been contacted about this issue to clarify the source of the iodide. The final dye was synthesized by bringing two equivalents of the $1-alkyl-3-(\omega-carboxyalkyl)-5,6-dichloro-2-methylbenzimidazolium$ bromides into the respective benzimidacarbocyanine dyes by treatment with iodoform (CHI_3) in the presence of sodium methoxide as shown in Fig. 4.26. A detailed description of the synthesis of a whole class of these dyes can be found in [116]. The final step in the production is to process the substance to get rid of the remaining contamination. Apparently, this process cannot be done with full efficiency and an unavoidable contamination remains. Nevertheless, the actual concentration of iodide could be reduced from three ions per final dye molecule to a bit more than one ion per two dye molecules. The iodide exists in the form of sodium iodide, so, besides sodium and iodide, we can expect no other ions to be present within the dye salt.

4.2.5 High-resolution transmission electron microscopy of wires

After we could verify the presence of β-silver iodide within the samples and determining the origin of the iodide ions, we still lacked deeper insight into the actual wire structure. The size of the crystalline domains as well as a possible influence of the template on the crystal orientation is of interest here. The combined measurement of HR-TEM with SAED was also applied for the wires. For the following images the crystals were again stabilized by addition of sodium chloride after two days of growth time and grids were prepared six days after illumination. Each grid was then placed in a cryo-holder cooling the sample down with liquid nitrogen during the measurement. Fig. 4.27 **a**

shows a HR-TEM image of a wire with the corresponding SAED pattern in Fig. 4.27 **b**, collected in the same way as for the particles shown in Fig. 4.22. The crystalline part of the grid is marked by a red and blue line revealing the homogeneity of the diameter of the wire.

The wire in the HR-TEM actually reveals two crystalline domains as shown in Fig. 4.27 **a**. The domains are marked and indexed in the enlarged images of the figure. The red part of the wire is hexagonal and can be explained by β-silver iodide. The smaller blue domain shows a stacking of planes with a distance of 2.37 Å. Such HR-TEM measurements supported the misinterpretation of the wires as silver [1]. The evaluation of the SAED in Fig. 4.27 **b** allows for more detailed investigation. In Fig. 4.27 **c** the SAED pattern is overlain by the simulated β-silver iodide spots in [0001] orientation. The right part shows the radial plot profile of the pattern with the theoretical distances of silver, β-silver iodide, and γ-silver iodide. The hexagonal domain of the wire marked in red in the HR-TEM is maintained over the whole wire, as can be seen in the SAED, revealing the good crystallinity. The blue domain is visible as a broadening in the SAED for the spots belonging to a distance of 2.32 Å, marked with a red spot in both images. Those lattice planes can either be assigned to the $\{11\bar{2}0\}$ lattice planes of β-silver iodide, the $\{200\}$ planes of γ-silver iodide, or the $\{200\}$ planes of silver. Before we make use of both of these measurements to fully explain the presented structure, we first clarify the correlation of the two methods. Fig. 4.28 is a schematic showing the same images as in Fig. 4.27 but with line scans in the HR-TEM picture and their respective plot profiles. The line scans are averaged over several lines and reveal the good crystal orientation of the wire. Every visible lattice plane distance in HR-TEM can be assigned to one specific pair of spots in the SAED as marked in the image by the same colors as for the line scans. With this correlation it is now possible to completely characterize the crystal structure and orientation of this particular wire.

Besides the β-silver iodide crystal responsible for most of the image, we also have a stacking of lattice planes in the blue part. This stacking is most likely due to β-silver iodide as well, but in a different orientation. The crystal is the same as in the hexagonal domain but titled by a certain angle relative to the beam. Fig. 4.29 is a simulation of β-silver iodide with the calculated electron diffraction pattern for the structures performed with CrystalMaker. In Fig. 4.29 **top** the crystal structure for the hcp silver iodide is displayed. The silver atoms are gray and the iodine are purple. The left part shows β-silver iodide in the [0001] view direction resulting in an hexagonal arrangement of the atoms. Visible here are the $\{10\bar{1}0\}$ planes. The left part is β-silver iodide in almost the same orientation but rotated by 5° clockwise around the red axis shown in the left part. Here only one lattice plane ar-

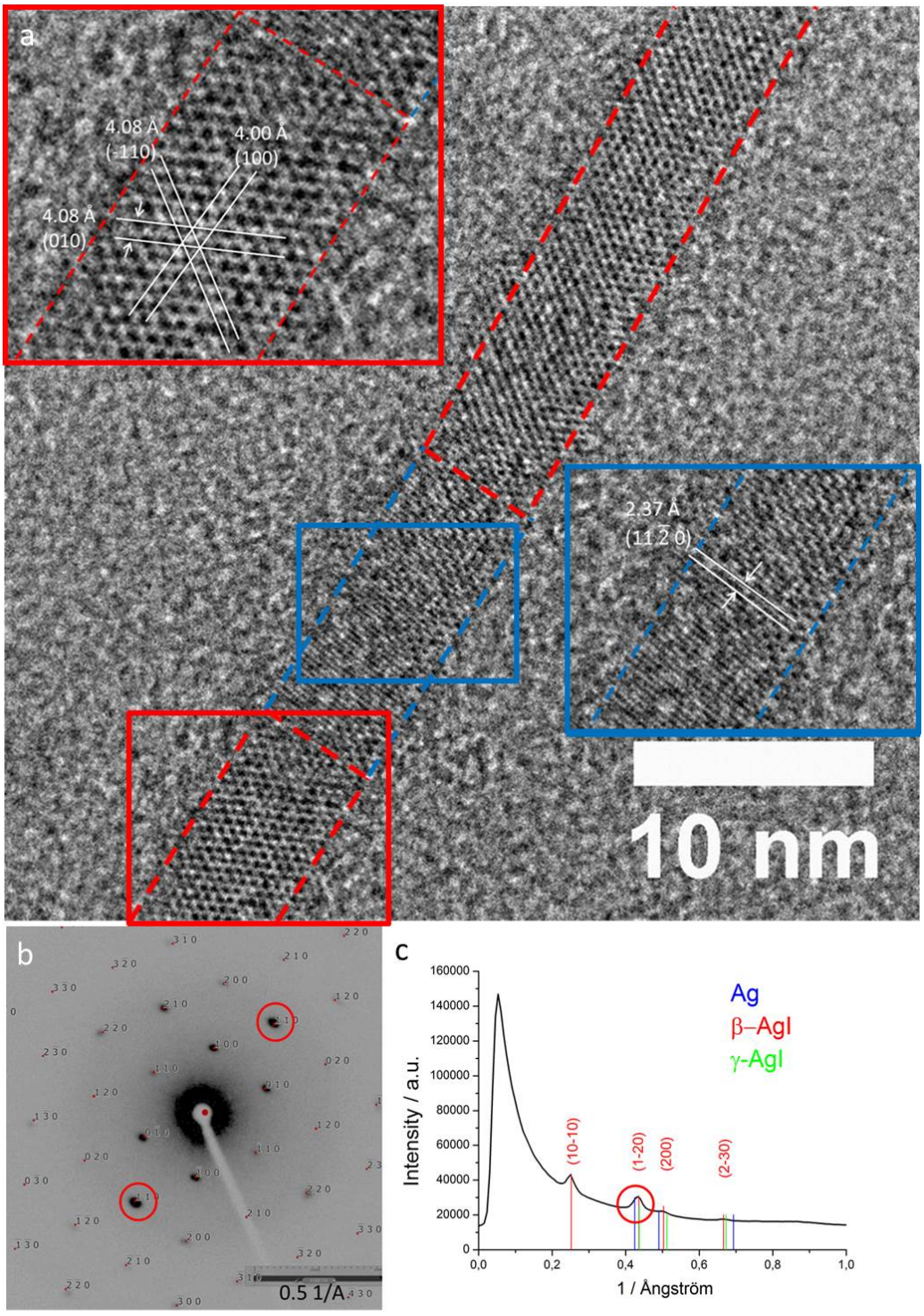

Figure 4.27: **a**: HR-TEM of a wire. The image reveals two crystalline domains. The blue domain is β-AgI in [0001] orientation with the $\{10\bar{1}0\}$ planes marked and indexed. The red domain is a stacking of planes resulting in a distance of 2.37Å. **b**: SAED of the wire shown in the top with an overlay of a calculated β-AgI pattern in [0001] orientation. **c**: radial plot of the SAED with calculated spots for the silver, β-AgI, and γ-AgI. Only β-AgI is in agreement with all the measured distances, whereas silver and γ-AgI could be attributed to the structure in the red domain of the top image marked here with red circles.

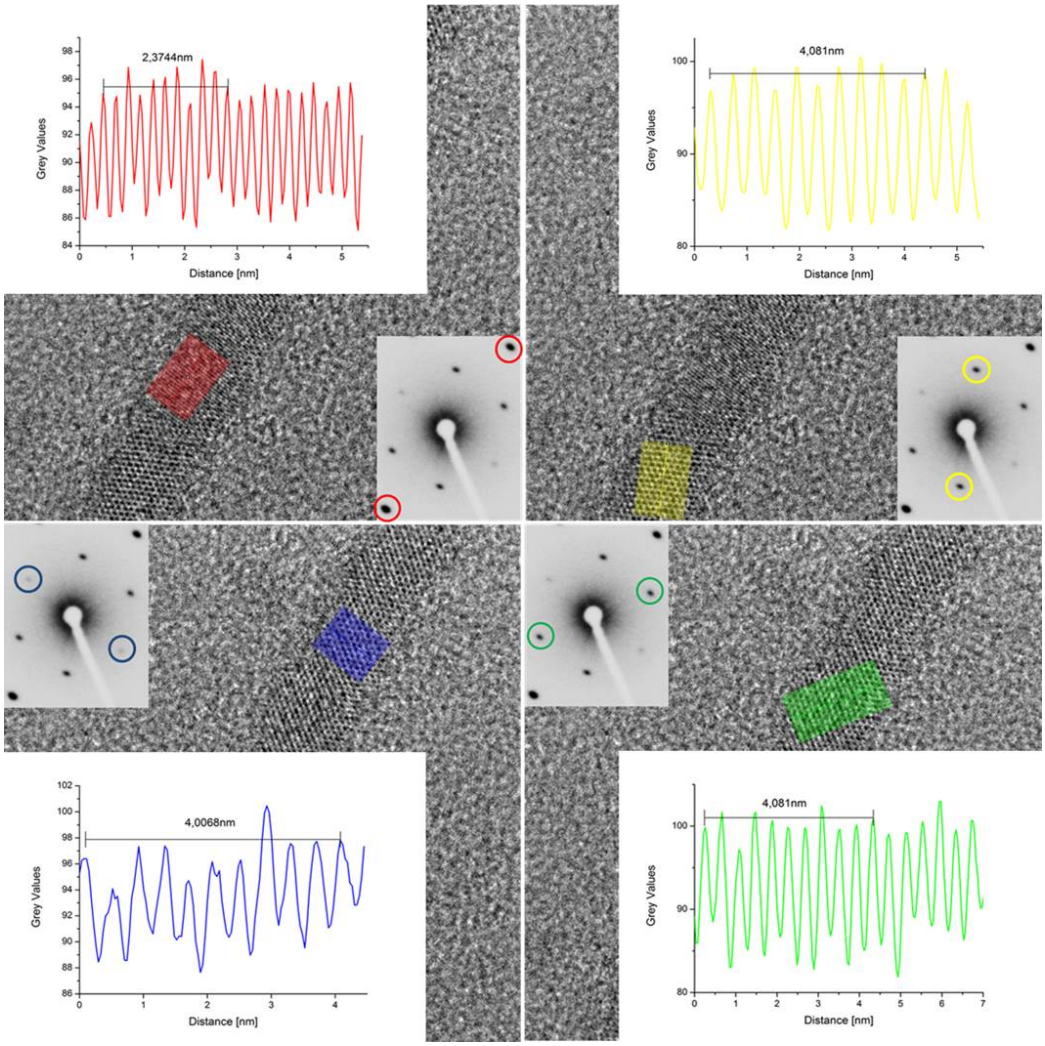

Figure 4.28: HR-TEM image and SAED as in Fig. 4.27 with line scans for all visible lattice plane distances in HR-TEM. The most prominent spots in the SAED can now be assigned to visible lattice plane distances in HR-TEM as marked with colors.

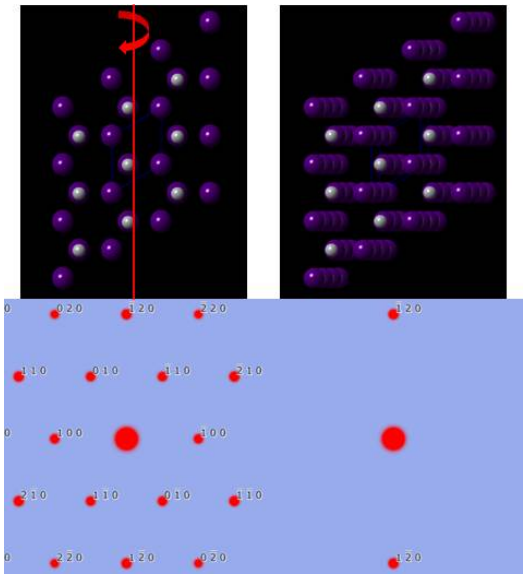

Figure 4.29: Models of β-AgI crystals and respective calculated electron diffraction patterns. Silver is displayed in gray and iodine in purple. The structure on the right hand side is rotated by 5° clockwise around the red axis to generate the one on the left.

rangement is visible, namely the horizontal stacking of one of the $\{11\bar{2}0\}$ planes. Fig. 4.29 **bottom** shows the simulated electron diffration patterns for the orientations displayed in the upper part of this image. For the crystal in perfect orientation, the left electron diffraction pattern contains all possible spots. The rotation by 5° in the right part results in the loss of almost all spots except for the one $\{11\bar{2}0\}$ plane perfectly perpendicular to the tilt axis. The Ewald sphere construction gives a simple geometric interpretation of this effect as introduced in the fundamentals section.

With the help of these simulations we can now give the exact orientations of the two crystal in the HR-TEM image. Fig. 4.30 shows an enlarged image of the lower junction of Fig. 4.27 with a model of the β-AgI crystal structures and an implied relation between them on the right. The HRTEM image has been simulated with QSTEM [102], shown on the left of Fig. 4.30, using the same orientations as for the model of the β-AgI crystal. The simulation reproduces very well the observed structures within the HRTEM image. Note that the model structure and the HR image are not in the same scale and the lines drawn between those two just indicate the correlation. The lower red part, is hcp [0001] of silver iodide with the $\{10\bar{1}0\}$ planes visible as a hexagon perpendicular to the view direction. This is shown for the lower simulated crystal structure. The simulated crystal for the upper, blue part

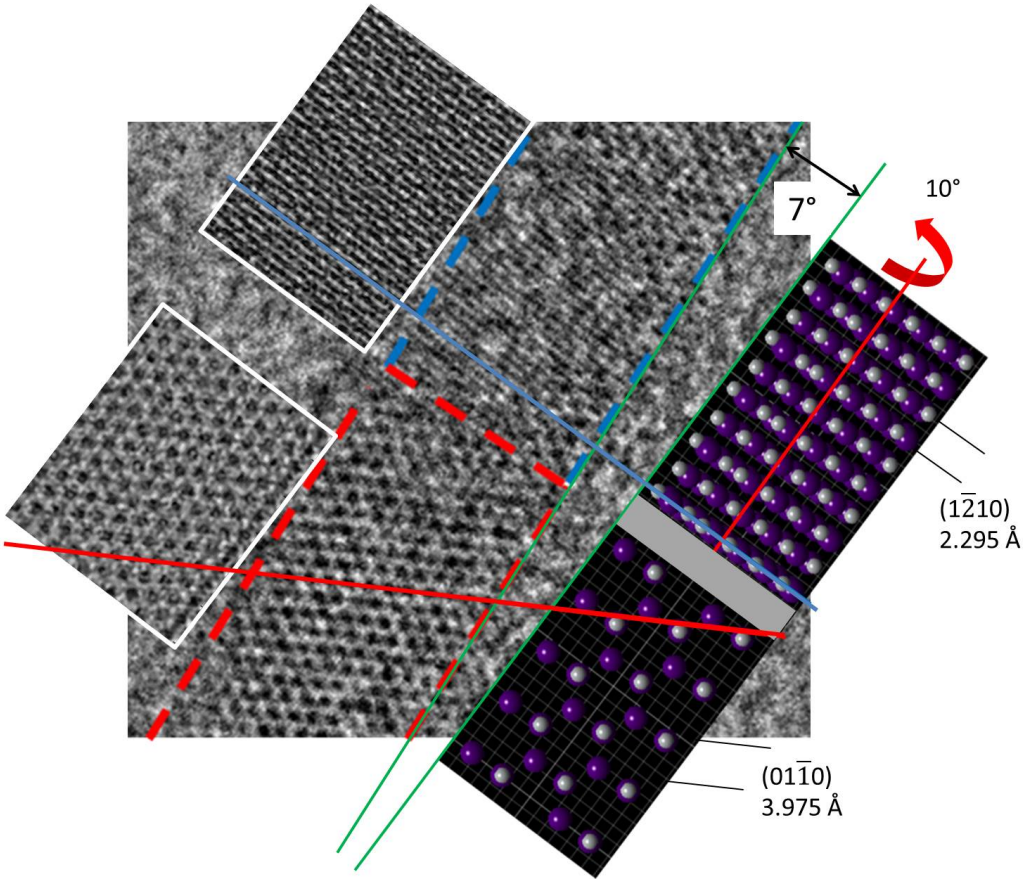

Figure 4.30: Magnified view of the HRTEM image of the single AgI nanowire shown in Fig. 4.27. A model of a β-AgI crystal is shown at the right (not in scale) and simulated HRTEM images for these two respective orientations are shown at the left. The lower part is viewed along the [0001] direction and the typical hexagonal lattice becomes apparent. The upper part is rotated along the [1$\bar{2}$10] axis by an angle of 10° which causes the appearance of lattice planes seen edge-on. The model is oriented such that the lattice planes have the same orientation as in the HRTEM image, indicated by the red and blue line. The [1$\bar{2}$10] axis then turns out to be tilted by 7° with respect to the main aggregate axis.

is also hexagonal silver iodide but rotated along the [1$\bar{2}$10] axis as described above. The rotation shown here is 10°, resulting in the stacking of one of the {11$\bar{2}$0} planes as visible in the HR-TEM. The result is a tilt of the whole crystal of 7±1° relative to the aggregates axis as shown in the figure by the red and blues lines connecting the image with the simulation. The error in the angle measurement is due to the fact that the aggregates axis cannot be perfectly defined in the pictures as the wire appears a little fringed. As

a result, we can now explain the wire crystal structure by β-silver iodide and even get insight into the relative orientations between crystals and their template.

4.2.6 Crystalline domains of the wires

After clarification of the crystal structure we can use the data obtained by HR-TEM to gain further insight into the crystal orientation. Of particular interest is the relative orientation of the crystal lattice relative to the templates axis. This orientation can either be totally random or fixed. Fig. 4.31 shows two different HR-TEM measurements where the visible lattice planes are marked and indexed according to β-silver iodide and the angle relative to the templates axis is marked. The left part in Fig. 4.31 is the stacking of one of the $\{10\bar{1}0\}$ planes as the crystal is again tilted as already explained for the junction in Fig. 4.30. The planes have an angle of 96±1° degree relative to the aggregates axis. The right part of Fig. 4.31 is the straight forward β-silver iodide in [0001] orientation. There the interesting angle is 97±1°. HR-TEM also provides us with crystals tilted so, that the lattice planes closest to being perpendicular to the template axis is tilted away from the electron beam. Such situations are depicted in Fig. 4.32. From the stacking of the planes in the images we can identify the corresponding lattice planes, which are in both cases the $\{10\bar{1}0\}$ planes. From these planes the others are tilted by an angle of 60°. These not visible planes are marked in

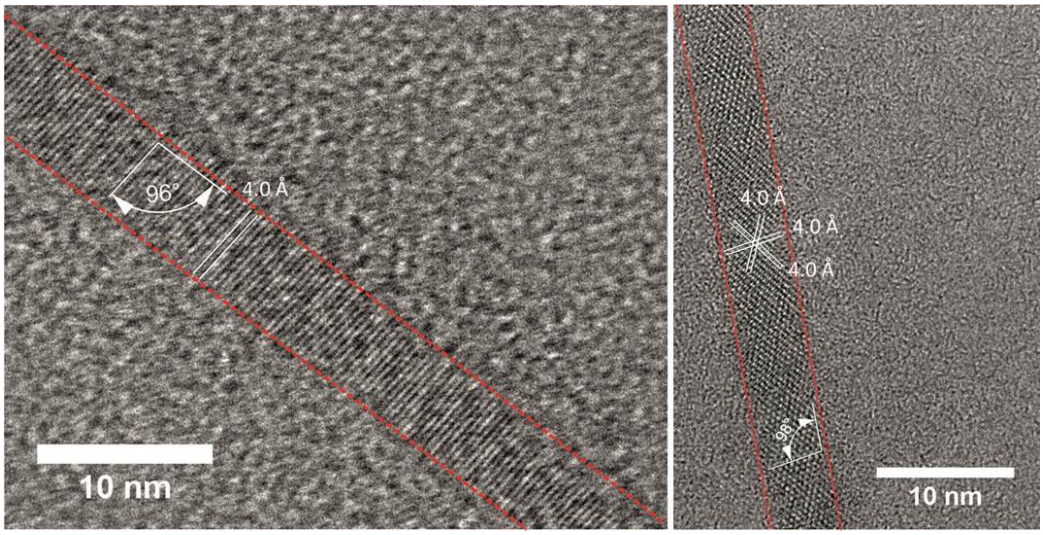

Figure 4.31: HR-TEM of two wires with their orientation relative to the aggregates axis.

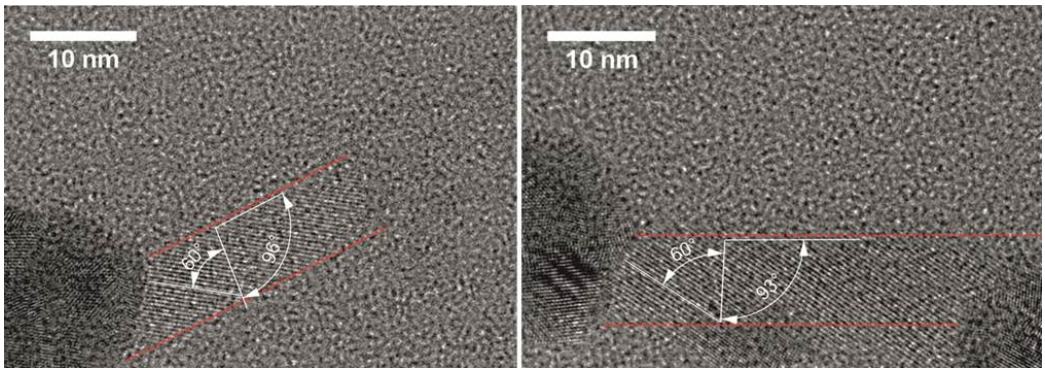

Figure 4.32: HR-TEM of two wires where one of the $\{10\bar{1}0\}$ plane almost perpendicular to the template axis is tilted away. This axis exhibit an 60° angle between the visible planes as shown by the angle dimensioning originating from the visible lattice planes. From there the orientation between those planes and the aggregate axis is marked.

white with their respective angles to the template. For these two images the angles are 96±2° and 93±2°. As a result, we can say that, for the analyzed crystals the angle between one of the $\{10\bar{1}0\}$ planes and the aggregate axis is 96±2°. This is a remarkable correlation between the grown crystals and the template with a defined derivation from the perfectly perpendicular arrangement of the $\{10\bar{1}0\}$ planes and the aggregates axis of 6±2°. It is another interesting observation that for the last two wires, which do not exceed over the image range displayed here, the crystalline domain starts from a particle.

Most of the crystalline domains of the wires shown here are bigger than the image sizes displayed. This allows us to conclude that they can reach a length of more than 40 nm. Fig. 4.33 is a combination of three HR-TEM images from the same wire. It shows a single crystalline wire with extension of more than 120 nm, which appears to be uniformly bent over the whole range. The bending is emphasized by the lines that follow the direction of one given lattice plane. For comparison, the orientation of the lattice plane at the far left of the image is reproduced as a dashed red line at the other positions. The crystal exhibits a twin boundary along the central part, as emphasized by the dashed white line in Fig. 4.33. The AgI wire is connected at the left end with a spherical particle.

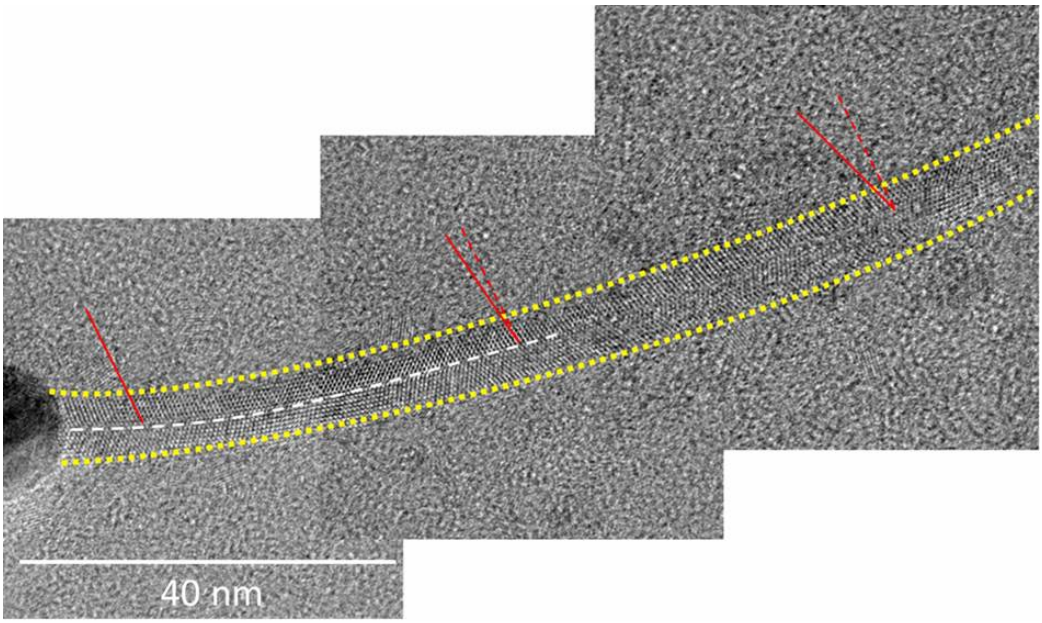

Figure 4.33: HRTEM image of largely extended AgI nanowire. The image was obtained by adding three separate HRTEM images taken by moving the object within the TEM. A twin boundary can be seen along the central part of the wire (white dashed line). At the left a silver nanoparticle is visible. The crystal is bend over the whole range. The red lines indicate the orientation of one given lattice plane. The dashed red lines always point towards the direction of the line at the very left.

4.2.7 Discussion

The equilibrium shape of every crystal is a result of minimizing its total surface free energy and the low energy faces are preferentially expressed [71]. The favored growth direction of β-AgI is along the z-direction or [0001], i.e. the stacking direction of the hexagons. One can attribute this to the minimum surface energy of the basal plane of the close packed hexagonal crystal. It was demonstrated for epitaxial growth that this orientation of silver iodide is independent of the substrate orientation [115][117]. So we would expect the silver iodide to grow with basal planes perpendicular to aggregate axis with the characteristic AB-stacking of these planes visible parallel to the templates axis as sketched in Fig. 4.34 top branch.

Surprisingly, we found exactly the basal plane orientated almost parallel to the template's axis (Fig. 4.34 lower branch). The orientation of the crystals and the template reveal a mutual orientation between the two, where one of the $\{10\bar{1}0\}$ planes always cover an angle of $96\pm2°$ with the aggregate's axis. A possible explanation can be that the aggregate, described as a wrapping of dye molecules along a cylinder with a certain angle, is responsible for

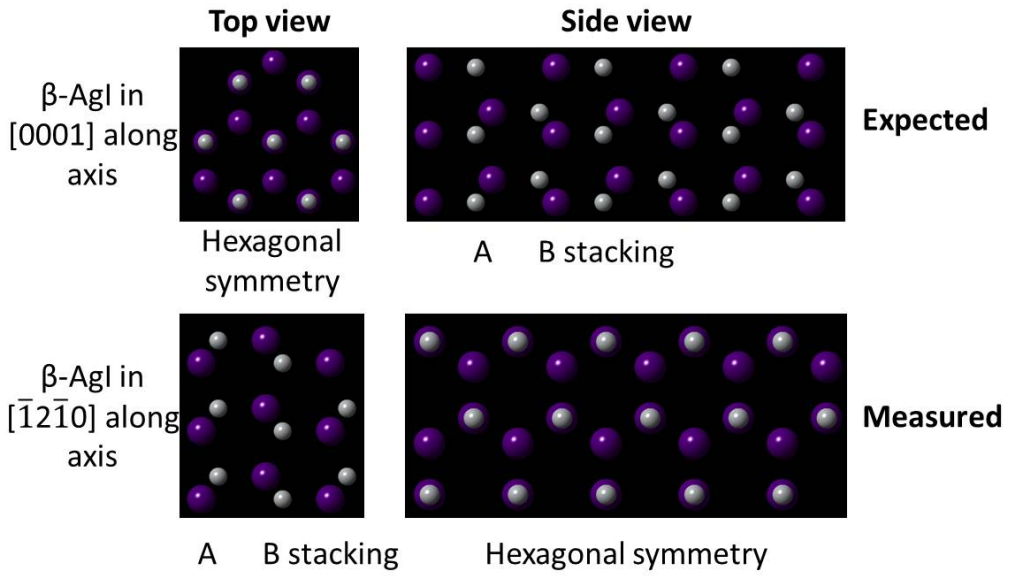

Figure 4.34: Sketch of two possible AgI orientations relative to the aggregates axis. The top branch shows the growth of the basal plane parallel to the templates axis resulting in the characteristic AB-stacking for hcp systems as expected. The lower branch shows the actual orientation as measured with the basal plane visible perpendicular to the axis.

that defined angle. Unfortunately, the actual structure of the J-aggregates from the C8S3 is still a subject under discussion. From the so far developed theoretical structure models [62][118] no reasonable parameter for the stacking of the dyes could explain the mutual orientation that was found. An experimental approach for structure determination is even more challenging and only revealed the pitch angle for the outer dye layer of 17° [119]. It could be shown that when coating the C8S3 aggregates with a silica shell on the outer layer, the silica adopts a helical structure reflecting the J-aggregate's outer layer superstructure [120]. Under the assumption that the wire growth starts from the inner surface of the aggregate, one may suppose that the crystal structure of the silver iodide is correlated with the superstructure of the inner dye layer.

Taking diffraction patterns from single nanowires was a very challenging task. Most of the isolated wires identified by TEM did not produce a diffraction pattern. Those wires that produced a SAED pattern always revealed spots belonging to the distance of the $\{10\bar{1}0\}$ planes (see Appendix for more SAED patterns). For a β-AgI crystal only the [0001] orientation and slight rotations from this orientation would produce a diffraction pattern with spots belonging to this distance. We never obtained a SAED pattern for silver iodide in a different orientation along other axes, which would be expected for randomly orientated crystals. Upon drying and immobilizing the sample on the TEM-grid no direction is preferred and the structures should be arbitrarily orientated. Additionally, HR-TEM shows the same tendency and reveals only slight rotations from the [0001] orientation but almost always one of the $\{10\bar{1}0\}$ planes visible. Only the intensively studied structure in Fig. 4.27 reveals a stronger rotation leading to the $\{11\bar{2}0\}$ planes becoming visible.

A possible explanation is the mutual orientation between the crystal structure and the tube's axis. A rotation of the tube would lead to a rotation of the crystal along an axis that is tilted by 6° with respect to the $\{10\bar{1}0\}$ planes. This rotation of the crystal along an axis different from one of the axes defined by the unit cell would not orient the crystal to one of its main crystallographic orientations. All other orientations do not generate a diffraction pattern, but a set of two points in the diffraction as seen for the rotated structure in Fig. 4.27. Thus, only the [0001] orientation generates an evaluable pattern in this system. That would explain, why it was so difficult to obtain diffraction patterns from the wires only.

The identification of the crystal structure as silver iodide requires a reinterpretation of the previously proposed growth model. Especially the role of the illumination, which is necessary for the wire growth, must be reevaluated. Now, with all the results presented above, one can at least suggest a better model for the initial nucleation process and the necessity of illumination.

The proposal for the growth process is sketched in Fig. 4.35.

First, we assume that the iodine anions are either close to the positive charges of the cyanine dyes, which is delocalized along their conjugated backbone, or dissolved as free ions in solution. The freely dissolved I^- cations may easily precipitate with added Ag^+ cations and thus do not play any role for the growth of the nanowires. The tubular aggregates are made of a double layer of the amphiphilic dyes with the negatively charged sulfopropyl side groups pointing to the outer or inner space of the tube [37]. From this model one can assume that the I^- cations are located somewhere within the inner part of the tube wall, attracted by the positive charge of the polymethine group and at reasonable distance to the SO_3^- groups. The concentration of ions can be orders of magnitude higher inside the tube than outside (see Appendix).

Second, the $AgNO_3$ is added to the solution with preformed tubular aggregates in ten fold excess with respect to the dye. The Ag^+ cations are attracted electrostatically by the aggregates and either they attach to the outer surface or they diffuse through the wall into the interior of the tube. If the silver cations remain at the outer surface they can be reduced by oxidization of the dye molecules and form bare silver particles [65]. That is observed by TEM, where growth of particles is only observed at the outside of the aggregates but never in the interior [2][121]. Additionally, the oxidation of the dyes is seen by optical absorption spectroscopy and it shows up at a time where no wires in the aggregate and only few particles at the outside

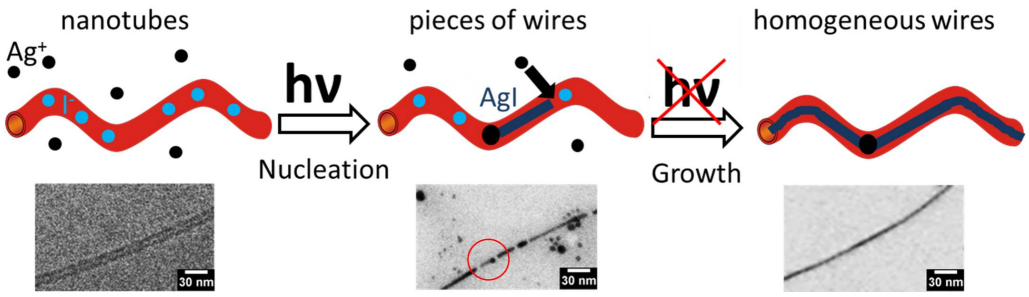

Figure 4.35: Schematic to illustrate the growth of silver iodide wires within a tubular J-aggregate. The added silver ions accumulate close to the aggregates, were some ions have already diffuse inside the tube. The iodide ions are mainly inside the tube and the illumination creates elementary silver and iodide. These silver nuclei are stable and act as seeds for the subsequent growth of silver iodide wires. Additional silver ions diffuse through the confining walls of the template and nucleate with the iodide ions at the pre-existing existing structures. Those fragments eventually coalesce to a homogenous wire.

are visible [121].

It is obvious that silver cations diffuse through the tubular wall in order to provide the material supply. On the path through the aggregate wall and within the interior of the aggregate the silver ions are the minority in comparison to iodine anions but may form complexes of the kind AgI, AgI_2^-, AgI_3^{2-} and higher [122][123]. These complexes then may condensate to larger AgI crystals. At the concentrations given, these complexes are supposed to be unstable and do not reach the critical size of a nucleus to grow into a crystal. However, illumination with 420 nm hits the band gap of the AgI complexes and crates neutral Ag atoms and silver clusters, as is well known from the photographic reaction [124]. Silver clusters now can be stable when formed only from a few atoms [125]. Hence we assume that AgI clusters combined with these silver clusters serve as seeds for the growth of AgI crystals. The formation of the seeds is assumed to take place close to the inner wall of the aggregates.

The stable silver iodide nuclei are evenly distributed along the aggregate, leading to the piecewise wires typical for the early growth phase as in Fig. 4.4. The growth then continues on the stable nuclei. Additional silver ions diffuse through the wall of the template and crystallize with the iodide ions inside the tube, as can be seen in Fig. 4.27 for two differently orientated fragments. If growth starts from two seeds simultaneously at different places of the wall, a grain boundary or even twin boundary as seen in Fig. 4.33 may be formed. Those fragments eventually coalesce to a homogeneous wire.

Oxidative etching upon addition of sodium chloride is apparently dependent on the presence of oxygen. It is expected that the small silver seeds are etched by this process, but it remains puzzling that the grown silver iodide is dissolved as well. The growth of silver chloride decorating the outer wall of the tube could be due to Ostwald ripening at the expense of silver iodide. The surface to volume ratio is much better for the silver chloride particles than for the high-aspect ratio silver iodide nanowire.

Chapter 5

Conclusion and outlook

5.1 Conclusions

The assignment of the crystalline nanowires to silver iodide is certainly the most important outcome of this work. Since only silver ions were added to the solutions and the particles consist of pure silver, it was reasonable that in previous publications the wire structure had been attributed to pure silver [1][2]. The presence of iodide ions within the solution was, to the best of our knowledge, not self-explanatory. Additionally supporting this misconception was the fact that the lattice plane distance of the $\{11\bar{2}0\}$ silver iodide planes is almost the same as that of the $\{111\}$ planes of silver. Together with HR-TEM showing rotated silver iodide crystals resulting in the $\{11\bar{2}0\}$ planes being visible, this could easily lead to the wrong assignment of pure silver. Nevertheless, the here presented results allow for the following conclusions.

TEM imaging of the growth process of silver iodide nanowires within the tubular J-aggregates of the surfactant dye allowed for identification of the starting points of the nanocrystalline wire growth. These locations indicate where nucleation occurred, a process which cannot be directly visualized. It was found that nucleation within the aggregates is induced by light while nucleation outside the aggregates also occurs in the dark. The nuclei inside the aggregates are located at relatively large, but rather regular, distances and grow piecewise into wires until they fill the entire aggregate. The growth does not affect the shape and morphology of the template tubular structure, which means that the latter acts as a real template. This direct templating process is only possible because the aggregates are permeable for ions and water molecules, but are stable enough not to be deformed by the growing crystals. This direct templating process is different from other soft templates where facet capping leads to anisotropic growth.

The material transport through the confining wall of the tubular aggregates permits also precipitation of excess silver ions and dissolution of the nanowires by oxidative etching. These properties allow further control of the growth of silver iodide nanowires within the tubular template structure.

Structure analysis of the wire crystals allows for correction of the erroneous assignment to pure silver for the wires in previous publications. The source of the iodide ions could be identified as impurities within the dye powder itself. Based on these findings the role of the illumination could be determined to induce silver seed formation from accumulations of silver and iodide within the inner space of the template. The combination of these seeds and the inner dye-layer of the template provide enough interfaces for the formation of stable silver iodide wires.

The tubular J-aggregate induces a preferential orientation to the crystal structure of the wires. Since this orientation is considered unfavorable in terms of surface energy, it is assumed to follow the structure of the inner dye-layer of the double-walled template and to be induced by the nucleation at the silver seed layer formed at the surface of the dye aggregate.

5.2 Outlook

The role of the iodide in the growth of the nanowires needs to be further clarified. Upon addition of iodide ions in a controlled manner the growth of the wires could be strongly affected. First experiments, where iodide was added before the addition of silver nitrate, only resulted in a stronger bundling of the tubes without the formation of wires. Addition in presence of silver nitrate led to formation of silver iodide particles and preservation of the wires in their actual state. Use of different halides, like the chlorides presented here, have a similar outcome. Adding the halides before silver nitrate results in bundling of the tubes without wire formation, whereas addition after silver nitrate dissolves the wires. Since the addition of halides into a dye solution does not lead to the formation of nanowires, use of different counter ions for the dye salt could result in different silver halide nanowires. This requires a synthesis of the dyes with the use of another halide than iodide or a recrystallization of the existing dye salt.

On the other hand, the chloride ions led to the formation of silver chloride crystallites decorating the J-aggregate. Use of other halide ions should result in a similar outcome, covering the aggregate with different silver halides. All this might pave the way for the synthesis of new inorganic organic hybrid systems.

For future applications of these wires the important ability of ionic superconductivity for silver iodide needs to be investigated. The transformation of silver iodide from the β-phase to the interesting α-phase happens under elevated temperatures of at least 150° C for bulk silver iodide under normal conditions. Coating of silver iodide nanoparticles with poly(vinyl pyrrolidone) (PVP) stabilizes the α-phase down to 30° C [126]. Since the silver iodide nanowires are coated with a dye aggregate, it is possible that the α-phase shows similar behavior in our system.

Chapter 6

Appendix

6.1 Calculation of silver and iodine to dye molecule ratio

For the growth of silver wires inside the tubular J-aggregates the silver ions have to be reduced to neutral silver. It is interesting to estimate how many silver atoms per nm length are needed to grow a compact silver structure because this gives insight to the mechanism of silver transport and electron delivery.

We estimate the number of dye molecules per length of the tubular aggregate from the volume of the aggregate structure and the density of crystalline dye material. The latter is taken from x-ray diffraction data of the very similar dye C8O3 [127].

Mass density of J-aggregates is reported to be $\rho = 1.29\frac{g}{cm^3}$; from the volume of the unit cell a volume per dye is calculated to be $V_d = 1.12nm^3$.

The volume of the J-aggregate per nm length is

$$V_j = (r_a^2 - r_i^2) * \pi = 99.5nm^3$$

(with: $r_a = \frac{1}{2} * 13nm$ and $r_i = \frac{1}{2} * 6.5nm$).

From these numbers we calculate the number of C8S3 molecules per nm length:

$$N_d = \frac{V_j}{V_d} \approx 89.$$

The volume taken by a silver atom can be calculated from the regular fcc structure to be $V_{Ag} = 0.017nm^3$.

The size of the silver wire is given by the hollow space within the J-aggregate per nm length:

$$V_H = r_i^2 * \pi = 33.2nm^3.$$

Hence we obtain the number of silver atoms within the nanowire per nm length:

$$N_{Ag} = \frac{V_H}{V_{Ag}} \approx 1953.$$

The ratio of dye molecules per silver atoms is then given by:

$$N_d : N_{Ag} = 89 : 1953 \approx 1 : 20.$$

This number tells that the silver atoms forming the nanowire cannot be provided by exchange of the counterions of the dyes, because they are present only in a 1:1 stoichiometry. Also, they cannot be provided by sacrificial oxidation of dye molecules alone.

With the same approach the number of silver iodine per nm length required to fill the aggregate can be calculated. Volume of the silver iodine base in hcp structure is:

$$V_{AgI} = 0.07nm^3.$$

The number of silver iodide within the nanowire per nm length:

$$N_{AgI} = \frac{V_H}{V_{AgI}} \approx 474.$$

The resulting ratio of dye molecules per silver iodide is:

$$N_d : N_{AgI} = 89 : 474 \approx 1 : 4.$$

Since silver iodide has the empirical formula AgI, the silver to dye ratio and the iodine to dye ratio is:

$$N_d : N_{Ag} = 89 : 237 \approx 1 : 2.$$

$$N_d : N_I = 89 : 237 \approx 1 : 2.$$

To completely fill all the aggregates we need a ratio of dye to iodine of 1:2 (Silver is added in a 10-fold excess with respect to the dyes). Iodine ions are present in a dye:iodine ratio of 2:1. From this we can conclude, that the number of iodine ions in the sample is sufficient to fill every fourth aggregate completely or every aggregate up to one fourth of its length.

6.2 Ion concentration inside and outside the tube

For the comparison of the concentration of ions inside and outside the double-walled tube we first estimate the charge per length from the number of molecules per length by assuming one elementary charge per molecule: $\tau \approx 90\frac{e}{nm}$ (see former section). These charges are distributed between the inner and outer wall and since the packing density of the molecules is identical the charge density must be as well:

$$\sigma_i = \sigma_o.$$

with $\sigma = \frac{q}{A}$, $q = eN$, and $A = 2r\pi h$ follows:

$$\Leftrightarrow 1 = \frac{\sigma_i}{\sigma_o} = \frac{q_i 2r_o\pi h}{2r_i\pi h q_o}$$

$$\Leftrightarrow \frac{q_i}{q_o} = \frac{r_i}{r_o}$$

by defining $q = eN = q_i + q_o$:

$$\Leftrightarrow \frac{q - q_o}{q_o} = \frac{r_i}{r_o}$$

$$\Leftrightarrow \frac{q}{q_o} = 1 + \frac{r_i}{r_o}$$

$$\Leftrightarrow q_o = q\frac{1}{1 + \frac{r_i}{r_o}}$$

Inserting the values leads to the following charges per nm length for the inner and outer wall:

$$q_o = 60\frac{e}{nm} = \tau_a$$

$$q_i = 30\frac{e}{nm} = \tau_i$$

One can easily see, that:

$$\sigma_o = \frac{q_o}{2r_o\pi 1} = 1.47\frac{e}{nm^2} = \sigma_i.$$

Under the assumption that for every dye exists one counter-ion (e.g. Na^+) we can calculate the ion concentration inside the tube:

$$\rho_i = \frac{\tau_i h}{V_i} = \frac{\tau_i h}{Ah} = \frac{30e}{33.2nm^3} \approx 1\frac{e}{nm^3}$$

$$\Leftrightarrow 1\frac{e}{nm^3} = \frac{e}{(10^{-8}dm)^3} = 10^{24}\frac{e}{l}$$

$$\Leftrightarrow \rho_i = \frac{10^{24}}{N_A}\frac{mol}{l} = 1.66\frac{mol}{l}.$$

The concentration of ions outside the tube is simply the overall concentration:

$$\rho_{o,\infty} = 3 * 10^{-4}\frac{mol}{l}$$

and by comparison between ρ_i and ρ_o one can see, that the concentration of counter ions is three to four orders of magnitude higher inside the tubes than outside.

6.3 Iodide concentration within the dye salt

The Laboratoire national de sante (LNS) in Luxembourg has measured the absolute iodine concentration to be 76 mg/g. Of interest here is the stoichiometric ratio between the dyes and iodine. The respective molecular weights for iodine and C8S3 are:

$$M_I = 127\frac{g}{mol}$$

$$M_{C8S3} = 903\frac{g}{mol}$$

Note, that M_{C8S3} is the overall dye powder and already contains one Na-molecule per one dye molecule. The measured value gives the relative percentage of iodine within one gram of analyte:

$$\frac{m_I}{m_{C8S3} + m_I} = \frac{0.076}{1}$$

$$\Leftrightarrow \frac{m_{C8S3}}{m_I} + 1 = \frac{1}{0.076}$$

$$\Leftrightarrow \frac{m_{C8S3}}{m_I} = \frac{1}{0.076} - 1$$

From there follows for the mass ratio of iodine to C8S3:

$$\frac{m_I}{m_{C8S3}} = \frac{0.076}{1 - 0.076} = 0.0822$$

By using $m = M * [C]$:

$$\frac{m_I}{m_{C8S3}} = \frac{[C]_I M_I}{[C]_{C8S3} M_{C8S3}}$$

$$\Leftrightarrow \frac{m_I}{m_{C8S3}} = \frac{[C]_I}{[C]_{C8S3}} \frac{127}{903}$$

$$\Leftrightarrow \frac{m_I}{m_{C8S3}} = \frac{[C]_I}{[C]_{C8S3}} 0.140 = 0.0822$$

$$\Leftrightarrow \frac{[C]_I}{[C]_{C8S3}} = \frac{0.0822}{0.140} = 0.59$$

This ratio tells us that per dye molecule in the salt we have 0.6 iodide ions or an approximate ratio of $C8S3 : I \approx 2 : 1$.

LNS LUXEMBOURG

Laboratoire national de santé
Département des laboratoires officiels d'analyses de contrôle
Service d'hygiène du milieu et de surveillance biologique

Dudelange, le 11 octobre 2016

Martin Kaergel MSc
Hahn-Meitner-Platz 1
D-14109 Berlin

Notre référence : ***161011-iode***
Votre référence : *Votre mail du 09 octobre 2016*

Concerne : Votre demande d'offre concernant la détermination d'iode dans un colorant

Bonjour,

Veuillez trouver les résultats concernant la détermination d'iode dans un colorant :

Echantillon	**iode**
Dye C8S3	76 mg/g

L'analyse a été effectuée en double. L'ensemble de l'échantillon fût solubilisé dans de l'eau déionisée et analysé par spectroscopie de masse à plasma à couplage inductif (ICP-MS).

Pour de plus amples renseignements et toute question je vous prie de ne pas hésiter de me contacter,

Meilleures salutations,

Dr Georges Dahm

LABORATOIRE NATIONAL DE SANTÉ | HYGIÈNE DU MILIEU ET SURVEILLANCE BIOLOGIQUE | 1, RUE LOUIS RECH - L-3555 DUDELANGE | TÉL. (+352) 28 100-609 | FAX (+352) 28 100-602

Figure 6.1: Data sheet for the measurement of iodide concentration within the C8S3 powder as delivered.

6.4 Simulation of HRTEM images

The HRTEM images were simulated using the QSTEM software package for quantitative STEM and TEM simulations which is based on a multislice algorithm (https://www.physics.hu-berlin.de/en/sem/software/software_qstem). The calculated HRTEM images shown in Fig. 4.30 are explained here in more detail. An almost cubic super cell of β-AgI with a thickness of 6.6 nm was used. This fits well with the typical diameter of 6.5 $\pm$ 0.5 nm of the nanowires. In Fig. 6.2 this super cell is oriented with the [0001] direction normal to the projection plane. A focal series has been calculated and the only agreement between simulation and experiment was found for a defocus of -110 nm. The defocus was determined by knowing that it has to be identical for both areas of the nanowire seen in Fig. 4.30. Only for a defocus of - 110 nm the simulation reproduces the image contrast observed in the experiment. An "amorphous" noise has also been added to account for the contribution of the carbon support film to the image contrast. Fig. 6.3 displays a simulation for the same supercell as in Fig. 6.2 but rotated along the $[1\bar{2}10]$ axis by 10°. Additionally, the electron diffraction patterns for these structures have been calculated and were found in good agreement with the experimentally obtained pattern.

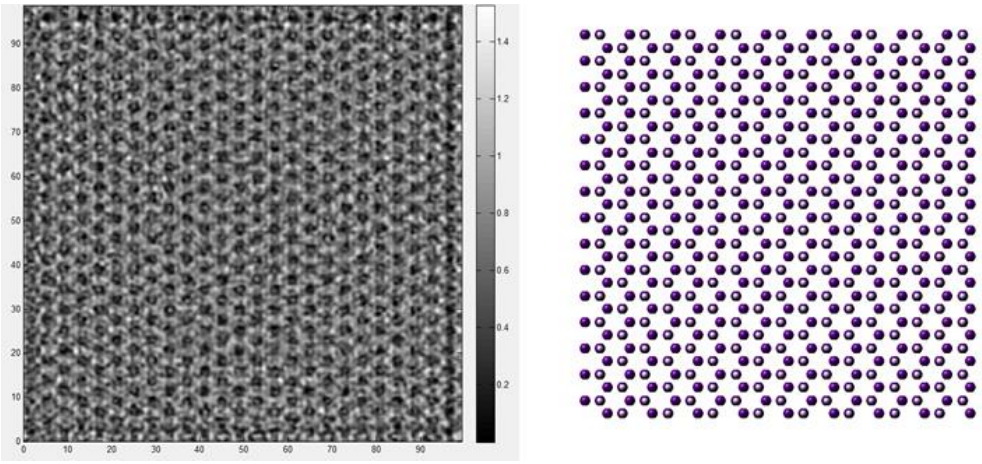

Figure 6.2: Simulation of the HRTEM image (left) for the supercell shown on the right performed with QSTEM. This simulation is shown in Fig. 4.30 in the lower part next to the measured HRTEM. The unit cell for β-AgI in [0001] orientation is shown on the right. The defocus value for the simulation is -110 nm, the thickness 6.6 nm, and an "amorphous" noise has been added to account for the carbon support film.

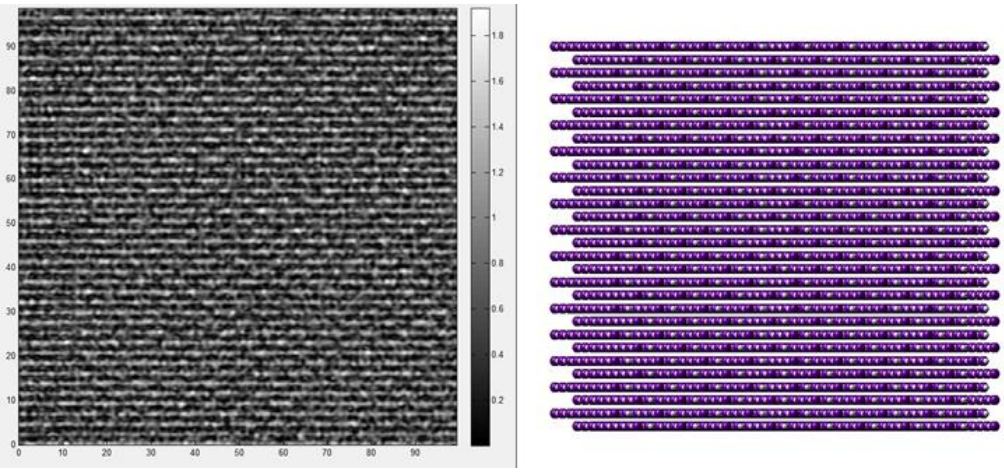

Figure 6.3: a: Simulation of the HRTEM image for the supercell shown on the right performed with QSTEM. This simulation is shown in Fig. 4.30 in the upper part next to the experimentally observed fringe pattern. The unit cell for β-AgI in [0001] orientation is rotated along the $[1\bar{2}10]$ axis by 10°. The defocus value for the simulation is -110 nm, the thickness 6.6 nm, and an "amorphous" noise has been added to account for the carbon support film.

6.5 SAED patterns

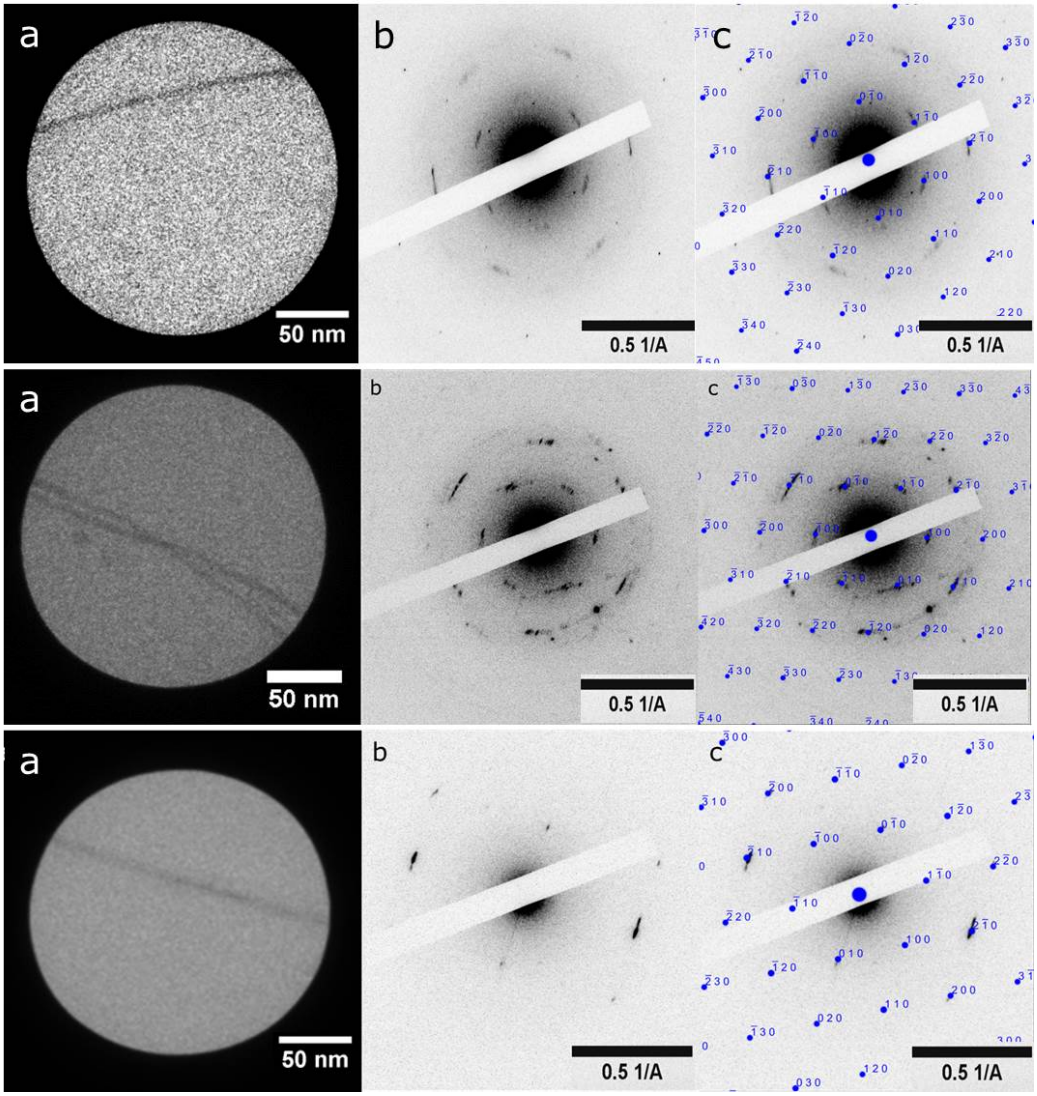

Figure 6.4: SAED analysis of three different samples. a) TEM image of a wire. b) diffraction pattern of the wire shown in a. c) diffraction pattern as in b with overlay of calculated β-AgI in [0001] orientation.

List of Figures

List of Tables

Bibliography

[1] Dorthe M. Eisele, Hans V. Berlepsch, Christoph Bottcher, Keith J. Stevenson, David A. Vanden Bout, Stefan Kirstein, and Juergen P. Rabe. Photoinitiated growth of sub-7 nm silver nanowires within a chemically active organic nanotubular template. *Journal of the American Chemical Society*, 132(7):2104–+, 2010.

[2] Egon Steeg, Frank Polzer, Holm Kirmse, Yan Qiao, Jürgen P. Rabe, and Stefan Kirstein. Nucleation, growth, and dissolution of silver nanostructures formed in nanotubular j-aggregates of amphiphilic cyanine dyes. *Journal of Colloid and Interface Science*, 472:187–194, 2016.

[3] R. D. Zhu, Z. Y. Luo, H. W. Chen, Y. J. Dong, and S. T. Wu. Realizing rec. 2020 color gamut with quantum dot displays. *Optics Express*, 23(18):23680–23693, 2015.

[4] Byoungho Lee, Il-Min Lee, Seyoon Kim, Dong-Ho Oh, and Lambertus Hesselink. Review on subwavelength confinement of light with plasmonics. *Journal of Modern Optics*, 57(16):1479–1497, 2010.

[5] Liangbing Hu, Han Sun Kim, Jung-Yong Lee, Peter Peumans, and Yi Cui. Scalable coating and properties of transparent, flexible, silver nanowire electrodes. *Acs Nano*, 4(5):2955–2963, 2010.

[6] Yunxia Jin, Lu Li, Yuanrong Cheng, Lingqiang Kong, Qibing Pei, and Fei Xiao. Cohesively enhanced conductivity and adhesion of flexible silver nanowire networks by biocompatible polymer sol-gel transition. *Advanced Functional Materials*, 25(10):1581–1587, 2015.

[7] Nasir M. Abbasi, Haojie Yu, Li Wang, Abdin Zain ul, Wael A. Amer, Muhammad Akram, Hamad Khalid, Yongsheng Chen, Muhammad Saleem, Ruoli Sun, and Jie Shan. Preparation of silver nanowires and their application in conducting polymer nanocomposites. *Materials Chemistry and Physics*, 166:1–15, 2015.

[8] J. T. Hu, T. W. Odom, and C. M. Lieber. Chemistry and physics in one dimension: Synthesis and properties of nanowires and nanotubes. *Accounts of Chemical Research*, 32(5):435–445, 1999.

[9] W. P. McConnell, J. P. Novak, L. C. Brousseau, R. R. Fuierer, R. C. Tenent, and D. L. Feldheim. Electronic and optical properties of chemically modified metal nanoparticles and molecularly bridged nanoparticle arrays. *Journal of Physical Chemistry B*, 104(38):8925–8930, 2000.

[10] T. Ida, H. Saeki, H. Hamada, and K. Kimura. The preparation and properties of polycrystals of solid electrolyte ultrafine particles. *Surface Review and Letters*, 3(1):41–44, 1996.

[11] T. Ida and K. Kimura. Ionic conductivity of small-grain polycrystals of silver iodide. *Solid State Ionics*, 107(3-4):313–318, 1998.

[12] Y. G. Guo, J. S. Lee, and J. Maier. Agi nanoplates with mesoscopic superionic conductivity at room temperature. *Advanced Materials*, 17(23):2815–+, 2005.

[13] Y. G. Guo, Y. S. Hu, J. S. Lee, and J. Maier. High-performance rechargeable all-solid-state silver battery based on superionic agi nanoplates. *Electrochemistry Communications*, 8(7):1179–1184, 2006.

[14] D. A. Keen, S. Hull, W. Hayes, and N. J. G. Gardner. Structural evidence for a past-ion transition in the high-pressure rocksalt phase of silver iodide. *Physical Review Letters*, 77(24):4914–4917, 1996.

[15] M. Nagai and T. Nishino. Enhancement in conductivity for porous alumina-based agi-al2o3 composites by use of temperature and concentration gradient. *Solid State Ionics*, 117(3-4):317–321, 1999.

[16] C. Tubandt and E. Lorenz. Molecular state and electrical conductivity of crystallised salts. *Zeitschrift Fur Physikalische Chemie–Stochiometrie Und Verwandtschaftslehre*, 87(5):513–542, 1914.

[17] G. Cochrane and N. H. Fletcher. Ionic conductivity and low frequency dispersion in hexagonal silver iodide. *Journal of Physics and Chemistry of Solids*, 32(11):2557–, 1971.

[18] S. Hull. Superionics: crystal structures and conduction processes. *Reports on Progress in Physics*, 67(7):1233–1314, 2004.

[19] A. P. Alivisatos. Perspectives on the physical chemistry of semiconductor nanocrystals. *Journal of Physical Chemistry*, 100(31):13226–13239, 1996.

[20] G. Markovich, C. P. Collier, S. E. Henrichs, F. Remacle, R. D. Levine, and J. R. Heath. Architectonic quantum dot solids. *Accounts of Chemical Research*, 32(5):415–423, 1999.

[21] Y. Kimura, R. Kikuchi, and T. Kawamoto. Effect of shape of silver-chloride particles on photosensitivity of photochromic-glasses. *Physics and Chemistry of Glasses*, 18(5):96–100, 1977.

[22] S. Xu and Y. D. Li. Different morphology at different reactant molar ratios: synthesis of silver halide low-dimensional nanomaterials in microemulsions. *Journal of Materials Chemistry*, 13(1):163–165, 2003.

[23] C. R. Berry. Structure and optical absorption of agi microcrystals. *Physical Review*, 161(3):848–, 1967.

[24] S. H. Chen, T. Ida, and K. Kimura. Thiol-derivatized agi nanoparticles: Synthesis, characterization, and optical properties. *Journal of Physical Chemistry B*, 102(32):6169–6176, 1998.

[25] K. R. Gopidas, M. Bohorquez, and P. V. Kamat. Photoelectrochemistry in semiconductor particulate systems .16. photophysical and photochemical aspects of coupled semiconductors - charge-transfer processes in colloidal cds-tio2 and cds-agi systems. *Journal of Physical Chemistry*, 94(16):6435–6440, 1990.

[26] T. Tanaka, H. Saijo, and T. Matsubara. Optical-absorption studies of the growth of microcrystals in nascent suspensions .3. absorption-spectra of nascent silver-iodide hydrosols. *Journal of Photographic Science*, 27(2):60–65, 1979.

[27] H. Saijo, M. Iwasaki, T. Tanaka, and T. Matsubara. Electron-microscopic study of the growth of sub-microcrystals in nascent silver-iodide and silver bromoiodide hydrosols. *Photographic Science and Engineering*, 26(2):92–97, 1982.

[28] Y. G. Guo, J. S. Lee, and J. Maier. Preparation and characterization of agi nanoparticles with controlled size, morphology and crystal structure. *Solid State Ionics*, 177(26-32):2467–2471, 2006.

[29] K. H. Schmidt, R. Patel, and D. Meisel. Growth of silver-halides from the molecule to the crystal - a pulse-radiolysis study. *Journal of the American Chemical Society*, 110(15):4882–4884, 1988.

[30] D. Hayes, K. H. Schmidt, and D. Meisel. Growth mechanisms of silver-halide clusters from the molecule to the colloidal particle. *Journal of Physical Chemistry*, 93(16):6100–6109, 1989.

[31] H. Tan and W. Y. Fan. Laser-based synthesis of core ag-shell agi nanoparticles. *Chemical Physics Letters*, 406(4-6):289–293, 2005.

[32] B. Gates, B. Mayers, Y. Y. Wu, Y. G. Sun, B. Cattle, P. D. Yang, and Y. N. Xia. Synthesis and characterization of crystalline ag2se nanowires through a template-engaged reaction at room temperature. *Advanced Functional Materials*, 12(10):679–686, 2002.

[33] H. L. Cao, X. F. Qian, C. Wang, X. D. Ma, J. Yin, and Z. K. Zhu. High symmetric 18-facet polyhedron nanocrystals of cu7s4 with a hollow nanocage. *Journal of the American Chemical Society*, 127(46):16024–16025, 2005.

[34] Y. H. Wang, J. M. Mo, W. L. Cai, L. Z. Yao, and L. D. Zhang. Synthesis of nano-agi arrays and their optical properties. *Journal of Materials Research*, 16(4):990–992, 2001.

[35] H. von Berlepsch, C. Bottcher, A. Ouart, C. Burger, S. Dahne, and S. Kirstein. Supramolecular structures of j-aggregates of carbocyanine dyes in solution. *Journal of Physical Chemistry B*, 104(22):5255–5262, 2000.

[36] Stefan Kirstein, Hans von Berlepsch, and Christoph Böttcher. Photo-induced reduction of noble metal ions to metal nanoparticles on tubular j-aggregates. *International Journal of Photoenergy*, 2006, 2006.

[37] Doerthe M. Eisele, Jasper Knoester, Stefan Kirstein, Juergen P. Rabe, and David A. Vanden Bout. Uniform exciton fluorescence from individual molecular nanotubes immobilized on solid substrates. *Nature Nanotechnology*, 4(10):658–663, 2009.

[38] B. Jirgensons and M.E. Straumanis. *A Short Textbook of Colloid Chemistry*. Elsevier Science, 2013.

[39] C. Tanford. *The hydrophobic effect: formation of micelles and biological membranes*. Wiley, 1980.

[40] Kevin Letchford and Helen Burt. A review of the formation and classification of amphiphilic block copolymer nanoparticulate structures: micelles, nanospheres, nanocapsules and polymersomes. *European Journal of Pharmaceutics and Biopharmaceutics*, 65(3):259–269, 2007.

[41] A. S. Davydov. *Theory of molecular excitons.* Plenum Press, New York, 1971.

[42] Dietmar Möbius. Scheibe aggregates. *Advanced Materials*, 7(5):437–444, 1995.

[43] Frank Würthner, Theo E. Kaiser, and Chantu R. Saha-Möller. J-aggregates: From serendipitous discovery to supramolecular engineering of functional dye materials. *Angewandte Chemie International Edition*, 50(15):3376–3410, 2011.

[44] Jacob N. Israelachvili, D. John Mitchell, and Barry W. Ninham. Theory of self-assembly of hydrocarbon amphiphiles into micelles and bilayers. *Journal of the Chemical Society, Faraday Transactions 2: Molecular and Chemical Physics*, 72(0):1525–1568, 1976.

[45] D. John Mitchell and Barry W. Ninham. Micelles, vesicles and microemulsions. *Journal of the Chemical Society, Faraday Transactions 2: Molecular and Chemical Physics*, 77(4):601–629, 1981.

[46] R. Nagarajan. Molecular packing parameter and surfactant self-assembly: the neglected role of the surfactant tail. *Langmuir*, 18(1):31–38, 2002.

[47] J. Knoester. Nonlinear-optical line-shapes of disordered molecular aggregates - motional narrowing and the effect of intersite correlations. *Journal of Chemical Physics*, 99(11):8466–8479, 1993.

[48] Jasper Knoester. Third-order optical response of molecular aggregates. disorder and the breakdown of size-enhancement. *Chemical Physics Letters*, 203(4):371–377, 1993.

[49] E. W. Knapp. Lineshapes of molecular aggregates, exchange narrowing and intersite correlation. *Chemical Physics*, 85(1):73–82, 1984.

[50] Steven de Boer, Kees J. Vink, and Douwe A. Wiersma. Optical dynamics of condensed molecular aggregates: An accumulated photon-echo and hole-burning study of the j-aggregate. *Chemical Physics Letters*, 137(2):99–106, 1987.

[51] Steven De Boer and Douwe A. Wiersma. Dephasing-induced damping of superradiant emission in j-aggregates. *Chemical Physics Letters*, 165(1):45–53, 1990.

[52] H. Fidder, J. Knoester, and D. A. Wiersma. Optical-properties of disordered molecular aggregates - a numerical study. *Journal of Chemical Physics*, 95(11):7880–7890, 1991.

[53] Francis C. Spano and Shaul Mukamel. Nonlinear susceptibilities of molecular aggregates: Enhancement of $\chi^{(3)}$ by size. *Physical Review A*, 40(10):5783–5801, 1989.

[54] E. E. Jelley. Spectral absorption and fluorescence of dyes in the molecular state. *Nature*, 138:1009–1010, 1936.

[55] G. Scheibe. Auxiliary valency as the cause of variability in the absorption spectra in solutions. *Angewandte Chemie*, 50:0212–0219, 1937.

[56] G. Scheibe, L. Kandler, and H. Ecker. Polymerisation and polymere adsorption as a cause of novel absorption bands of organic pigments. *Naturwissenschaften*, 25:75–75, 1937.

[57] G. Scheibe, A. Mareis, and H. Ecker. The reverible polymerisation as a cause of unusual absorption bands iii. *Naturwissenschaften*, 25:474–475, 1937.

[58] S. E. Sheppard. The effects of environment and aggregation on the absorption spectra of dyes. *Reviews of Modern Physics*, 14(2/3):0308–0345, 1942.

[59] C. Didraga, A. Pugzlys, P. R. Hania, H. von Berlepsch, K. Duppen, and J. Knoester. Structure, spectroscopy, and microscopic model of tubular carbocyanine dye aggregates. *Journal of Physical Chemistry B*, 108(39):14976–14985, 2004.

[60] H. von Berlepsch, S. Kirstein, R. Hania, A. Pugzlys, and C. Bottcher. Modification of the nanoscale structure of the j-aggregate of a sulfonate-substituted amphiphilic carbocyanine dye through incorporation of surface-active additives. *Journal of Physical Chemistry B*, 111(7):1701–1711, 2007.

[61] C. Didraga, J. A. Klugkist, and J. Knoester. Optical properties of helical cylindrical molecular aggregates: The homogeneous limit. *Journal of Physical Chemistry B*, 106(44):11474–11486, 2002.

[62] Cătălin Didraga and Jasper Knoester. Exchange narrowing in circular and cylindrical molecular aggregates: degenerate versus nondegenerate states. *Chemical Physics*, 275(1–3):307–318, 2002.

[63] S. Kirstein and S. Daehne. J-aggregates of amphiphilic cyanine dyes: Self-organization of artificial light harvesting complexes. *International Journal of Photoenergy*, 2006.

[64] Doerthe Melitta Eisele. *Optical, Structural and Redox Properties of Nanotubular J-aggregates of Amphiphilic Cyanine Dyes*. PhD thesis, 2010.

[65] Doerthe M. Eisele, Dylan H. Arias, Xiaofeng Fu, Erik A. Bloemsma, Colby P. Steiner, Russell A. Jensen, Patrick Rebentrost, Holger Eisele, Andrei Tokmakoff, Seth Lloyd, Keith A. Nelson, Daniela Nicastro, Jasper Knoester, and Moungi G. Bawendi. Robust excitons inhabit soft supramolecular nanotubes. *Proceedings of the National Academy of Sciences of the United States of America*, 111(33):E3367–E3375, 2014.

[66] Jennifer L. Lyon, Doerthe M. Eisele, Stefan Kirstein, Juergen P. Rabe, David A. Vanden Bout, and Keith J. Stevenson. Spectroelectrochemical investigation of double-walled tubular j-aggregates of amphiphilic cyanine dyes. *Journal of Physical Chemistry C*, 112(4):1260–1268, 2008.

[67] J. R. Lenhard and A. D. Cameron. Electrochemistry and electronic-spectra of cyanine dye radicals in acetonitrile. *Journal of Physical Chemistry*, 97(19):4916–4925, 1993.

[68] C. Kittel. *Introduction to Solid State Physics*. Wiley, 2004.

[69] W. Massa and R.O. Gould. *Crystal Structure Determination*. Springer Berlin Heidelberg, 2010.

[70] C. Giacovazzo. *Fundamentals of Crystallography*. Oxford University Press, 2002.

[71] J. J. De Yoreo and P. G. Vekilov. *Principles of crystal nucleation and growth*, volume 54 of *Reviews in Mineralogy and Geochemistry*, pages 57–93. 2003.

[72] P. Sear Richard. Nucleation: theory and applications to protein solutions and colloidal suspensions. *Journal of Physics: Condensed Matter*, 19(3):033101, 2007.

[73] Neil James Alexander Conway, John Horton; Sloane. *Sphere Packings, Lattices and Groups*. A Series of Comprehensive Studies in Mathematics. Springer New York, 1999.

[74] http://www.crystallography.net/cod/.

[75] A. L. Patterson. The scherrer formula for x-ray particle size determination. *Physical Review*, 56(10):978–982, 1939.

[76] J. W. Gibbs. On the equilibrium of heterogeneous substances. *American Journal of Science*, Series 3 Vol. 16(96):441–458, 1878.

[77] F. Abraham. *Homogeneous Nucleation Theory: The Pretransition Theory of Vapor Condensation*. Elsevier Science, 2012.

[78] D. Turnbull and B. Vonnegut. Nucleation catalysis. *Industrial and Engineering Chemistry*, 44(6):1292–1298, 1952.

[79] http://www.eng.utah.edu/ lzang/images/lecture-12.pdf.

[80] M. Volmer. The migration of adsorbed molecules on surfaces of solids. *Transactions of the Faraday Society*, 28:0359–0363, 1932.

[81] M. Volmer and W. Schultze. Condensation of crystals. *Zeitschrift Fur Physikalische Chemie-Abteilung a-Chemische Thermodynamik Kinetik Elektrochemie Eigenschaftslehre*, 156(1):1–22, 1931.

[82] M. Volmer and M. Marder. The theory of the linear crystalisation rate of under cooled melts and under cooled firm modifications. *Zeitschrift Fur Physikalische Chemie-Abteilung a-Chemische Thermodynamik Kinetik Elektrochemie Eigenschaftslehre*, 154(1/2):97–112, 1931.

[83] G. Wulff. On the question of speed of growth and dissolution of crystal surfaces. *Zeitschrift Fur Krystallographie Und Mineralogie*, 34(5/6):449–530, 1901.

[84] N. Wang, Y. Cai, and R. Q. Zhang. Growth of nanowires. *Materials Science + Engineering R-Reports*, 60(1-6):1–51, 2008.

[85] T. A. Witten and L. M. Sander. Diffusion-limited aggregation, a kinetic critical phenomenon. *Physical Review Letters*, 47(19):1400–1403, 1981.

[86] Shyi-Long Lee and Chung-Kung Lee. Simulation of diffusion-limited aggregation and reactions over its surfaces. *International Journal of Quantum Chemistry*, 52(2):339–352, 1994.

[87] Y. G. Sun, B. Gates, B. Mayers, and Y. N. Xia. Crystalline silver nanowires by soft solution processing. *Nano Letters*, 2(2):165–168, 2002.

[88] Y. G. Sun, Y. D. Yin, B. T. Mayers, T. Herricks, and Y. N. Xia. Uniform silver nanowires synthesis by reducing agno3 with ethylene glycol in the presence of seeds and poly(vinyl pyrrolidone). *Chemistry of Materials*, 14(11):4736–4745, 2002.

[89] Huamei Shang and Guozhong Cao. *Template-Based Synthesis of Nanorod or Nanowire Arrays*, pages 169–186. Springer Berlin Heidelberg, Berlin, Heidelberg, 2010.

[90] D. Ugarte, A. Chatelain, and W. A. deHeer. Nanocapillarity and chemistry in carbon nanotubes. *Science*, 274(5294):1897–1899, 1996.

[91] M. H. Huang, A. Choudrey, and P. D. Yang. Ag nanowire formation within mesoporous silica. *Chemical Communications*, (12):1063–1064, 2000.

[92] E. Braun, Y. Eichen, U. Sivan, and G. Ben-Yoseph. Dna-templated assembly and electrode attachment of a conducting silver wire. *Nature*, 391(6669):775–778, 1998.

[93] Lu Tao, Yukun Gao, Pinju Wu, Xiong Lu, and Faming Gao. Insulin templated synthesis of single-crystalline silver nanocables with ultrathin ag cores. *Rsc Advances*, 5(47):37814–37817, 2015.

[94] Carter C. Barry Williams, David B. *Transmission Electron Microscopy*. Springer US, 2009.

[95] James Howe Brent Fultz. *Transmission Electron Microscopy and Diffractometry of Materials*. Springer; 3rd edition, 2009.

[96] Helmut Kohl Ludwig Reimer. *Transmission Electron Microscopy: Physics of Image Formation*. Springer Science+Business Media, New York, 2008.

[97] Ray F. Egerton. *Physical principles of electron microscopy*. Springer Science+Business Media, New York, 2005.

[98] F. Haguenau, P. W. Hawkes, J. L. Hutchison, B. Satiat-Jeunemaitre, G. T. Simon, and D. B. Williams. Key events in the history of electron microscopy. *Microscopy and Microanalysis*, 9(2):96–138, 2003.

[99] F. Zemlin. Image formation in high-resolution electron microscopy. *Crystal Research and Technology*, 33(7-8):1097–1111, 1998.

[100] http://www.maxsidorov.com/ctfexplorer/.

[101] H. von Berlepsch, S. Kirstein, and C. Bottcher. Supramolecular structure of j-aggregates of a sulfonate substituted amphiphilic carbocyanine dye in solution: Methanol-induced ribbon-to-tubule transformation. *Journal of Physical Chemistry B*, 108(48):18725–18733, 2004.

[102] C. T. Koch. *Determination of core structure periodicity and point defect density along dislocations*. PhD thesis, 2002.

[103] B. Wiley, Y. G. Sun, B. Mayers, and Y. N. Xia. Shape-controlled synthesis of metal nanostructures: The case of silver. *Chemistry-a European Journal*, 11(2):454–463, 2005.

[104] G. Carotenuto, S. DeNicola, and L. Nicolais. Spectroscopic study of the growth mechanism of silver microclusters. *Journal of Nanoparticle Research*, 3(5-6):469–474, 2001.

[105] S. Link and M. A. El-Sayed. Spectral properties and relaxation dynamics of surface plasmon electronic oscillations in gold and silver nanodots and nanorods. *Journal of Physical Chemistry B*, 103(40):8410–8426, 1999.

[106] H. Cheng, B. Huang, Y. Dai, X. Qin, and X. Zhang. One-step synthesis of the nanostructured agi/bioi composites with highly enhanced visible-light photocatalytic performances. *Langmuir*, 26(9):6618–24, 2010.

[107] C. H. B. Ng and W. Y. Fan. Controlled synthesis of beta-agl nanoplatelets from selective nucleation of twinned ag seeds in a tandem reaction. *Journal of Physical Chemistry C*, 111(7):2953–2958, 2007.

[108] W. Jiang, C. H. An, J. X. Liu, S. T. Wang, L. M. Zhao, W. Y. Guo, and J. X. Liu. Facile aqueous synthesis of beta-agi nanoplates as efficient visible-light-responsive photocatalyst. *Dalton Transactions*, 43(1):300–305, 2014.

[109] B. Wiley, T. Herricks, Y. G. Sun, and Y. N. Xia. Polyol synthesis of silver nanoparticles: Use of chloride and oxygen to promote the formation of single-crystal, truncated cubes and tetrahedrons. *Nano Letters*, 4(9):1733–1739, 2004.

[110] Younan Xia, Yujie Xiong, Byungkwon Lim, and Sara E. Skrabalak. Shape-controlled synthesis of metal nanocrystals: Simple chemistry meets complex physics? *Angewandte Chemie-International Edition*, 48(1):60–103, 2009.

[111] Yiqun Zheng, Jie Zeng, Aleksey Ruditskiy, Maochang Liu, and Younan Xia. Oxidative etching and its role in manipulating the nucleation and growth of noble-metal nanocrystals. *Chemistry of Materials*, 26(1):22–33, 2014.

[112] A. Henglein. Reduction of ag(cn)(2)(-) on silver and platinum colloidal nanoparticles. *Langmuir*, 17(8):2329–2333, 2001.

[113] P. K. Sudeep and P. V. Kamat. Photosensitized growth of silver nanoparticles under visible light irradiation: A mechanistic investigation. *Chemistry of Materials*, 17(22):5404–5410, 2005.

[114] M. A. Asoro, D. Kovar, and P. J. Ferreira. In situ transmission electron microscopy observations of sublimation in silver nanoparticles. *Acs Nano*, 7(9):7844–7852, 2013.

[115] G. Safran, O. Geszti, G. Radnoczi, P. B. Barna, and K. Toth. Tem study of the structure and morphology of agi crystals formed on ag (001), (011) and (111) thin-films. *Thin Solid Films*, 259(1):96–104, 1995.

[116] A. Pawlik, A. Ouart, S. Kirstein, H. W. Abraham, and S. Daehne. Synthesis and uv/vis spectra of j-aggregating 5,5 ',6,6 '-tetrachlorobenzimidacarbocyanine dyes for artificial light-harvesting systems and for asymmetrical generation of supramolecular helices. *European Journal of Organic Chemistry*, 16(16):3065–3080, 2003.

[117] M. Y. Bashouti, R. Talebi, T. Kassar, A. Nahal, J. Ristein, T. Unruh, and S. H. Christiansen. Systematic surface phase transition of ag thin films by iodine functionalization at room temperature: Evolution of optoelectronic and texture properties. *Scientific Reports*, 6, 2016.

[118] Joerg Megow, Merle I. S. Roehr, Marcel Schmidt am Busch, Thomas Renger, Roland Mitric, Stefan Kirstein, Juergen P. Rabe, and Volkhard May. Site-dependence of van der waals interaction explains exciton spectra of double-walled tubular j-aggregates. *Physical Chemistry Chemical Physics*, 17(10):6741–6747, 2015.

[119] H. von Berlepsch, K. Ludwig, S. Kirstein, and C. Bottcher. Mixtures of achiral amphiphilic cyanine dyes form helical tubular j-aggregates. *Chemical Physics*, 385(1-3):27–34, 2011.

[120] Yan Qiao, Frank Polzer, Holm Kirmse, Stefan Kirstein, and Jurgen P. Rabe. Nanohybrids from nanotubular j-aggregates and transparent silica nanoshells. *Chemical Communications*, 51(60):11980–11982, 2015.

[121] D. M. Eisele, C. W. Cone, E. A. Bloemsma, S. M. Vlaming, C. G. F. van der Kwaak, R. J. Silbey, M. G. Bawendi, J. Knoester, J. P. Rabe, and D. A. Vanden Bout. Utilizing redox-chemistry to elucidate the nature of exciton transitions in supramolecular dye nanotubes. *Nature Chemistry*, 4(8):655–662, 2012.

[122] Sheng Xu, Haicheng Zhou, Jian Xu, and Yadong Li. Synthesis of size-tunable silver iodide nanowires in reverse micelles. *Langmuir*, 18(26):10503–10504, 2002.

[123] Ivana Lj Mladenovic, Willem K. Kegel, Paul Bomans, and Peter M. Frederik. Observation of equilibrium, nanometer-sized clusters of silver iodide in aqueous solutions. *The Journal of Physical Chemistry B*, 107(24):5717–5722, 2003.

[124] C. Mees and T. James. The theory of the photographic process the macmillan co. *New York*, 19, 1942.

[125] P. Fayet, F. Granzer, G. Hegenbart, E. Moisar, B. Pischel, and L. Wöste. The role of small silver clusters in photography. *Zeitschrift für Physik D Atoms, Molecules and Clusters*, 3(2):299–302, 1986.

[126] R. Makiura, T. Yonemura, T. Yamada, M. Yamauchi, R. Ikeda, H. Kitagawa, K. Kato, and M. Takata. Size-controlled stabilization of the superionic phase to room temperature in polymer-coated agi nanoparticles. *Nature Materials*, 8(6):476–480, 2009.

[127] Stefan Kirstein, Hans von Berlepsch, Christoph Böttcher, Christian Burger, Andre Ouart, Günter Reck, and Siegfried Dähne. Chiral j-aggregates formed by achiral cyanine dyes. *Chemphyschem*, 1(3):146–150, 2000.

Acknowledgement

First of all I want to thank Dr. Stefan Kirstein for supervising this thesis. He brought me to the interesting field of J-aggregates and supervised me since my Diploma thesis. With his patience and honest interest in since he was always a great benefit not only for me but for the whole group.

Prof. Jürgen P. Rabe gave me the opportunity to work in his group for which I am very grateful. His clear and structured way of working has always been a great help, especially in the preparation of presentations and writting papers.

I want to thank Prof. Christoph T. Koch and Prof. Monika Schönhoff for being further members of my Ph.D. committee.

My special thank goes to Dr. Frank Polzer for teaching me how to use the TEM and performing cryo-TEM. Dr. Holm Kirmse I like to thank for the HRTEM measurements. He was a great support in acquiring data on the TEM and analyzing and interpreting this data. Dr. Zdravko Kochovski had the very important job of keeping the TEM serviceable all the time, which he did great.

I like to thank Martin Kärgell for organizing and Georges Dahms for performing the ICP-MS measurements.

The whole group of Prof. Jürgen P. Rabe was responsible for a creative and productive working atmosphere. Evi Poblenz made the labs a safe place to work and Lothar Geyer did the same for the computers. Katherine Herman and Omar Al-Khatib I like to thank for proof reading my thesis as well as very fruitful collaborations. Caroline Falk, Philipp Lange, Vitalij Scenev, Jose Cojal, Abdul Rauf, and Nikolai Severin are all own my special thank for making work on this thesis sometimes even fun. Without the expertise of Yan Qiao this thesis would never have been finished the way it is. It was always a pleasure working with you.

Last but not least I want to thank my family and friends for having supported me on this long way.

Selbständigkeitserklärung

Ich erkläre, dass ich die Dissertation selbständig und nur unter Verwendung der von mir gemäß § 7 Abs. 3 der Promotionsordnung der Mathematisch-Naturwissenschaftlichen Fakultät, veröffentlicht im Amtlichen Mitteilungsblatt der Humboldt-Universität zu Berlin Nr. 126/2014 am 18.11.2014 angegebenen Hilfsmittel angefertigt habe.

Berlin, den 30.05.2018